Weak Deflection Angle via Gauss-Bonnet Theorem

Yashmitha Kumaran

Submitted to the
Institute of Graduate Studies and Research
in partial fulfillment of the requirements for the degree of

Doctor of Philosophy
in
Physics

Eastern Mediterranean University
July 2023
Gazimağusa, North Cyprus

Approval of the Institute of Graduate Studies and Research

Prof. Dr. Ali Hakan Ulusoy
Director

I certify that this thesis satisfies all the requirements as a thesis for the degree of Doctor of Philosophy in Physics.

Prof. Dr. İzzet Sakallı
Chair, Department of Physics

We certify that we have read this thesis and that in our opinion it is fully adequate in scope and quality as a thesis for the degree of Doctor of Philosophy in Physics.

Assoc. Prof. Dr. Ali Övgün
Supervisor

Examining Committee

1. Prof. Dr. Durmuş Ali Demir
2. Prof. Dr. S. Habib Mazharimousavi
3. Prof. Dr. İlkay Türk Çakır
4. Prof. Dr. Osman Yılmaz
5. Assoc. Prof. Dr. Ali Övgün

ABSTRACT

Researchers have come a long way in understanding our universe. The chief objective of this piece of text is to augment and improve the contributions to that ever-changing world of mysteries in Physics, in particular, black holes. Various kinds of black holes are discussed along with the potential influencing factors... some conventional facets, some customised. The underlying vision of this research is to provide as many analyses with as few assumptions as possible so that future works, observations, and/or experiments can have a solid set of references.

The main focus of this research is studying the gravitational lensing caused by black holes and employing the Gauss-Bonnet theorem to evaluate the weak deflection angle. Five different types of black holes with various kinds of consequences. The advantages, approximations, and disadvantages of every derivation are also mentioned. Several attempts to minimize presumptions were made in this work irrespective of how complicated it is, though, a few still happen to exist, mostly limited by current technology. New discoveries about the cosmos happen every day inching one step closer to the ultimate truth. After all, lesser premises mean more authenticity.

Keywords: Black Hole, Gravitational Lensing, Gauss-Bonnet Theorem, Weak Deflection Angle, General Relativity, Quantum Cosmology, Quantum Gravity, Plasma, Dark Matter.

ÖZ

Araştırmacılar evrenimizi anlama konusunda uzun bir yol kat etmişlerdir. Bu tezin başlıca amacı, özellikle kara delikler olmak üzere, Fizik biliminin her zaman değişen gizemler dünyasına olan katkıları artırmak ve geliştirmektir. Farklı türlerdeki kara delikler ve karadelikleri etkileyen potansiyel faktörler, incelenmiştir. Bu araştırmanın temel vizyonu, gelecekteki çalışmalara, gözlemlere ve/veya deneylere sağlam bir referans seti sunabilmek için mümkün olduğunca az varsayımla mümkün olduğunca çok analiz sağlamaktır.

Bu araştırmanın ana odak noktası, kara delikler tarafından oluşturulan yerçekimi merceklenmesini incelemek ve Gauss-Bonnet teoremini kullanarak zayıf sapma açısını hesaplamaktır. Farklı özelliklere sahip beş farklı tür kara delik kullanılmıştır. Her türdeki karadeliğin avantajları, ve dezavantajları da belirtilmiştir. Bu çalışmada varsayımları en aza indirgeme girişimlerinde bulunulmuştur, ne kadar karmaşık olursa olsun, ancak, birkaçı hala var olmaya devam etmektedir, çoğunlukla mevcut teknoloji tarafından sınırlıdır. Evren hakkında her gün yeni keşifler yapılmakta ve nihai gerçeğe bir adım daha yaklaşılmaktadır. Daha az varsayım daha fazla otantiklik anlamına gelir.

Anahtar Kelimeler:Kara Delik, Yerçekimsel Mercekleme, Gauss-Bonnet Teoremi, Zayıf Sapma Açısı, Genel Görelilik, Kuantum Kozmolojisi, Kuantum Kütleçekimi, Plazma, Karanlık Madde.

ACKNOWLEDGMENTS

Firstly, I would like to thank My Almighty God for bringing me to this island and giving me this opportunity, both personally and professionally. Next, I thank my Mother for encouraging me to aim for the stars since I was a kid and for living as a role model for me to keep studying and learning. I especially thank her time and effort in offering her all the help possible so that I can achieve everything. I thank my Father for believing in me no matter how much opposition he gained from loved ones in giving me the freedom to pursue my dreams, even if it broke our cultural norm, and for supporting me every step of the way, emotionally and financially. I thank my Brother for always taking my side, having deep conversations with me about black holes through the night, and being truly encouraging and inspiring. I thank my Husband for taking care of me like a baby tirelessly as I got through, celebrating/crying with me, cooking for me, checking on me, and so much more. I thank my In-Laws for all their prayers and motivation since the day I knew them.

I would like to express my sincere gratitude to my supervisor for having an extraordinary amount of confidence in me and for his meticulous efforts in constantly yet patiently pulling me through all the time, without which I would not be here. I extend my thanks to my department Chair and the Vice-Chair who have taken care of me as mentors professionally and as family personally. I thank all the academic and administrative staff of my department for so many things, all of which I can neither list nor remember. Finally, I thank all my students, my family, my friends, and last but not least, my dogs for consistently energizing me in a lot of ways I realized not.

Note that this thesis incorporates findings from my six papers: [1–6].

TABLE OF CONTENTS

LIST OF TABLES

LIST OF FIGURES

Chapter 1

INTRODUCTION

> "A black hole, a cosmic masterpiece hidden in the veil of equations, patiently awaits the moment when we lift our eyes to the heavens, and a century later, reveals itself in all its awe-inspiring splendor!"

1.1 Gravity

Since 1666, the tale of a falling apple transmits through generations promoting Newtonian gravity. For centuries, physicists have assumed that gravitational force is proportional to the product of the interacting masses and the square of their separation via a proportionality constant. According to this, gravity possesses the ability to draw objects within its reach inward, yet, its effect diminishes with distance until it is no longer essential. The Cavendish experiment provided an accurate value for this 'Gravitational' constant. Gravitational physics has long piqued the interest of physicists of various disciplines. Mercury's orbit was the first paradox to reveal the need to refine Newtonian gravitational theory.

Following Heaviside and his pioneering theory in 1893, Poincaré penned down his epiphany of gravitational waves in 1905 by means of his *Sur la dynamique de l' électron*. The concept of a gravitational counterpart to the electromagnetic wave travelling at a speed equivalent to the speed of light was naturally compelling and opened up new possibilities in understanding the fundamental nature of gravity and its interactions.

The 1910s saw the emergence of Einstein's General Theory of Relativity (GR),

proposing a finite, spherical universe discovering the gravitational constant G to be dependent on mass distribution and universe size, in order to account for inertial forces. [10]. The substantiation of Lorentz Transformations and GR has served as a catalyst for numerous researchers, motivating them to pursue the exploration and the reformulation of Newtonian gravity in order to transcend its constraints at high speeds, in extreme gravitational fields, and in the realm of particle physics. The Dark Matter hypothesis is the most victorious justification of the Newtonian "missing mass" problem, [11]. While this theory has many merits, there have been quite a few disagreements about integrating a new form of matter, implying that Newtonian dynamics must be modified to account for it.

The perception of ripples in spacetime was another prediction of GR that was in tandem with the theory of gravitational waves. Though Einstein himself believed that the radiation from gravitational waves will not be detected owing to the feeble intensity of matter-gravity interaction, LIGO successfully detected gravitational waves following a series of attempts since the early 1960s [12] from a black hole merger that was 400 megaparsecs away from the Earth. These observations and experiments confirmed the validity of GR and paved the way for several other works, now that the right direction was set in motion.

1.2 Black Holes

Gravity, the least powerful among the fundamental forces in our universe, exhibits different behavior as the mass of an object increases. When the mass becomes sufficiently large, causing the object to collapse and concentrate at a single point, gravity does not just surpass the other three natural forces; rather, it defies the known rules governing our physical reality. A black hole, characterized by its immense mass, infinitesimal volume, infinite density, and overwhelming gravitational pull, possesses

such extraordinary strength that anything that enters its grasp is unable to escape. [13].

The evolution of black hole physics can be traced back to 1784, when the English philosopher John Michell [14]. He proposed that all light emitted by an invisible central body with a radius greater than five hundred times that of the sun but a density equal to that of the sun would return to it due to gravity. When an object falls from infinity into the central body, it acquires a velocity greater than that of light at the central body's surface due to the latter's force of attraction.

In the year 1796 [15], Laplace proposed an invisible star that could potentially be the largest and most gravitating luminous object in the universe. His theories were based on observations of an astronomical body with the density of the Earth but a diameter more than 250 times that of the sun, preventing its light from reaching us due to its strong attraction.

Einstein's groundbreaking 1915 theory proposes that the apparent gravitational force is caused by the curvature of the fabric of spacetime. [13]. In the year 1916, Schwarzschild presented the first solution for the simplest black holes, depicting the gravitational field from a spherical mass with no angular momentum, charge, or universal cosmological constant. [16]. Between then and 1918, the combined efforts of four European physicists yielded the Reissner-Nordström metric, which was solved using the Einstein-Maxwell equations to represent electrically charged black holes. [17].

Centuries of research have enabled humanity to understand the concept of a star

collapsing due to its own intense gravity into a black hole to the extent that not even light can escape its gravitational pull beyond its horizon. Being a consequence of General Relativity, black holes are enigmatic objects of the universe that started off as a bunch of mathematical equations which were written down only to take form in the sky hundred years later!

Since LIGO successfully detected gravitational waves from two merging black holes, black holes have captivated the scientific community. [5, 12, 18]. As endeavors persist to enhance the sensitivity of detectors for future detections, the groundbreaking achievement of the Event Horizon Telescope brought about a revolutionary moment in the field of physics by providing the initial glimpse into M87* [19]. Einstein's theory of relativity, which revolutionized physics, received its long-awaited validation after a century with this novelty image of a supermassive black hole that was released on April 10, 2019 [19]. This has ushered in a new era in theoretical cosmology, stimulating the interest of numerous researchers in black holes. [20, 21].

1.3 Gravitational Lensing

Light is a distinct type of radiation that serves diverse purposes, ranging from vision to life. The most fascinating aspect of light, however, is how it interacts with heavy objects. In addition to resolving the enigma of Mercury's precession, the phenomenon of light deflection in the presence of a massive object has unveiled a broad spectrum of new/unexplored avenues, including the realms of spacetime and its null structure. [22, 23].

Light is a major factor in overriding a black hole being invisible by means of a phenomenon that occurs due to the deflection of light rays by the gravity fields of a massive object in their path to a distant observer. Called gravitational lensing, the

light rays from the source in the background are distorted owing to the massive object acting as a lens [24]. A black hole is one of the elements that trigger the unusual gravitational lensing phenomenon. As light traverses a cluster of massive objects en route to an observer, the gravitational influence of the cluster causes the light rays to bend, giving rise to a gravitational lens. This phenomenon, first proposed by Einstein, results in the distortion of the observed light. Galaxy clusters tend to deviate from passing light because of the gravity fields, contributing to distortions of the source in the background.

Since Eddington's first observation of gravitational lensing, several researchers have explored the gravitational lensing effects induced by different celestial objects, including black holes, wormholes, and cosmic strings. Based on the characteristics of the lensing system, lensing can be categorized into three distinct types: strong, weak, and micro lensing [10]. The phenomenon of strong lensing gives rise to distinctive features such as arcs and rings, exemplified by Einstein's ring. On the other hand, weak lensing is characterized by subtle distortions that result in magnifications too small to be discerned individually, unless observed across a large number of galaxies. These weak distortions, when averaged over a significant sample, provide insights into mass distributions [25]. Through the intricate effect of lensing, even subtle magnifications uncover hidden details and allow for the identification of mass distributions. In addition to the aforementioned phenomena, other captivating aspects such as gravitational monopoles, exoplanets, dark matter, dark energy, and galaxy clusters have garnered attention. These remarkable discoveries have solidified the enduring significance of general relativity, serving as a fundamental pillar for ongoing advancements in scientific theory.

1.4 Shadow

The invisibility of a black hole has not stopped its distant observers from seeing it, thanks to the existence of a shadow [26]. The extreme gravitational pull of the black hole compels the light rays to be deflected toward the singularity, causing those that skim the photon sphere to start looping around it.

When a photon ends up precisely on the photon sphere, it will continue to encircle the black hole forever. This phenomenon occurs for the light rays passing in the neighbourhood of the unstable photon region abet the intensity of the original source through the extended path length of the light rays, thus, increasing its brightness around the shadow's edge; consecutively, the cloud's brightness just outside the shadow appears to be enhanced as well. The captured light rays spiraling into a black hole and the scattered light rays veering away from it are separated by a shadow, giving it the facade of a bright surrounding illuminating a dark disk. Therefore, it is also known as the critical curve that manifests as an isotropic and homogenous emission ring.

The accretion disk that is formed due to the immense gravity of a black hole attracting and trapping everything in its path such as dust, photons, radiation, etc., [26] constitutes the shadow shape and size, hence, indirectly making it visible and observable [27, 28]. The shadow is imagined to be a circular ring of light around its host; however, in reality, this is not the case. It is a region that is geometrically thick and optically thin, especially for regular black holes, that is not so circular. This means that the disk of orbits surrounding the black hole is spread out (geometrically thick) but the matter in the disk is too scanty to absorb or scatter light that the rays passing through it experiences barely any intrusion.

In relativistic models, the size and shape of a shadow are found to be dependent on the geometry of the spacetime, not the accretion [29]. For a given black hole, its intrinsic parameters play a major role in determining the size of the shadow, whereas, the light rays and the instabilities of their orbits in the photosphere affect its contour. Numerous researchers have explored the distinct imprints that alternative gravitational theories leave behind by studying the phenomenon of shadows [5, 9, 22, 23, 30, 30–41].

Apart from accretion, the effects of lensing were seen to influence the shadow dramatically through the radiation from the accretion [27, 28], as it is caused by the non-circular photon sphere. The captivating occurrence became notably apparent in the initial images captured by the James Webb Space Telescope, particularly showcasing the galactic cluster referred to as SMACS 0723, attributable to an immense concentration of celestial matter observed within a minuscule portion of the sky, approximately equivalent to the size of a grain of sand when viewed at arm's length. [42]. In the realm of astrophysics, the determination of object distances plays a pivotal role in unravelling their inherent qualities and quantities.

The above-mentioned aspects are thoroughly analyzed for five different black holes [1–6]. The purpose of this work is to incorporate as many logical cases as possible with the least plausible assumptions so that it can contribute to our knowledge of the cosmos.

1.4.1 Synopsis

The underlying concepts of this research have been defined above. In the upcoming section, the Gauss-Bonnet theorem is elucidated further as the foundation, along with a detailed methodology applied to the case of a Schwarzschild black hole. This is then extrapolated to five different black holes in §2 – §7.

Chapter 2

THE WEAK DEFLECTION ANGLE METHOD USING THE GAUSS-BONNET THEOREM

In this chapter, the pieces of literature that act as a foundation for this research have been briefly reviewed.

2.1 The Gauss-Bonnet Theorem

Weak gravitational lensing holds significant interest due to the noticeable distortions it induces in the light source. These distortions are sufficiently strong to be detected, yet they pose a challenge in swiftly discerning the prominent features of the source. Utilizing this subtle property of differential deflection exhibited by light bending can help us probe deeper into the celestial structures such as distinguishing between mass distributions, gaining insights into the infant universe, analyzing the geometry of the cosmic web, investigating the peripheral dark matter, etc. The conventional approach for studying this phenomenon involves determining the deflection angle, which quantifies the extent of light bending and gravitational lensing, which is, in turn, dependent on the lens' mass distribution.

The region where light undergoes bending plays a crucial role in determining the deflection angle in weak gravitational lensing. The behavior of light rays as optical geodesics in a metric space is examined to understand this phenomenon. In reference to [43], the Gauss-Bonnet theorem (GBT), which connects the surface's topology with its intrinsic geometry, provides a framework that ensures the bending angle

remains unchanged under certain coordinate transformations.

The Gauss-Bonnet theorem for a selected two-dimensional manifold $\mathscr{M}_R$ is given by:

$$\iint_{\mathscr{M}_R} \mathscr{K}\ \mathrm{d}S + \int_{\partial \mathscr{M}_R} \kappa\, \mathrm{d}\sigma + \sum_j \Theta_j = 2\pi\, \chi\,(\mathscr{M}_R)\,, \tag{2.1}$$

where $\mathscr{K}$ symbolizes the Gaussian optical curvature, dS depicts the differential element of a two-dimensional surface S, κ is identified as the geodesic curvature, σ stands for the line element along the boundary $\mathscr{M}_R$ in the $\mathscr{D}$ domain, Θ_j represents the exterior angle at the j^{th} vertex, and χ is the Euler characteristics of the topology. The surface domain is considered outside the light trajectory and can be written as $(\mathscr{D}, \chi, g)$; here, g is the Riemannian metric of the symmetric lens in $\mathscr{M}_R$.

Note that the Euler characteristic depends on the surface, originally defined for a polyhedron as $\chi = (\text{numberof})[\text{Faces} - \text{Vertices} + \text{Edges}]$. Generally speaking, the Euler characteristic in a geodesic triangle, $\chi\,(\mathscr{M}_R) = 1$ for regular domains and $\chi(\mathscr{M}_R) = 0$ if the centre of the lens is singular. So, for the surface under consideration, $\chi = 1$.

When gravitational lensing is approached geometrically, this proves effective in finding the deflection caused by any curved surface. In the weak lensing regime, it becomes possible to relate the geometry and the topology with GBT to determine the bending angle through the optical metric because:

- the metric evolves from the surface curvature relating it to its geometry
- the geodesics of the metric are spatial light rays regarding the focused light rays as a topological effect.

Elaborating with a triangle as in [44]: take $\bar{\Psi}_a$, $\bar{\Psi}_b$ and $\bar{\Psi}_c$ as the interior angles of a

triangle, $\bar{\Psi}_a + \bar{\Psi}_b + \bar{\Psi}_c = \pi$. Then, exterior angles: $\pi - \bar{\Psi}_a$, $\pi - \bar{\Psi}_b$, and $\pi - \bar{\Psi}_c$. Considering a spherical triangle that belongs to a unit sphere: $\bar{\Psi}_a + \bar{\Psi}_b + \bar{\Psi}_c > \pi$ such that $\bar{\Psi}_a + \bar{\Psi}_b + \bar{\Psi}_c - \pi = A_\Delta$ for the additional quantity A_Δ associated with the area of the triangle. Thus, for a sphere of radius R: $\bar{\Psi}_a + \bar{\Psi}_b + \bar{\Psi}_c - \pi = A_\Delta / R^2$.

Applying GBT over the given area with the Gaussian curvature of the sphere, $\mathscr{K}$:

$$\begin{aligned}
\int_{A_\Delta} \mathscr{K} \, \mathrm{d}S + \sum \text{external angles} &= \left[\frac{A_\Delta}{R^2}\right] + \left[(\pi - \bar{\Psi}_a) + (\pi - \bar{\Psi}_b) + (\pi - \bar{\Psi}_c)\right] \\
&= \left[\bar{\Psi}_a + \bar{\Psi}_b + \bar{\Psi}_c - \pi\right] + \left[3\pi - \bar{\Psi}_a - \bar{\Psi}_b - \bar{\Psi}_c\right] \\
&= (\bar{\Psi}_a + \bar{\Psi}_b + \bar{\Psi}_c) - \pi + 3\pi - (\bar{\Psi}_a + \bar{\Psi}_b + \bar{\Psi}_c) \\
&= 2\pi. \qquad (2.2)
\end{aligned}$$

Therefore, the differential geometry of the surface is connected to its underlying topology. The Gaussian curvature holds its significance as it represents the inherent measure of curvature at a specific point on a surface, which is a characteristic determined solely by the surface's own properties. For example, positive curvature $K = 1$ signifies that the underlying surface is a sphere. Similarly, $K = 0$ denotes a flat plane and $K = -1$ represents a hyperbolic plane.

Extending this concept to the fabric of spacetime (as discussed in [45]), the line element of a static, axis-symmetric spacetime that is also asymptotically flat is:

$$\mathrm{d}s^2 = g_{\mu\nu} \, \mathrm{d}x^\mu \, \mathrm{d}x^\nu = -f(r) \, \mathrm{d}t^2 + \frac{1}{g(r)} \, \mathrm{d}r^2 + r^2 \left(\mathrm{d}\theta^2 + \sin^2\theta \, \mathrm{d}\phi^2 \right), \qquad (2.3)$$

with a time coordinate t, radial coordinate r, and co-latitude θ and longitude ϕ both outlined for a point on the two-sphere. While the null geodesics satisfies $\mathrm{d}s^2 = 0$, consider the solution at the plane of equator $\theta = \pi/2$ so that $\mathrm{d}\theta$ is zero. The optical metric can be written as:

$$\mathrm{d}t^2 \equiv \bar{g}_{ij}\,\mathrm{d}x^i\,\mathrm{d}x^j = \bar{g}_{rr}\,\mathrm{d}r^2 + \bar{g}_{\phi\phi}\,\mathrm{d}\phi^2 = \frac{\mathrm{d}r^2}{f(r)g(r)} + \frac{r^2\,\mathrm{d}\phi^2}{f(r)}, \tag{2.4}$$

where $i, j \in [1,2,3]$. This is known as the optical metric and it consists of light rays that can be regarded as spatial geodesics, inducing a topological effect [46]. The Gaussian curvature of the optical metric is determined by evaluating the Christoffel symbols and the Ricci scalar $\mathscr{R}$ to have the general form:

$$\mathscr{K} = \frac{\mathscr{R}}{2} = -\frac{1}{\sqrt{\bar{g}_{rr}\bar{g}_{\phi\phi}}}\left[\frac{\partial}{\partial r}\left(\frac{1}{\sqrt{\bar{g}_{rr}}}\frac{\partial\sqrt{\bar{g}_{\phi\phi}}}{\partial r}\right) + \frac{\partial}{\partial\phi}\left(\frac{1}{\sqrt{\bar{g}_{\phi\phi}}}\frac{\partial\sqrt{\bar{g}_{rr}}}{\partial\phi}\right)\right]. \tag{2.5}$$

The geodesic curvature κ quantifies the amount of deviation of a curve from the shortest path along an arc that connects two points on a surface, i.e., a measure of how much a curve curves on a curved surface, and is given by:

$$\kappa = \frac{1}{2\sqrt{\bar{g}_{rr}\bar{g}_{\phi\phi}}}\left(\frac{\partial\bar{g}_{\phi\phi}}{\partial r}\frac{\mathrm{d}\phi}{\mathrm{d}t} - \frac{\partial\bar{g}_{rr}}{\partial\phi}\frac{\mathrm{d}r}{\mathrm{d}t}\right). \tag{2.6}$$

Using bounded $\mathscr{M}_R$ by a geodesic $\tilde{C} \equiv \partial\mathscr{M}_R$ from the source S to the observer O and a circular curve C_R intersecting $\tilde{C}$ in S and O at right angles, Eq. (2.1) reduces to:

$$\iint_{\mathscr{M}_R} \mathscr{K}\,\mathrm{d}S + \int_{\tilde{C}} \kappa(C_R)\,\mathrm{d}t = \pi, \tag{2.7}$$

where $\kappa(\tilde{C}) = 0$ and $\chi(\mathscr{M}_R) = 1$.

2.1.1 Gibbons and Werner Method

When contemplating a spatial domain characterized by the optical metric, one can delve into the realm of optical geometry where a point source and a spectator is present within an asymptotic region to alleviate the complexity of determining the deflection angle. Presume that the source, positioned at an infinite distance from a mass distribution that exhibits spherical symmetry, which functions as the lens, is viewed by the observer in an asymptotically flat spacetime [3]. If γ is taken to be a smooth curve in the said domain, then $\dot{\gamma}$ becomes the unit-speed vector [7]. With respect to this curve, the geodesic curvature κ is given by [3, 7]:

$$\kappa = g^{opt}(\nabla_{\dot{\gamma}}\dot{\gamma}, \ddot{\gamma}), \tag{2.8}$$

with a unit-speed constrain $g^{opt}(\dot{\gamma}, \dot{\gamma}) = 1$. Here, $\ddot{\gamma}$ is the unit-acceleration vector that

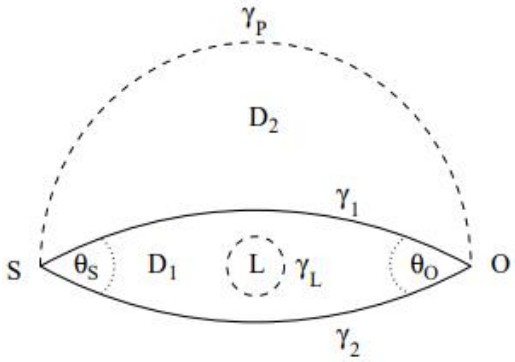

Figure 2.1: The geometry of weak lensing as given by Gibbons and Werner [7].

is perpendicular to $\dot{\gamma}$. When $R \to \infty$, the relevant jump angles are considered to be $\pi/2$; that is to say, the angles respective to the source and the observer sum up as $\Theta_S + \Theta_O \to \pi$. Given the fact that $\gamma_{\tilde{g}}$ is a geodesic and the geodesic curvature makes null contribution, i.e., $\kappa(\gamma_{\tilde{g}}) = 0$, the curve C_R as:

$$\kappa(C_R) = \mid \nabla_{\dot{C}_R}\dot{C}_R \mid . \tag{2.9}$$

Considering $C_R := r(\phi) = R =$ constant, R is the distance from the origin of the selected coordinate system. The radial component of κ becomes:

$$(\nabla_{\dot{C}_R}\dot{C}_R)^r = \dot{C}_R^{\phi}(\partial_{\phi}\dot{C}_R^{\phi}) + \Gamma^r_{\phi\phi}(\dot{C}_R^{\phi})^2. \tag{2.10}$$

Evidently, the first term disappears from the presumptions and so:

$$\lim_{R\to\infty} \kappa(C_R) = \lim_{R\to\infty} \left|\nabla_{\dot{C}_R}\dot{C}_R\right| \to \frac{1}{R}, \tag{2.11}$$

acquired from the unit-speed condition. At higher limits of radial distance,

$$\lim_{R\to\infty} \mathrm{d}t \to R\,\mathrm{d}\phi. \tag{2.12}$$

Going back to Eq. (2.7) and analyzing the second integral, the circular curve C_R such that $C_R := r(\phi) = R =$ constant. As $R \to \infty$:

$$\kappa(C_R)\,\mathrm{d}t = \lim_{R\to\infty}\left[\kappa(C_R)\,\mathrm{d}t\right] = \lim_{R\to\infty}\left[\frac{1}{2\sqrt{\bar{g}_{rr}\bar{g}_{\phi\phi}}}\left(\frac{\partial \bar{g}_{\phi\phi}}{\partial r}\right)\right]\mathrm{d}\phi$$

$$= \mathrm{d}\phi. \tag{2.13}$$

Inserting all this into Eq. (2.1):

$$\iint_{\mathscr{M}_R} \mathscr{K}\,\mathrm{d}S + \oint_{C_R} \kappa\,\mathrm{d}t \overset{R\to\infty}{=} \iint_{\mathscr{D}_\infty} \mathscr{K}\,\mathrm{d}S + \int_0^{\pi+\hat{\alpha}} \mathrm{d}\phi = \pi, \tag{2.14}$$

where, ϕ is the angular coordinate centered at the lens and $\hat{\alpha}$ is the small, positive, non-trivial, asymptotic angle of deflection that can be obtained as:

$$\hat{\alpha} = -\iint_{\mathscr{M}_{R\to\infty}} \mathscr{K}\,\mathrm{d}S. \tag{2.15}$$

Hence, the computation of the weak deflection angle involves integrating the curvature across an infinite region bounded by the light ray, disregarding the presence of the lens. This equation captures the overall effect on particle lensing, as it requires integration over the optical domain beyond the encompassed mass. To be more precise,

$$\hat{\alpha} = -\int_0^{\pi}\int_{b/\sin\phi}^{\infty} \mathscr{K}\,\mathrm{d}S. \tag{2.16}$$

Here, b denotes a dimensionless quantity called the impact parameter that allows for the use of the straight-line approximation. In this approximation, the light rays supposedly follow the trajectory $r = b/\sin\phi$ to zeroth order for $0 \le \phi \le \pi$ in the regime of weak deflection [7]. In practical terms, b represents the perpendicular separation between the asymptotic tangent to the central point (of the gravitating lens) and the line that outlines the light ray's path (i.e., the trajectory aligned with the ray's direction of motion that connects the ray to a distant observer). Furthermore,

$$\mathrm{d}S = \sqrt{\left(\frac{r^2}{f(r)^2 g(r)}\right)}\,\mathrm{d}r\,\mathrm{d}\phi. \tag{2.17}$$

Gibbons and Werner [7] presented this as an alternate approach in finding the deflection angle. They obtained the bending angle as a consequence of weak lensing using the Gauss-Bonnet theorem with the Gaussian curvature of the optical metric directed away from the light ray for a simply connected and asymptotically flat domain $\mathscr{D}$ in the manifold $\mathscr{M}_R$, in which the lens is not an element of the regime but the source and the observer are and the differential domain consists of a bounding geodesic at the source.

2.2 Methodology

In this section, the deflection angle is calculated for a Schwarzschild black hole in various instances. This will be the general framework throughout this research.

2.2.1 Schwarzschild Black Hole

The solution for a Schwarzschild black hole with mass M is given [16] by:

$$f(r) := 1 - \frac{2M}{r}. \tag{2.18}$$

The gravitational field is a pivotal factor to discern how spacetime behaves. Depending on the selected coordinate system, the time coordinate evolves with respect to the proper time from one hypersurface[1] to another. This can be accounted for by a lapse function. As time dilates near the event horizon, a lapse function is highly beneficial in the study of black holes especially since it is related to the black hole's geometry. So, the no.of horizons is determined by the quantities in f. That being said, the lapse function of $f(r)$ for a Schwarzschild black hole for different masses is given in Fig. 2.2.

Applying null geodesics to the line element in the form of Eq. (2.3) for $g(r) = f^{-1}(r)$ and choosing the equatorial plane $\theta = \pi/2 \Rightarrow \partial g_{\mu\nu}/\partial\theta = 0$, the optical metric is:

[1] Hypersurface is a slice of a higher dimension n represented by $n-1$ dimensions for better visualization – here, the temporal dimension is constrained to explore the spatial dimensions.

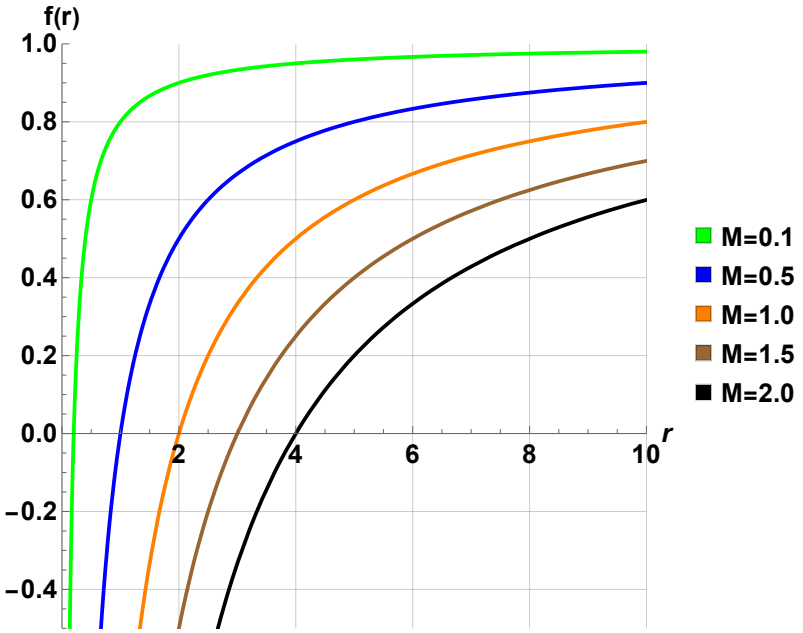

Figure 2.2: The lapse function of the Schwarzschild black hole for various masses.

$$\mathrm{d}t^2 = \frac{\mathrm{d}r^2}{\left(1-\frac{2M}{r}\right)^2} + \frac{r^2}{\left(1-\frac{2M}{r}\right)}\,\mathrm{d}\phi^2, \tag{2.19}$$

with:

$$\mathscr{K} = \frac{3M^2}{r^4} - \frac{2M}{r^3}. \tag{2.20}$$

Plugging this into Eq. (2.16) for $\mathrm{d}S$ given by Eq. (2.17), the bending angle in vacuum for a Schwarzschild black hole, calculated using the zeroth-order approximation along a straight line, is given by:

$$\hat{\alpha} = \frac{735\pi M^6}{256b^6} + \frac{28M^5}{5b^5} + \frac{75\pi M^4}{64b^4} + \frac{8M^3}{3b^3} + \frac{3\pi M^2}{4b^2} + \frac{4M}{b}. \tag{2.21}$$

Limiting this to the first order of M with $\mathrm{d}S \equiv r\,\mathrm{d}r\,\mathrm{d}\phi$ reduces it to [7]:

$$\hat{\alpha} = \frac{4M}{b}. \tag{2.22}$$

Graphical analysis of this equation is depicted in Fig. 2.3. The drastic effect of mass on the deflection angle is observed. It is to be noted that approximating the higher powers of mass to the first order has a trivial impact on the deflection angle.

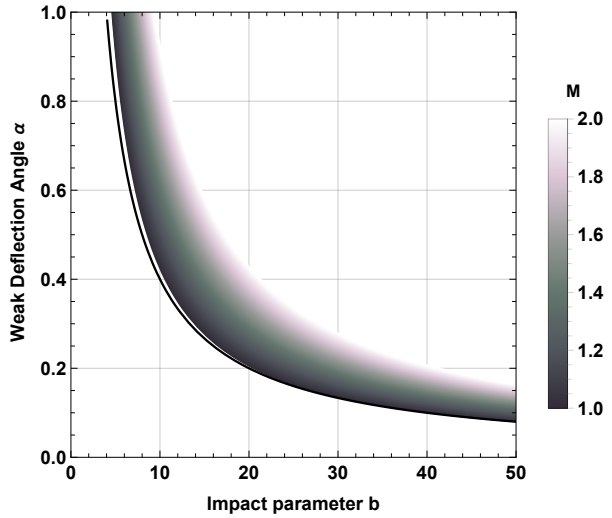

Figure 2.3: $\hat{\alpha}$ vs b for varying M. The solid black line represents the deflection angle for the first order of M.

2.2.2 Massive Particles

For SSS spacetime:

$$\mathrm{d}s^2 = g_{\mu\nu}\,\mathrm{d}x^\mu\,\mathrm{d}x^\nu = -A(r)\,\mathrm{d}t^2 + B(r)\,\mathrm{d}r^2 + C(r)\,\mathrm{d}\Omega^2, \tag{2.23}$$

can be re-written using the Jacobi metric:

$$\mathrm{d}l^2 = g_{ij}\,\mathrm{d}x^i\,\mathrm{d}x^j = \left(E^2 - m^2 A(r)\right)\left\{\frac{B(r)}{A(r)}\,\mathrm{d}r^2 + \frac{C(r)}{A(r)}\,\mathrm{d}\Omega^2\right\}, \tag{2.24}$$

where, E is the energy of the particle per unit mass m with $\mathrm{d}\Omega^2 = \mathrm{d}\theta^2 + r^2\sin^2\phi$ is the unit two-sphere's line element. One can utilize the Jacobi metric to determine the circular photon orbit's radius at the equatorial plane. Null particles have $m = 0$ and $E = 1$, reducing $\mathrm{d}l^2$ to the typical $\mathrm{d}t^2$. The presence of non-zero mass indicates an object possessing mass being examined and is therefore not moving at light speed c. From the perspective of an asymptotic distant observer, one of the conserved quantities is E and is perceived as:

$$E \equiv \frac{m}{\sqrt{1-v^2}}, \tag{2.25}$$

where v denotes the velocity of the particle. In the equatorial plane:

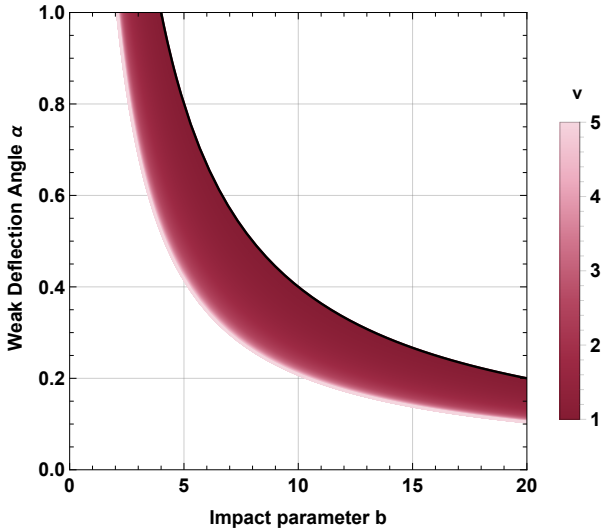

Figure 2.4: $\hat{\alpha}$ vs b for varying particle velocity v ($M = 1$).

$$\mathrm{d}l^2 = m^2 \left(\frac{1}{1-v^2} - A(r) \right) \left\{ \frac{B(r)}{A(r)}\, \mathrm{d}r^2 + \frac{C(r)}{A(r)}\, \mathrm{d}\phi^2 \right\}, \tag{2.26}$$

conserving the generality. The above metric's determinant has been established to be

$$g = m^4 B(r) C(r) \left[\frac{A(r)\left(v^2-1\right)+1}{A(r)\left(v^2-1\right)} \right]^2. \tag{2.27}$$

The Gaussian curvature for a Schwarzschild black hole surrounded by massive particles restricted to the first-order of M is:

$$\mathscr{K} = \frac{M\left(v^2-1\right)\left(v^2+1\right)}{v^4\left(m^2 r^3\right)} + \mathscr{O}\left(M^2\right). \tag{2.28}$$

The corresponding bending angle is found to be:

$$\hat{\alpha} = \frac{2M}{bv^2} + \frac{2M}{b}, \tag{2.29}$$

reducing to the vacuum case for $v = 1$. Graphically, this is represented by Fig. 2.4. The presence of massive particles seems to be attenuating the deflection angle for a Schwarzschild black hole. This is expected as massive particles interact with the light rays around the black hole retarding them.

2.2.3 Plasma

Lensing in a vacuum does not involve a photon's dispersive properties. So, the presence of a medium significantly alters the dispersive characteristics of light rays. As matter succumbs to the intense gravitational pull of a black hole, it simply collapses and subsequently experiences substantial heating to reach temperatures in the range of millions of degrees; this transformation gives rise to the formation of active plasma. If a ray of light strikes this heated mixture of ionized homogenous gas, it is refracted, mainstreaming the influence of plasma and implying the presence of a refractive index factor. Nevertheless, plasma often bombards lenses [47], revealing an essential factor contributing to the bending angle.

Gravitational deflection advocates the refracting of light, which ensues in further deflection. The refractive index [48], which accounts for the adjunct component, which is merely small yet not insignificant, particularly in the radio regime, outlines the shift in medium. Consider the circumstance where light moves into a hot, homogenous, ionized, non-magnetized plasmatic medium in order to encompass the effects of plasma. Let v stand for the speed of light through plasma. The index of refraction $n(r)$ is described by:

$$n(r) = \sqrt{1 - \frac{\omega_e^2}{\omega_\infty^2}\left(1 - \frac{2M}{r}\right)}, \tag{2.30}$$

in natural units, i.e., $c = 1$. Here, ω_e represents the plasmatic electron frequency, and ω_∞ denotes the photon frequency at infinity [1, 3, 5]. The presence of this non-zero factor leads to substantial deflection of light rays passing through. In order to determine the deflection angle in the plasma medium, it is necessary to utilize the appropriate optical metric given by:

$$\mathrm{d}\sigma^2 = g_{ij}^{\mathrm{opt}}\,\mathrm{d}x^i\,\mathrm{d}x^j = \frac{n^2(r)}{1 - \frac{2M}{r}\left(1 + \frac{4\alpha M^2}{L^2}\right)}\left[\frac{\mathrm{d}r^2}{1 - \frac{2M}{r}\left(1 + \frac{4\alpha M^2}{L^2}\right)} + r^2\,\mathrm{d}\phi^2\right]. \tag{2.31}$$

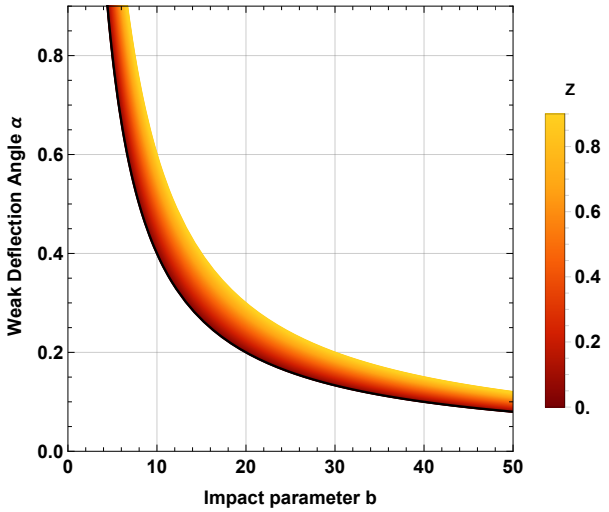

Figure 2.5: $\hat{\alpha}$ vs b for varying z ($M = 1$).

The Gaussian curvature for a Schwarzschild black hole surrounded by plasma is:

$$\mathscr{K} = -\frac{M\omega_\infty^2\left(2\omega_\infty^2 - \omega_e^2\right)}{r^3\left(\omega_\infty^2 - \omega_e^2\right)^2} + \mathscr{O}\left(M^2\right), \tag{2.32}$$

for which:

$$\hat{\alpha} = \frac{2M\omega_e^2}{b\omega_\infty^2} + \frac{4M}{b}, \tag{2.33}$$

reducing to the vacuum case for $\omega_e^2 = 0 \Rightarrow n(r) = 1$. Plotting Fig. 2.5, plasma is seen to escalate the deflection. For the sake of simplicity, $z \equiv \omega_e^2/\omega_\infty^2$ is defined as the ratio of frequencies to represent the refractive index.

2.2.4 Dark Matter

A medium which is known to exist almost always is the one surrounded by dark matter (DM). Poincaré laid the foundation for *matière obscure* – French for dark matter – as matter that was 'hard to observe.' Later, Zwicky phrased the terminology *dunkle materie* in German meaning dark matter or missing mass from the fact that he was able to observe too many galaxies with too little mass to cluster together, insinuating an immense amount of unseen or invisible mass that does not interact with light. In light of his detection of dark matter through gravitational lensing, multiple research endeavours and theories were and are being constantly developed to this day.

The enormous dark matter halo surrounding the black holes in the galactic centres is seen by the Event Horizon Telescope. It is a subject of inquisitivity due to its capacity to engulf galaxies and invade interstellar and intergalactic media. The extreme gravity that dark matter experiences around a black hole, combined with the gravitational effects it already endures, is a crucial aspect of astrophysics that would greatly help the gravitational lensing analyses. In the context of gravitational lensing, the notion of velocity dispersions as a consequence of non-thermal mechanisms is noteworthy as it disentangles mass and velocity to an extent [49].

The refractive index computed from the dark matter scatterers is:

$$n = 1 + Bu + vw^2. \tag{2.34}$$

In the provided equation, the symbol w represents the frequency of light. The term B is introduced as $B = \frac{\rho_0}{4m^2w^2}$, where ρ_0 represents the mass density of the DM scatterers. Another parameter, denoted as u, is defined as $u = -2\varepsilon^2 e^2$, where ε denotes the scatterer's charge in terms of e, and v is a non-negative value. The term of order w^{-2} is linked with a charged DM candidate, while w^2 corresponds with a neutral DM candidate. Its also possible for $\mathscr{O}(w)$, in w to be present if there are parity and charge-parity asymmetries. With dark matter:

$$\mathscr{K} = -\frac{2M}{r^3\left(Bu + vw^2 + 1\right)^2} + \mathscr{O}\left(M^2\right), \tag{2.35}$$

yielding:

$$\hat{\alpha} = \frac{4M}{b(1 + Bu + vw^2)^2}, \tag{2.36}$$

reducing to the vacuum case for $w = 1$. Fig. 2.6 has been plotted for this variation ($m = v = \rho = 1$ and $u = -2$). The closer view in Fig. 2.6a shows that as w drops from unity, the deflection increases; Fig. 2.6b indicates how massive its effect is as $w \to 0$.

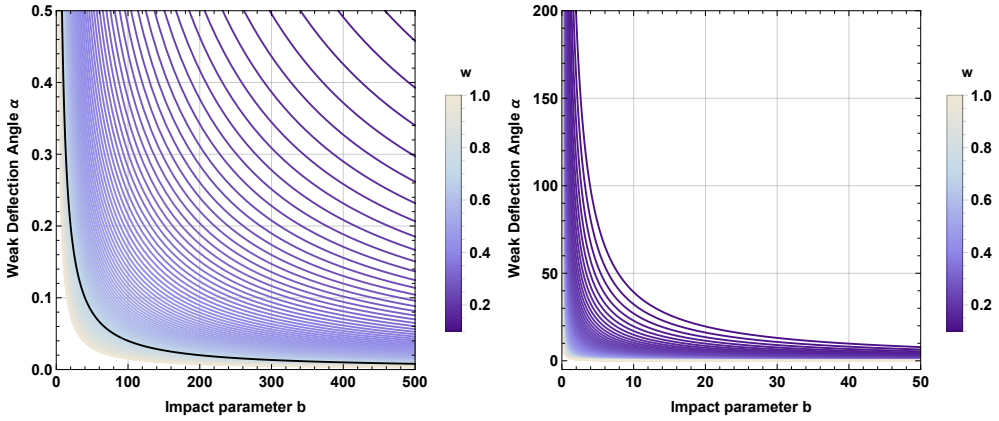

(a) Detailed view (b) Overall view

Figure 2.6: $\hat{\alpha}$ vs b for varying w ($M = 1$).

2.3 Literature Survey

Gibbons and Werner strategically demonstrated in 2008 that GBT can be used to calculate the bending angle in weak limits for asymptotically flat optical spacetimes [7]. Both the source and the observer were believed to be in asymptotic settings. Next, Crisnejo and Gallo demonstrated that the plasma medium deflects photons [50]. Furthermore, Keeton and Petters have presented an extensive analytical framework for the lensing phenomenon induced for Braneworld black holes characterized by the Garriga-Tanaka metric [51]. Virbhadra demonstrated that simply observing relativistic images can yield an exceptionally precise estimation of the upper limit on the compactness of massive dark objects [52]. Virbhadra's further research revealed the existence of a distortion parameter, capable of causing the summation with signs of all images produced by singular lensing of an object to vanish completely. This finding was verified through the examination of images depicting Schwarzschild lensing under both strong and weak gravity conditions [24].

In their study, Walia et al. employed the Gauss-Bonnet theorem to examine the gravitational bending of light caused by rotating black holes within the framework of

Horndeski gravity [53]. Li and Jia conducted a study on the charged-particle deflection that moves within the equatorial plane of Kerr-Newman spacetime. This investigation, performed in the weak field limit, utilized Jacobi geometry and the Gauss-Bonnet theorem as outlined in [43]. In [54], the authors collaborated with Liu to find the deflection and gravitational lensing of light and massive particles using the Gauss-Bonnet theorem in an arbitrary static, spherically symmetric, and asymptotically flat (anti-)de Sitter spacetime. Ali and Kaushal modified Kerr-Newman black holes in order to obtain precise solutions for rotating black holes within the framework of Eddington-inspired Born-Infeld gravity [53].

The Extended Uncertainty Principle was applied to discuss the dark matter consequences on a Schwarzschild black hole in [55]. In [31], the authors discussed the effects of nonlinear electrodynamics on non-rotating black holes parametrized by the field coupling parameter and magnetic charge parameter using the Gauss-Bonnet theorem under the influence of the Generalized Uncertainty Principle. Fu et al. deliberated on two black hole solutions based on two types of Non-linear electrodynamic (NLED) models, Euler-Heisenberg NLED model and the Bronnikov NLED model [56]. In the work presented in [2], the authors probed lensing by asymptotically flat black holes within the context of Horndeski theory. By utilizing GBT, they derived the deflection angle for both free-space and plasmatic environments. In their publication [57], the researchers explored the phenomenon of lensing by asymptotically flat black holes within the context of Horndeski theory. To determine the deflection angle in both vacuum and plasma environments, they applied the Gauss-Bonnet theorem. Pantig and Rodulfo present the deflection angle of a dirty black hole in [58]; fundamentally, a Schwarzschild black hole of mass encompassed by a surrounding presence of dark matter.

In [59], Li and Övgün sought out to determine the bending angle experienced by relativistic massive particles when interacting with a Kerr-like black hole in the weak field limits of the bumblebee gravity model. The complementary approach proposed by Gibbons and Werner, in conjunction with the conventional geodesic method, was examined in relation to the behaviour of light rays in the Kerr-Newman spacetime. The investigation primarily focused on the asymptotically flat scenario, as demonstrated in [60] by Li and Zhou.

In [3], Kumaran and Övgün have offered a more detailed summary of all the works related to lensing, a part of which is presented below.

2.3.1 Meta-analysis

To compare and contrast, some selected works have been tabulated in the following sections. Table (2.1) shows how the deflection angle varies in different paradigms. It is significant that any term subsidiary to $4M/b$ shapes the deflection angle to the desired case, implying that the GBT is extremely adaptable.

2.3.2 Plasma

Observations from the Event Horizon Telescope [20, 21, 33] qualify plasmatic influences as more significant than ever before. Revisiting Table (2.1), the effect of plasma on the corresponding black holes is examined for the second half and re-tabulated in Table (2.2).

The presence of the plasma term is evident in all scenarios, such that when $\omega_e/\omega_\infty \to 0$, the aforementioned expressions reduce to their non-plasmic equivalents. Consequently, the impact of the plasma becomes distinctly observable, as visually demonstrated by [61].

Gaussian curvature	**Deflection angle**
Weyl correction of a Schwarzschild black hole [62]	
$\mathscr{K} = -\frac{2M}{r^3} + \frac{3M^2}{r^4} - \frac{72M\alpha}{r^5}$	$\hat{\alpha} = \frac{4M}{b} + \frac{15\pi M^2}{4b^2} + \frac{32M\alpha}{b^3} + \frac{261\pi M\alpha}{4b^4}$
Schwarzschild-like solution in Bumblebee gravity [62]	
$\mathscr{K} = -\frac{2M}{(1+l)r^3}$	$\hat{\alpha} = \frac{4M}{b} + \frac{\pi l}{2} - \frac{2Ml}{b}$
Rindler-modified Schwarzschild black hole [63]	
$\mathscr{K} = -\frac{2\mu}{r^3}\left[f + \frac{\mu}{2r} - \frac{4\pi r^3}{\mu}F(\rho, f, p, \mu)\right]$	$\hat{\alpha} = \frac{0.126127529}{\sqrt{a^3 b^7}}$
Reissner-Nordström black hole [64] with topological defects	
$\mathscr{K} = -\frac{2M}{r^3}\left(1 - \frac{3M}{2r}\right) + \mathscr{O}(Q^2, r^4)$	$\hat{\alpha} = \frac{4M}{b} + 4\mu\pi - \frac{3\pi Q^2}{4b^2} + 4\pi^2\eta^2$
Einstein-Maxwell-Dilaton-Axion [65] (EMDA) black hole	
$\mathscr{K} = -\frac{2M}{r^3} + \frac{3M^2}{r^4} - \left(\frac{6M}{r^4} - \frac{12M^2}{r^5}\right) r_0$	$\hat{\alpha} = \frac{4M}{b} + \frac{3M\pi}{2b^2}$
Regular black holes with cosmic strings (RBCS) [46]	
$\mathscr{K} = -\frac{2M_0}{r^3} + \frac{3M_0^2}{r^4}$	$\hat{\alpha} = \frac{4M}{b} + 4\pi\mu$
Non linear electrodynamic (NLED) black hole [66]	
$\mathscr{K} = -\frac{2M}{r^3} + \frac{3Q^2}{r^4} - \frac{4MQ\alpha}{r^3}$	$\hat{\alpha} = \frac{4M}{b} - \frac{3\pi Q^2}{4b^2} + \frac{20MQ\alpha}{b}$

Table 2.1: $\hat{\alpha}$ for different black holes

Gaussian curvature	**Deflection angle**
Einstein-Maxwell-Dilaton-Axion black hole [65]	
$\mathscr{K} = \frac{M\left(\omega_e^2 r - 2\omega_\infty^2 r + 4r_0\omega_e^2 - 6r_0\omega_\infty^2\right)\omega_\infty^2}{\left(\omega_e^2-\omega_\infty^2\right)^2 r^4}$	$\hat{\alpha} = \frac{4M}{b} + \frac{3Mr_0\pi}{2b^2} + \frac{4M}{b}\frac{\omega_e^2}{\omega_\infty^2} + \frac{5\pi M r_0}{4b^2}\frac{\omega_e^2}{\omega_\infty^2}$
Regular black holes with cosmic strings [46]	
$\mathscr{K} = \frac{M\left(\omega_e^2 - 2\omega_\infty^2\right)\omega_\infty^2}{\left(\omega_e^2-\omega_\infty^2\right)^2 r^3} - \frac{3M^2\left(\omega_e^2+\omega_\infty^2\right)\omega_\infty^4}{\left(\omega_e^2-\omega_\infty^2\right)^3 r^4}$	$\hat{\alpha} = \frac{4M}{b} + 4\pi\mu + \frac{4M}{b}\frac{\omega_e^2}{\omega_\infty^2}$
Non linear electrodynamic black hole [66]	
$\mathscr{K} = \frac{M}{r^3}\left(-2 - \frac{\omega_e^2}{\omega_\infty^2} + \frac{2\omega_e^4}{\omega_\infty^4}\right) + \frac{2MQ^2}{r^5}\left(1 - \frac{17\omega_e^2}{\omega_\infty^2} + \frac{5\omega_e^4}{\omega_\infty^4}\right) - \frac{4MQ\alpha}{r^3}\left(1 + \frac{\omega_e^2}{\omega_\infty^2} - \frac{3\omega_e^4}{\omega_\infty^4}\right)$	$\hat{\alpha} = \frac{4M}{b} - \frac{3Q^2\pi}{4b^2} + \frac{4MQ\alpha}{b} + \frac{2M}{b}\frac{\omega_e^2}{\omega_\infty^2} + \frac{2MQ\alpha}{b}\frac{\omega_e^2}{\omega_\infty^2} - \frac{6M}{b}\frac{\omega_e^4}{\omega_\infty^4} - \frac{3Q^2\pi}{4b^2}\frac{\omega_e^4}{\omega_\infty^4}$

Table 2.2: Effect of homogenous plasma on $\hat{\alpha}$ due to different black holes

Chapter 3

EXTENDED UNCERTAINTY PRINCIPLE BLACK HOLE

One of the fundamental puzzles associated with black holes is the information paradox. According to the principles of quantum mechanics, particle information or its specific state while falling into a black hole should be preserved. The quantum wave function, which encodes the particle's characteristics, is believed to persist on the black hole's surface for an extremely long time. However, in 1974, Stephen Hawking proposed that black holes emit Hawking radiation as they gradually lose mass and energy over time [67]. This implies that the information of the swallowed object eventually dissipates with the black hole due to its finite temperature. This contradiction between quantum mechanics and general relativity gives rise to the information paradox.

Hawking provided the explanation that seemed most likely out of the few hypotheses that resolved the information paradox. He proposed that the information contained in the falling objects might be able to avoid being sucked into the black hole by escaping through quantum fluctuations from the radiation field of the object. The information from the particle (possibly distorted) gets captured in the radiation as it leaves the body and returns to the universe. For the spacetimes of these fluctuations in the event horizon to be consistent, quantum-gravity corrections are necessary. These quantum effects suggest that black holes adhere to quantum theory. This chapter is dedicated to one such black hole as in [1].

3.1 EUP Black Hole

Think of a hydrogen atom: the electron's kinetic energy prevents it from collapsing into the nucleus by counteracting its negative potential energy. Heisenberg introduced the uncertainty principle. In light of the fact that a black hole is now understood to be a quantum entity, Adler contends to the Generalized Uncertainty Principle [68] preventing it from dissipating. The Heisenberg relation mathematically includes an additional term proportional to the square of momentum uncertainty. As an alternative, the Extended Uncertainty Principle (EUP) can be obtained by adding an additional term to the Heisenberg relation that is proportional to the square of position uncertainty. The size of the black hole's photosphere, its properties, and other information can be determined on a large scale if the EUP corrections' contribution is sufficient etc.

The Heisenberg relation with the position uncertainty corrected for EUP for a fundamental distance scale, L [69] can be written as:

$$\Delta x\, \Delta p \geq 1 + \alpha \left(\frac{\Delta x^2}{L^2} \right), \tag{3.1}$$

where α is a coupling constant. The condition $L \gg \Delta x$ ensures that the uncertainty principle can still be retrieved. It also indicates that [70] quantum gravity's effects can be witnessed over very large distances, promoting the idea that quantum effects can be identified on macroscopic scales. According to [71], the solution of a EUP- corrected spherically symmetric black hole with mass M is:

$$f(r)\Big|_{EUP} = 1 - \frac{2M}{r} \left(1 + \frac{4\alpha M^2}{L^2} \right). \tag{3.2}$$

For the distance of closest approach r_0, if $M/r_0 \ll 1$, the deflection angle in this scenario is minuscule, indicating the occurrence of weak deflection lensing [72]. As the distance r_0 approaches the photosphere, the deflection angle α gradually increases until it reaches a point of divergence, leading to strong deflection lensing. The lapse

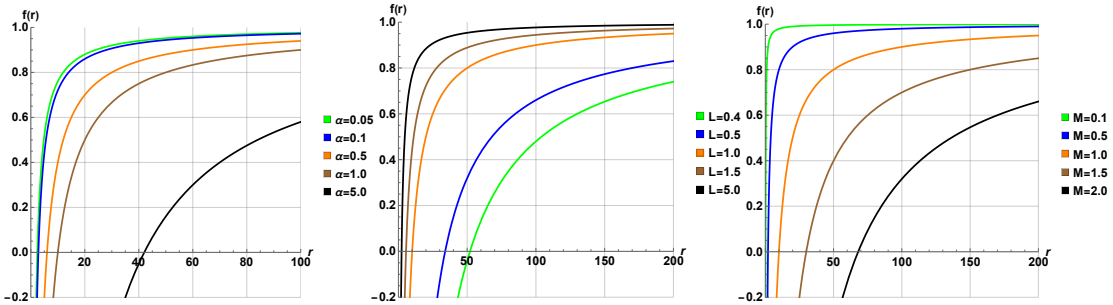

(a) Varying α; $M = 1$; $L = 1$ (b) Varying L; $M = 1$; $\alpha = 1$ (c) Varying M; $\alpha = 1$; $L = 1$

Figure 3.1: The lapse function of the EUP black hole.

function of $f(r)$ for a EUP black hole for different α, L, and M are given in Fig. 3.1. The mass shows a gradual progression in Fig. 3.1a. with increasing values, whereas, Figs. 3.1b and 3.1c show a drastic change for both $\alpha > 1$ and $L > 1$.

This gives:

$$\mathscr{K} = \frac{\mathscr{R}}{2} \approx -\frac{8M^3\alpha}{r^3L^2} - \frac{2M}{r^3} + \mathscr{O}(M^4). \tag{3.3}$$

Ignoring the higher-order terms, this simplifies to the following expression for the deflection angle due to weak lensing with EUP corrections:

$$\hat{\alpha} = \frac{4M}{b} + \frac{16M^3\alpha}{bL^2}, \tag{3.4}$$

in vacuum for limits in weak fields. As a result, the EUP parameter $alpha$ enhances the deflection angle, and when $\alpha = 0$ the deflection angle declines to that of a Schwarzschild black hole. It appears that the leading order terms' deflection angle agrees with [55]. Fig. 3.2a portrays this expression for a range of α.

3.2 Massive Particles

The deflection angle for a EUP black hole enveloped with massive particles is:

$$\begin{aligned}\hat{\alpha} = M^3 \left(\frac{16}{3b^3v^6} - \frac{40}{3b^3v^4} + \frac{10}{b^3v^2} + \frac{2}{3b^3} + \frac{8\alpha}{bL^2} + \frac{8\alpha}{bL^2v^2} \right) \\ + \frac{\pi M^2 \left(v^4 + 6v^2 - 4\right)}{4b^2v^4} + \frac{2M\left(v^2+1\right)}{bv^2}.\end{aligned} \tag{3.5}$$

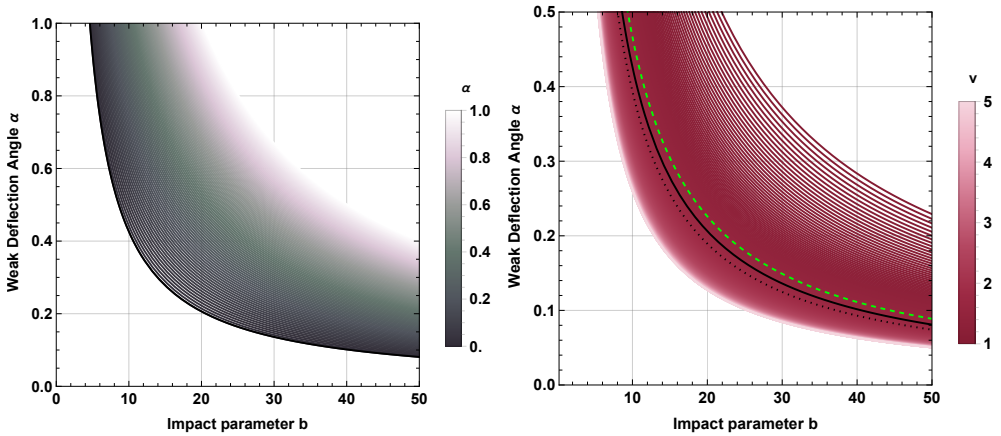

(a) Vacuum; varying α (b) Massive particles; varying v

Figure 3.2: $\hat{\alpha}$ vs b ($\mu = 2$). The solid black line is the Schwarzschild case with $M = 1$. On the right, the dotted black line shows the case of a Schwarzschild black hole surrounded by massive particles; the dashed green line depicts the vacuum case of the EUP black hole ($M = 1$, $\alpha = 0.05$, and $L = 1$.

This is exhibited by Fig. 3.2b. It is fascinating to observe that imposing a quantum correction shows a considerable increase in the deflection angle for low values of v. The decrease in $\hat{\alpha}$ for when $v^2 \geq \alpha$ and continues to drop till unity.

3.3 Plasma

The refractive index $n(r)$ for an EUP-corrected black hole is derived as [50],

$$n(r) = \sqrt{1 - \frac{\omega_e^2}{\omega_\infty^2}\left[1 - \frac{2M}{r}\left(1 + \frac{4\alpha M^2}{L^2}\right)\right]}. \tag{3.6}$$

As a result of plasma, the deflection angle is found to be:

$$\hat{\alpha}_{w_n} \approx \frac{4M}{b} + \frac{2M\omega_e^2}{b\omega_\infty^2} + \frac{16\alpha M^3}{bL^2} + \frac{8\alpha M^3\omega_e^2}{bL^2\omega_\infty^2}. \tag{3.7}$$

In Fig.3.2a, Eq. (3.7) is plotted for minimal values of the impact parameter, it becomes apparent that the quantum effects have an influence on the deflection angle. It is clear that these effects do make an impression, as demonstrated by the EUP parameter α). Thus, it is clear that when photon rays pass through a homogeneous plasma medium, the deflection angle increases. From the typical $\hat{\alpha}_w$, which boils down to vacuum without the EUP corrections, the graph illustrates a notable rise in the deflection angle

for the plasmatic medium. even though all the behaviors appear to be closely aligned for high impact parameters. Eq. (3.7) can eliminate the effect of plasma as $\omega_e/\omega_\infty \to 0$ to acquire the standard case.

In a weak field approach, the deflection angle of a EUP black hole in equation 3.7 mitigates to the following form:

$$\hat{\alpha}_{w_n} \approx \frac{4M(1+\alpha)}{l^2 b} + \frac{2M\omega_e^2}{b\omega_\infty^2} + \frac{8\alpha M^3\omega_e^2}{bL^2\omega_\infty^2}, \tag{3.8}$$

where $l = 2M/L$. Here, the leading term is observed to be equivalent to the post-Newtonian approach deflection angle, $\alpha_{\text{PPN}} = 2(1+\xi)M/b$. The lower bound of the EUP parameter can be determined as follows: $L \gtrsim 9.1 \times 10^5$m [71]. By comparing the EUP black hole's deflection angle without plasma's influence, deriving $\xi - 1 = 2l^2$, with the solar system limit of $|\xi - 1| \lesssim 2.1 \times 10^{-5}$, gives $L \gtrsim 9.1 \times 10^5$m.

The focus of this work is on uniform, regular plasma. This can be enhanced by combining this most extreme example of the magnetized plasma with the examples of homogeneous and inhomogeneous cases as shown [73] by the "Zeeman effect," which can be extended to deal with magnetic effects.

3.4 Dark Matter

Following the calculation of $\mathscr{K}$ from the refractive index, the deflection angle is:

$$\hat{\alpha} = \frac{768ML^2\left(2vw^2(Bu+1)+2Bu+1\right)}{192bL^2\left(Bu+vw^2+1\right)^2}. \tag{3.9}$$

Fig. 3.3b is plotted for a EUP black hole surrounded by dark matter. This is a rather messy variation with a significant decrease in the deflection angle from the Schwarzschild case, falling to the negative range for intermediate values for w, and then rising toward the Schwarzschild case approaching it more closely. Negative deflection implies that the bending of thr light ray is away from the gravitating object.

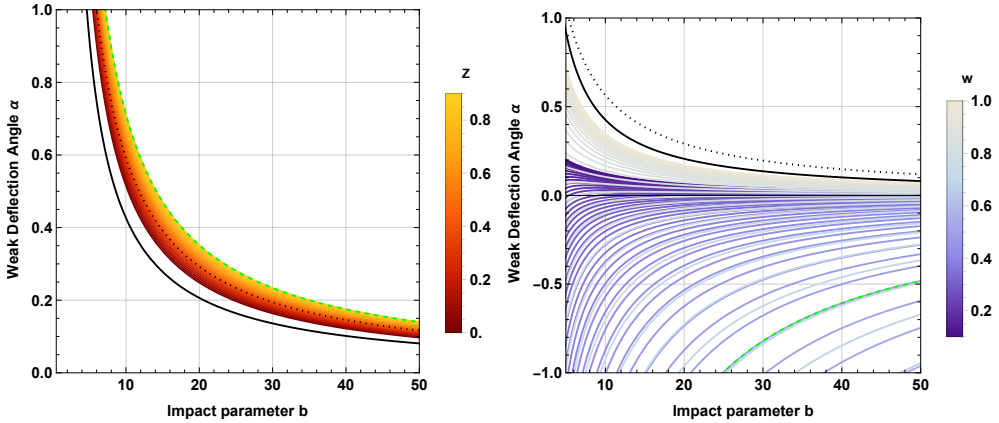

(a) Plasma case; varying z (b) Dark matter case; varying w

Figure 3.3: $\hat{\alpha}$ vs b in the presence of a medium for $\mu = 2$. The solid black line is the Schwarzschild case with $M = 1$; the dotted black line shows the case of a Schwarzschild black hole surrounded by the same medium; the dashed green line depicts the vacuum case of the EUP black hole.

3.5 Observables

In this section, gravitational lensing observables including positions, magnifications, and differential time delays between lensed images are obtained. Note: in the context of the weak deflection limit, the gravitational lensing effects considered in this study involve a circumstance where a massive compact object (referred to as the lens L) is positioned between an observer (O) and a point source of light (S). This arrangement takes place within an asymptotically flat region of spacetime, as depicted in Fig.3.4. The lens equation, also known as the ray-tracing equation, for this particular case, involves the angular positions of the images denoted as θ, along with the actual position of the source represented as β. It can be expressed as follows: [71]:

$$\tan\beta = \tan\theta - D\,\left[\tan\theta + \tan(\hat{\alpha} - \theta)\right], \tag{3.10}$$

where D is the ratio of the distance from the lens to the source, d_{LS} and the distance from the observer to the source, d_S: $D \equiv d_{LS}/d_S$. For weak-lens approximation ($\alpha D_s \simeq \hat{\alpha} D_{ds}$), the above lens equation ($\beta = \theta - \frac{D_{ds}}{D_s}\hat{\alpha}(\theta)$) becomes [71]:

$$\beta = \theta - \left(1 + \alpha^2\right)\frac{\theta_{\rm E}^2}{\theta}, \tag{3.11}$$

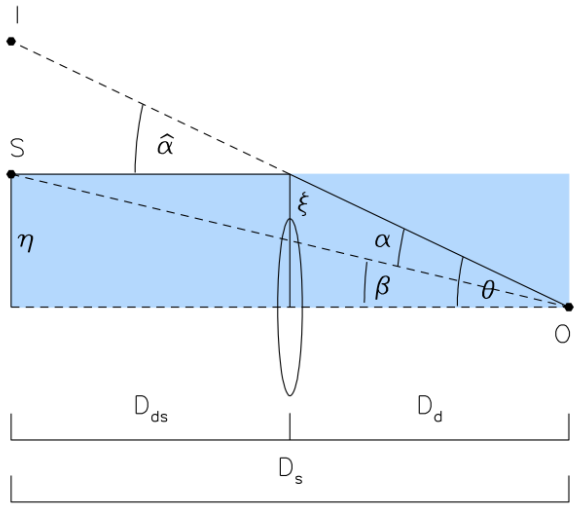

Figure 3.4: Lens geometry.

where the impact parameter, $b = D_d\theta$ and θ_E Einstein angle for the EUP black hole: for the position consistent with $\beta = 0$, it is:

$$\theta_{\mathrm{E}} = \sqrt{\frac{4MD_{\mathrm{LS}}}{D_{\mathrm{L}}D_{\mathrm{S}}}}, \tag{3.12}$$

and the Einstein radius

$$R_E = \theta_E D_d. \tag{3.13}$$

Using the Einstein angle 3.12 in 3.11, to get $\beta\theta = \theta^2 - \theta_E^2$. Then corresponding angular position of images are obtained as follows:

$$\theta_{\pm} = \frac{1}{2}[\beta \pm \sqrt{\beta^2 + 4\,(1+\alpha^2)\,\theta_{\mathrm{E}}^2}], \tag{3.14}$$

and the angular separation between the two images are

$$\Delta\theta = \theta_+ - \theta_- = \sqrt{\beta^2 + 4\,(1+\alpha^2)\,\theta_{\mathrm{E}}^2}. \tag{3.15}$$

In the presence of plasma:

$$\theta = \frac{1}{2}(\beta \pm \sqrt{\beta^2 + 4\tilde{\Theta}_{\pm}^2}), \tag{3.16}$$

with

$$\tilde{\Theta}_{\pm} = \theta_E \sqrt{\frac{1}{2}\left\{1 + \left[1 - \frac{\omega_e^2}{\omega_\infty^2}\left(1 - \tilde{\xi}(1+\alpha l^2)\right)\right]^{-1}\right\}}. \tag{3.17}$$

When the source, lens, and observer are precisely aligned, with $\beta = 0$, the resulting image of the source takes the form of the well-known Einstein ring, according to [74]. As a result of utilizing Eq. (3.17) and repeating the calculations, it becomes apparent that plasma causes a shift in the images' angular positions [73], as shown in Fig. 3.3a. In the case of an Einstein ring, the vicissitudes of plasma are unique [50].

The magnification, denoted as $\mu(\theta)$, of the images, occurs due to the phenomenon of light bending caused by the lens. This bending concentrates a greater number of light rays from the source within a specific solid angle at the observer's position, resulting in an enhanced brightness and intensity of the image. It is defined by [71]

$$\mu(\theta) = \left[\frac{\sin\beta}{\sin\theta}\frac{d\beta}{d\theta}\right]^{-1}, \tag{3.18}$$

and the magnification is:

$$\mu_{\pm} = \frac{\beta^2 + 2\left(1+\alpha^2\right)\theta_{\mathrm{E}}^2}{2\beta\sqrt{\beta^2 + 4\left(1+\alpha^2\right)\theta_{\mathrm{E}}^2}} \pm \frac{1}{2}. \tag{3.19}$$

The time delay, which serves as a significant observable in the context of weak gravitational lensing, can be computed using the subsequent equation: [71]

$$T = \int_{R_{\mathrm{src}}}^{r_0} \frac{\mathrm{d}t}{\mathrm{d}r}\mathrm{d}r + \int_{r_0}^{R_{\mathrm{obs}}} \frac{\mathrm{d}t}{\mathrm{d}r}\mathrm{d}r, \tag{3.20}$$

where,

$$\frac{\mathrm{d}t}{\mathrm{d}r} = \frac{\sqrt{f(r)^{-1}r^2 f(r_0)}}{f(r)\sqrt{r_0}\sqrt{\frac{r^2}{r_0}\frac{f(r_0)}{f(r)} - 1}}, \tag{3.21}$$

and using $b = D_{\mathrm{L}}\sin\theta$ the respective differential time delay for the EUP black hole is:

$$\begin{aligned}\Delta T &= T_+ - T_- \\ &= 4M\left[\frac{\beta}{2\theta_{\mathrm{E}}^2}\sqrt{\beta^2 + 4\left(1+\alpha^2\right)\theta_{\mathrm{E}}^2} + \left(1+\alpha^2\right)\ln\left(\frac{\sqrt{\beta^2 + 4\left(1+\alpha^2\right)\theta_{\mathrm{E}}^2} + \beta}{\sqrt{\beta^2 + 4\left(1+\alpha^2\right)\theta_{\mathrm{E}}^2} - \beta}\right)\right].\end{aligned} \tag{3.22}$$

Chapter 4

ASYMPTOTICALLY FLAT BLACK HOLE IN HORNDERSKI THEORY

After Einstein's theory of general relativity (GR), Hubble demonstrated that the universe was expanding, Hubble's observations provided compelling evidence for the Big Bang theory and raised the possibility of its potentially infinite nature. However, the observable portion of the universe is limited by the maximum distance that light can travel from the farthest edge to reach Earth. In basic terms, the gravitational constant G undergoes changes over time due to the evolving mass distribution and size of the universe [75]. This disparity speculated G as a scalar field rather than a constant number. The so-called metric field, according to Einstein's formulation, includes the impact of gravity and its mathematical terminology is tensor. the scalar-tensor theory pertains to the idea of incorporating a scalar field resulting from mass distribution into the metric. Several references, namely [76, 77], contribute to this understanding. Among the various gravitational scalar-tensor theories, the Horndeski theory stands out as a representative example [78]. Incorporating a scalar field as an additional degree of freedom within the framework of a four-dimensional spacetime, the Lagrangian of the system is modified to include this scalar field, resulting in second-order field equations of motion. This idea is based on the Lovelock theory of gravity: unwinding his assumptions tests the scalar-tensor theory and expands GR simultaneously. The action principle in four dimensions $n = 4$ is [79, 80]:

$$I[g_{\mu\nu},\varphi] = \int \sqrt{-g}\, d^4x \left[k\,(R-2\Lambda) - \frac{1}{2}\left(\alpha g_{\mu\nu} - \eta G_{\mu\nu}\right) \nabla^\mu \varphi \nabla^\nu \varphi \right], \tag{4.1}$$

where, $k \equiv 1/16\pi G$. The first term of this equation represents the contribution of the scalar field with a non-minimal coupling to matter, which is influenced by the Ricci scalar while the second one accounts for the Einstein-Hilbert action for the cosmological constant Λ. The positive energy density of the matter field governs the values of the parameters α and η.

The formula that follows is a simplified version of the action that was studied using normal matter and fields [80]: Using the presumptions that in the context of a static, spherically symmetric, and homogeneous geometry, where both the scalar and metric fields exhibit this symmetry in asymptotically flat spacetime, the equation presented can be regarded as the specific limit to the Horndeski theory. The following work is built on the foundation of Eq. (4.1).

The discovery of GW170817 by multi-messenger astronomy significantly restricted the scalar-tensor theories. When two neutron stars spiralling around each other eventually amalgamated, the arrival times of both gravitational waves and their corresponding electromagnetic counterparts originating from the NGC 4993 galaxy were observed to exhibit a temporal shift of less than a minute. Ergo, coupling the scalar field to the curvature reveals that the speed of gravitational waves is influenced. In order to align with these observations, the quintic and quartic models are disregarded, restricting our calculations to linear observables. It is worth noting that Horndeski theories have a major drawback related to their primordial tensor spectrum: the gravitational wave speed is not equal to unity. The discovery of GW170817, for instance, invalidates the use of Horndeski theory in explaining

phenomena that occur in the later stages of the universe. [81]. These theories can be modified using a new framework created in [82, 83]. In this chapter, the primary goal is to test the validity of the modified gravity theory via the Gauss-Bonnet theorem by studying black hole lensing in the context of Horndeski theory as in [2].

4.1 Asymptotically Flat Black Holes

A new asymptotically locally flat black hole can be discovered when the action includes a cosmological term. In this case, the kinetic term (constructed with Einstein tensor) of the scalar field alone is considered to yield the matter term in the action, which reduces the latter to $\alpha = 0$.

$$I[g_{\mu\nu}, \varphi] = \int \sqrt{-g} d^4x [k(R - 2\Lambda) + \frac{\eta}{2} \mathscr{G}_{\mu\nu} \nabla^\mu \varphi \nabla^\nu \varphi]. \tag{4.2}$$

In [82], The authors obtained an equation using slow-roll conditions that incorporated the implications of the GW170717 study results, which was additionally streamlined by [83]: The action appears to have gained an additional term equal to $\varphi\mathscr{G}$ where:

$$\mathscr{G} = R^2 - 4R_{\mu\nu}R^{\mu\nu} + R_{\mu\nu\rho\sigma}R^{\mu\nu\rho\sigma}. \tag{4.3}$$

Determining the integral for $K \neq 0$ [79]:

$$\mathrm{d}s^2 = -H(r)\ \mathrm{d}t^2 + \frac{15\left(-2K + \Lambda r^2\right)^2}{K} \frac{\mathrm{d}r^2}{H(r)} + r^2\ \mathrm{d}\Sigma_{K,2}^2, \tag{4.4}$$

where $\mathrm{d}\Sigma_{K,2}^2 = \mathrm{d}\theta^2 + \sin^2\theta\ \mathrm{d}\phi^2$ and

$$H(r) = (60K^2 - 20\Lambda K r^2 + 3\Lambda^2 r^4) - \frac{\mu}{r}. \tag{4.5}$$

If Λ vanishes, the scalar field dissipates reducing the solution to the topological Schwarzschild solution in a flat spacetime [79]. By taking $\Lambda = 0$:

$$\mathrm{d}s^2 = -H(r)\ \mathrm{d}t^2 + \frac{60K}{H(r)}\ \mathrm{d}r^2 + r^2\ \mathrm{d}\Sigma_{K,2}^2, \tag{4.6}$$

and

$$H(r) = 60K^2 - \frac{\mu}{r}. \tag{4.7}$$

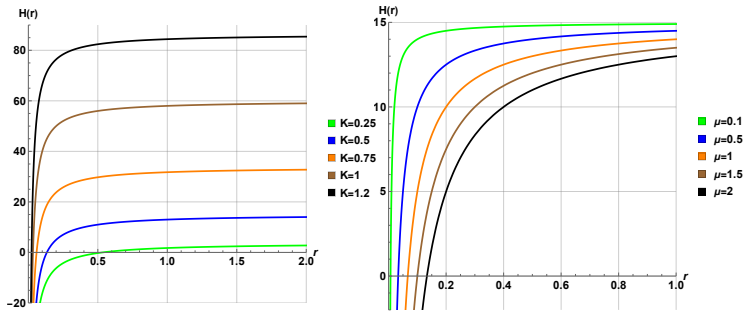

(a) Varying K; $\mu = 2$ (b) Varying μ; K = 0.5

Figure 4.1: Lapse function for asymptotically flat black holes in Horndeski theory.

Here, μ is the integration constant and can be expressed as the mass of a black hole. The lapse function of $H(r)$ for different K, and μ are given in Fig. 4.1. The nature of Fig. 4.1a infers that K has an almost constant variation for $K = 0.5$, whereas, Figs. 4.1b infers a typical change for μ.

Following the calculation of non-zero Christoffel symbols, the optical metric's Gaussian optical curvature is:

$$\mathscr{K} = -\frac{K\mu}{r^3} + \frac{\mu^2}{80Kr^4} + \mathscr{O}(r^{-5}). \tag{4.8}$$

and the weak deflection angle in vacuum for an asymptotically flat black hole in Horndeski theory by plugging Eq. 4.8 into Eq. 2.16:

$$\hat{\alpha} = \frac{2K\mu}{b} + \frac{\mu^2\pi}{320Kb^2} + \mathscr{O}(\mu^3). \tag{4.9}$$

The weak deflection angle is reduced to Schwarzschild deflection angle if $K = 2$ up to the first order term. It can be seen from the second term in the above equation that the second and higher-order terms deviate from the Schwarzschild case.

Graphically reviewing $\hat{\alpha}$ of asymptotically flat black holes and demonstrating their physical meaning to investigate the influence of curvature constant K and impact parameter b for the black hole's stable and unstable states, Figure 4.1 shows that $\hat{\alpha}$

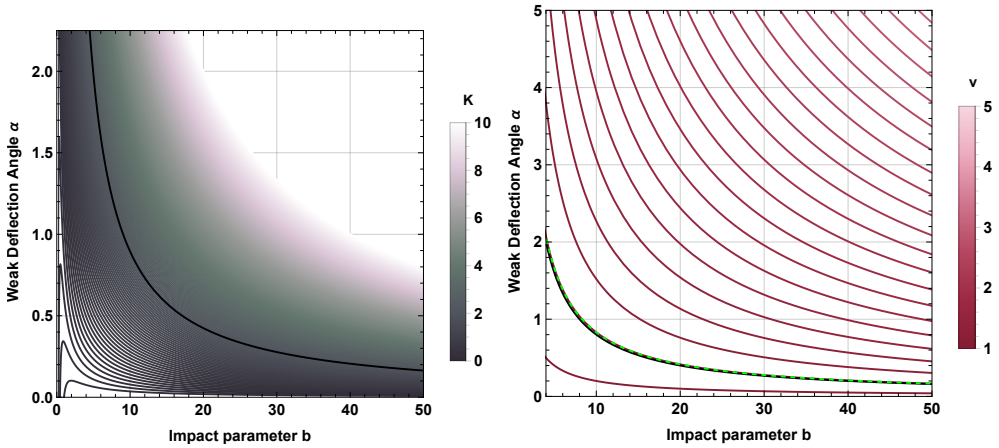

(a) Vacuum; varying K (b) Massive particles; varying v

Figure 4.2: $\hat{\alpha}$ vs b. The solid black line is the deflection angle for a Schwarzschild black hole with $M = 1$. On the right, the dotted black line shows the case of a Schwarzschild black hole surrounded by massive particles; the dashed green line depicts the vacuum case of the asymptotically flat black hole.

plotted against b for varying K and $\mu = 2$. One can see that for small b, the deflection angle increases, but for fixed μ, the deflection angle decreases. A locally hyperbolic behaviour is expected when K is obtained and a locally flat behaviour for when $K = 0$. If the variation of K is small, $\hat{\alpha}$ decreases significantly and as K grows, $\hat{\alpha}$ reduces progressively as it approaches positive infinity. Only when $K \geq 0.5$, a physically stable behaviour is noticed. The distant view of $\hat{\alpha}$ variation in Fig. 4.2b shows decreased deflection for $K < 2$ and increased deflection for $K > 2$; $K = 2$ overlaps with the Schwarzschild case.

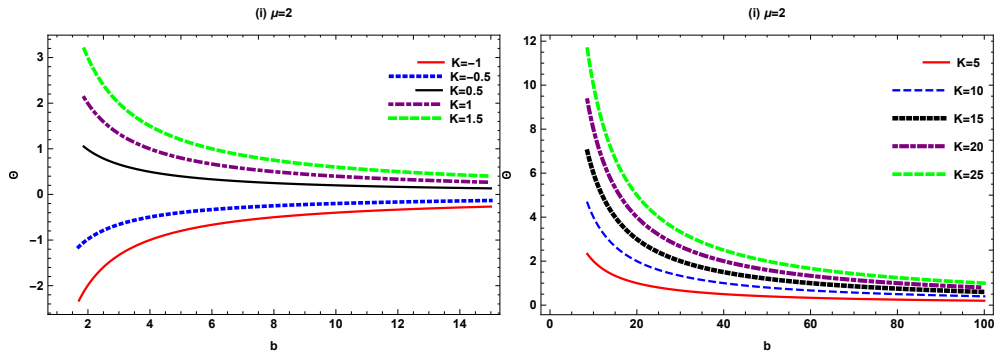

Fig. 4.2: Closer look of $\hat{\alpha}$ versus b for varying K.

4.2 Massive Particles

The Gaussian curvature is derived to be:

$$\mathscr{K} = \mu^2 \left(\frac{\left(6\left(60v^2-60\right)^2\left(240v^4-480v^2+240\right)-10\left(v^2-1\right)\left(60v^2-60\right)^3K^3\right)}{7200r^4} + \frac{\left(\left(6\left(v^2-1\right)\right)\left(60v^2-60\right)^2-\left(180\left(v^2-1\right)\right)\left(240v^4-480v^2+240\right)\right)K}{7200r^4} + \frac{v^2-1}{(7200r^4)K^3} + \frac{v^4-2v^2+1}{(120r^4)K}\right) + \mu\left(\frac{v^2-1}{120Kr^3} - \frac{\left(v^2-1\right)^2K}{r^3} + \frac{90\left(v^2-1\right)^3K^3}{r^3}\right), \tag{4.10}$$

giving the deflection angle:

$$\hat{\alpha} = -\frac{\pi\mu^2}{320b^2K} - \frac{120K^3\mu}{b} + \frac{120K^3\mu v^2}{b} + \frac{2K\mu}{b}. \tag{4.11}$$

This variation shows decreased deflection for a very small range of v, increasing drastically (note the y-axis scale) as v climbs up to unity.

4.3 Plasma

In this section, the plasma affects photon lensing by asymptotically flat black holes in Horndeski theory is analyzed. The optical Gaussian curvature drawn from Eq. (2.5) is:

$$\mathscr{K} = -\frac{\mu K}{r^3} + \frac{\mu^2}{80Kr^4} + \frac{90\mu K^3}{r^3}\frac{\omega_e^2}{\omega_\infty^2} - \frac{9\mu^2K}{4r^4}\frac{\omega_e^2}{\omega_\infty^2} - \frac{3\mu K}{r^4} (60K^2r-\mu)\frac{\omega_e^2}{\omega_\infty^2} + \frac{\mu^3}{80Kr^5}\frac{\omega_e^2}{\omega_\infty^2} + \frac{3\mu^2(60K^2r-\mu)}{80Kr^5}\frac{\omega_e^2}{\omega_\infty^2}. \tag{4.12}$$

Simplifying:

$$\hat{\alpha} \simeq \frac{\mu^2\pi}{320b^2K} + \frac{\mu^3}{90b^3K}\frac{\omega_e^2}{\omega_\infty^2} + \frac{2\mu K}{b} - \frac{3\mu^2K\pi}{4b^2}\frac{\omega_e^2}{\omega_\infty^2} + \frac{180\mu K^3}{b}\frac{\omega_e^2}{\omega_\infty^2} + \mathscr{O}(\mu^4,K^4). \tag{4.13}$$

This shows that the photon rays are moving in plasma and is plotted in Figs. 4.3 to analyze the stable and unstable states of the black hole and to determine the effects of K, ω_e/ω_∞, and b on $\hat{\alpha}$ for fixed $\mu = 2$. For simplicity, supposing $\frac{\omega_e}{\omega_\infty} = z$. At $z = 0.005$, $\hat{\alpha}$ exhibits a decrease. Similarly, it is observed that the behaviour remains consistent for the transition from $z = 0.005$ to 0.01, and as z approaches 0.1, there is a

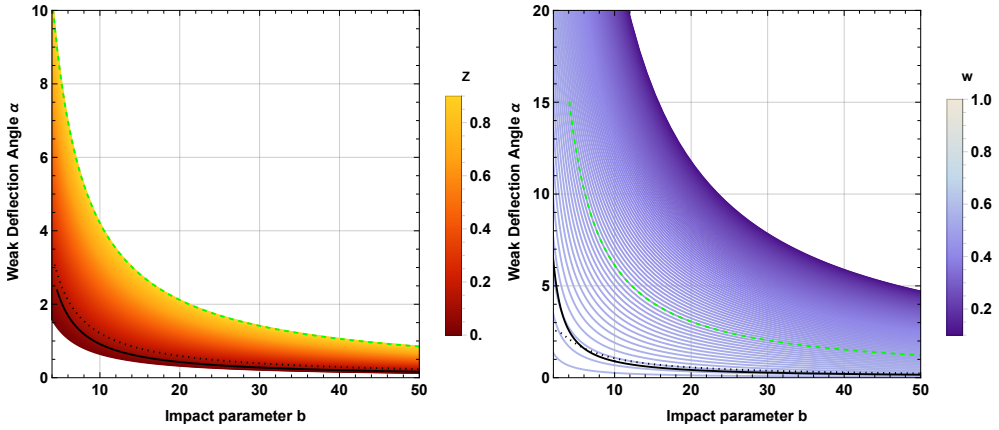

(a) Plasma case; varying z (b) Dark matter case; varying w

Figure 4.3: $\hat{\alpha}$ vs b in the presence of a medium. The solid black line is the Schwarzschild case with $M = 1$; the dotted black line shows the case of a Schwarzschild black hole surrounded by the same medium; the dashed green line depicts the vacuum case of the asymptotically flat black hole.

slight alteration in the deflection angle. However, beyond $z = 0.1$, the deflection angle gradually rises as the value of z increases. This is asserted by Fig. 4.3a.

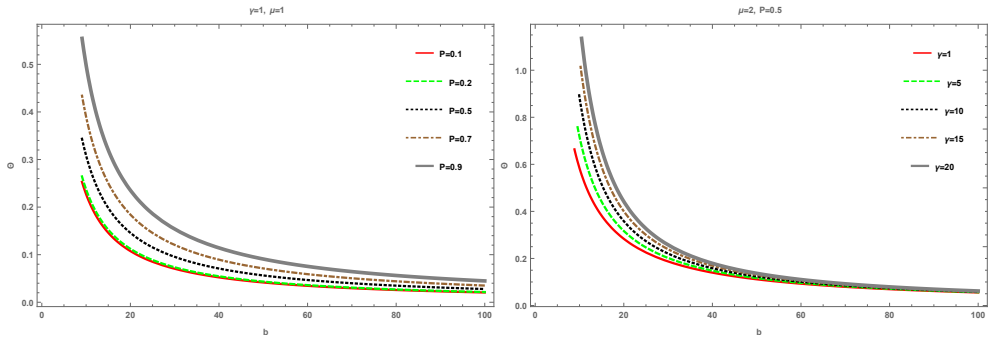

Fig. 4.3: Closer look of $\hat{\alpha}$ versus b for varying K.

4.4 Dark Matter

The deflection angle in the presence of dark matter is derived to be:

$$\hat{\alpha} = \frac{\pi\mu^2}{320b^2K} - \frac{\pi\mu^2 vw^2}{160b^2K} - \frac{3\pi\mu^2 u}{8b^2} + \frac{9\pi\mu^2 uvw^2}{8b^2} - \frac{240K^2\mu u}{b} + \frac{720K^2\mu uvw^2}{b} - \frac{4K\mu vw^2}{b} + \frac{2K\mu}{b}. \tag{4.14}$$

Fig. 4.3b shows a great increase in deflection as w decreases; for a few values of w close to unity, there is a small decrease in deflection.

Chapter 5

HORNDESKI BLACK HOLE

In the past, the idea of Modified Gravity was put forward as a prominent alternative to General Relativity, gaining considerable acceptance. Nevertheless, owing to theoretical intricacies and limitations in observations, this approach has been surpassed in recent times by the Scalar-tensor Theory. The Scalar-tensor Theory effectively combines the scalar field (representing mass) with the metric (describing gravity) [76–78].

Suppose a black hole that adheres to the comprehensive scalar-tensor theory in a four-dimensional spacetime, resulting in second-order equations of motion known as the Horndeski theory. The action can be expressed as follows: [80, 84]

$$S = \int \mathrm{d}^4x\sqrt{-g}\,\mathscr{L}, \tag{5.1}$$

with the generalised Galilean Lagrangean, $\mathscr{L} \equiv (\mathscr{L}_2 + \mathscr{L}_3 + \mathscr{L}_4 + \mathscr{L}_5)$ expanded as:

$$\mathscr{L}_2 = G_2 \tag{5.2}$$

$$\mathscr{L}_3 = -G_3\Box\phi \tag{5.3}$$

$$\mathscr{L}_4 = G_4\mathscr{R} + G_{4X}[(\Box\phi)^2 - (\nabla_\mu\nabla_\nu\phi)^2] \tag{5.4}$$

$$\mathscr{L}_5 = G_5G_{\mu\nu}\nabla^\mu\nabla^\nu\phi - \frac{G_{5X}}{6}[(\Box\phi)^3 - 3\Box\phi(\nabla_\mu\nabla_\nu\phi)^2 + 2(\nabla_\mu\nabla_\nu\phi)^3]. \tag{5.5}$$

G_i is an arbitrary function of the scalar field, ϕ and kinetic energy, $X \equiv -\partial_\mu\phi\partial^\mu\phi/2$, which depends on the curvature and coupling of the scalar field, and the subscript X refers to the derivative with respect to X, along with:

$$\Box\tilde{\varphi} \equiv g^{\mu\nu}\nabla_\mu\nabla_\nu\tilde{\varphi}$$
$$(\nabla_\mu\nabla_\nu\tilde{\varphi})^2 \equiv \nabla_\mu\nabla_\nu\tilde{\varphi}\nabla^\mu\nabla^\nu\tilde{\varphi} \tag{5.6}$$
$$(\nabla_\mu\nabla_\nu\tilde{\varphi})^3 \equiv \nabla_\mu\nabla_\nu\tilde{\varphi}\nabla^\nu\nabla^\sigma\tilde{\varphi}\nabla_\sigma\nabla_\mu\tilde{\varphi}.$$

The contemporary field of multi-messenger astronomy has made significant progress in detecting gravitational waves emanating from the merger of binary neutron stars (GW170817) [12]. This research has placed certain limitations on scalar-tensor theories. The observed discrepancy in arrival times between gravitational waves and electromagnetic waves, with a difference of approximately a minute, provides an opportunity to compare the characteristics of gravitational waves with their electromagnetic counterparts recorded during cosmological events. Such a comparison may potentially yield insights into the concept of cosmic acceleration, which could be attributed to modifications in scalar-tensor gravity within the framework of the Horndeski theory. The speed of gravitational waves have been shown to be affected by coupling the scalar field to curvature. To be in accordance with these observations, linear observables are specifically focused for the calculations; the cosmological solution and the equivalence principle associated with the quintic and quartic models are not to be neglected [85]. Therefore, the Horndeski black holes will be analyzed in this chapter as in [4].

5.1 Horndeski Black Holes

Considering the specific case of the action in which $G_2 = \eta X$, $G_4 = \zeta + \beta\sqrt{-X}$ and $G_3 = G_5 = 0$, where η and β are dimensionless parameters and $\zeta = M_{pl}^2/(16\pi)$, the action then takes on an explicit form

$$S = \int \sqrt{-g}\, d^4r \left\{ \left[\zeta + \beta\sqrt{\frac{\partial\tilde{\varphi})^2}{2}} \right] R - \frac{\eta}{2}(\partial\tilde{\varphi})^2 - \frac{\beta}{\sqrt{2(\partial\tilde{\varphi})^2}}[(\tilde{\varphi})^2 - (\nabla_\mu\nabla_\nu\tilde{\varphi})^2] \right\}. \tag{5.7}$$

The Einstein-Hilbert part of the action is given by the coefficient ζ; one of the parameters η and β can be absorbed into the scalar field via a redefinition, but that is not done in order to determine the origin of the different terms. The resulting field equations from the line element Eq. (2.3) admit a static, spherically symmetric, and asymptotically flat solution:

$$f(r) = 1 - \frac{\mu}{r} - \frac{\beta^2}{2\zeta\eta r^2}, \quad \text{and} \quad g(r) = \frac{1}{f(r)}. \tag{5.8}$$

This solution resembles a black hole in Braneworld gravity. [86]. The integration constant μ is equal to twice the black hole mass, i.e $\mu = 2M$. The parameters β and η must have the same sign, and the scalar field is provided by:

$$\tilde{\varphi}(r) = \pm 2\sqrt{\frac{\zeta}{\eta}}\left\{\arctan\left[\frac{\beta^2 + \zeta\eta\mu r}{\beta\sqrt{2\zeta\eta r(r-\mu) - \beta^2}}\right] - \arctan\left(\frac{\mu}{\beta}\sqrt{\frac{\zeta\eta}{2}}\right)\right\} \tag{5.9}$$

$$\text{if } \beta > 0 \text{ and } \eta > 0,$$

and

$$\tilde{\varphi}(r) = \pm 2\sqrt{\frac{\zeta}{-\eta}}\left\{\arctan\left[\frac{\beta^2 + \zeta\eta\mu r}{\beta^2 - \beta\sqrt{2\zeta\eta r(r-\mu)}}\right] + \arctan\left(\frac{\mu}{\beta}\sqrt{\frac{-\zeta\eta}{2}}\right)\right\}$$

$$\text{if } \beta < 0 \text{ and } \eta < 0. \tag{5.10}$$

As an initial point of coordinates, the geometry is singular. It is helpful to adapt a simplified notation with $\tilde{\gamma} = \beta^2/(2\zeta\eta)$. It is evident that if $\tilde{\gamma}$ is negative, this metric has a similarity to the Reissner-Nordstrom metric, with the squared charge given by $Q^2 = -\tilde{\gamma}$. The metric functions can be rewritten as follows:

$$f(r) = 1 - \frac{\mu}{r} - \frac{\tilde{\gamma}}{r^2}. \tag{5.11}$$

The radius of the event horizon is obtained as the largest root of the equation $f(x) = 0$, to give $x_h = (1 + \sqrt{1 + 4\tilde{\gamma}})/2$. Therefore, to avoid a naked singularity it is mandatory to have $\tilde{\gamma} \geq -1/4$, with $\tilde{\gamma} = -1/4$ in the case of an extremal black hole. Correspondingly,

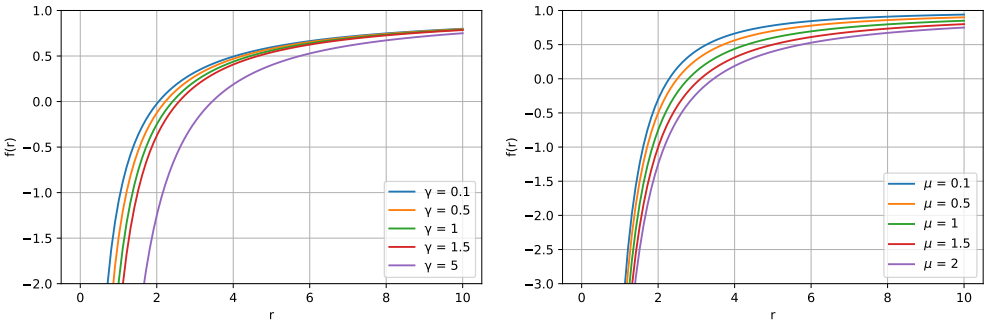

(a) Varying $\tilde{\gamma}$; $\mu = 2$ (b) Varying μ; $\tilde{\gamma} = 5$

Figure 5.1: The lapse function for a Horndeski black hole.

it is chosen to work within the interval $[-1/4, +\infty)$. Also, the lapse function of $f(r)$ for different $\tilde{\gamma}$, and μ are given in Fig. 5.1. It is observed that $\tilde{\gamma} \leq 1$ exhibits very minute variation that can be approximated to the same value, whereas, Figs. 5.1b exhibits a typical change for μ.

Null geodesics ($ds^2 = 0$) at the equatorial plane gives $\mathscr{K}$ for Horndeski black hole using the non-zero Christopher symbols as:

$$\mathscr{K} = -3\frac{\tilde{\gamma}}{r^4} + \left(-r^{-3} + \frac{3\tilde{\gamma}}{r^5}\right)\mu + \mathscr{O}(\mu^2, \tilde{\gamma}^2). \tag{5.12}$$

By plugging equation (5.12):

$$\hat{\alpha} = \frac{2\mu}{b} + \frac{3\pi\tilde{\gamma}}{4b^2} + \mathscr{O}(\mu^2, b^3). \tag{5.13}$$

Examining $\hat{\alpha}$ of Horndeski black holes, stable and unstable states, through the ramifications of $\tilde{\gamma}$ and μ against b in Fig. 5.2 with the overall trend in Fig. 5.3a:

1. Fig. 5.2a demonstrates the graphical influence of deflection angle against b with varying $\tilde{\gamma}$ and fixed μ. Negative $\tilde{\gamma}$ makes this metric comparable to the RN solution. Moreover, $\hat{\alpha}$ increases exponentially as $\tilde{\gamma}$ increases; $\tilde{\gamma}$ affects the deflection angle more for lower impact parameters

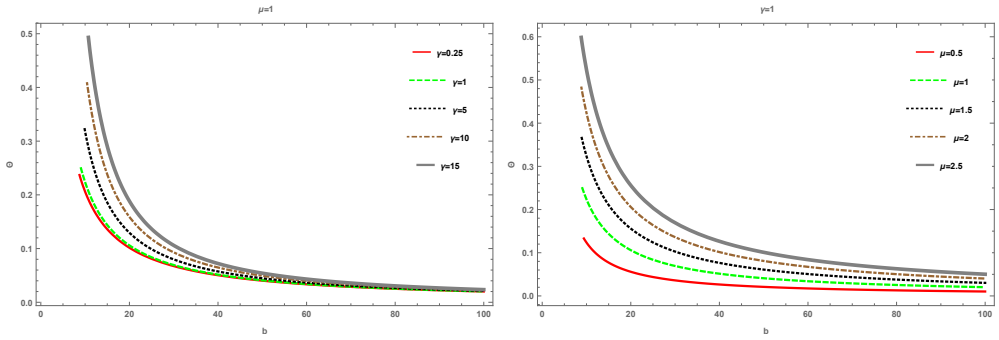

(a) Varying $\tilde{\gamma}$ (b) Varying μ

Figure 5.2: Closer look at the variation of the deflection angle.

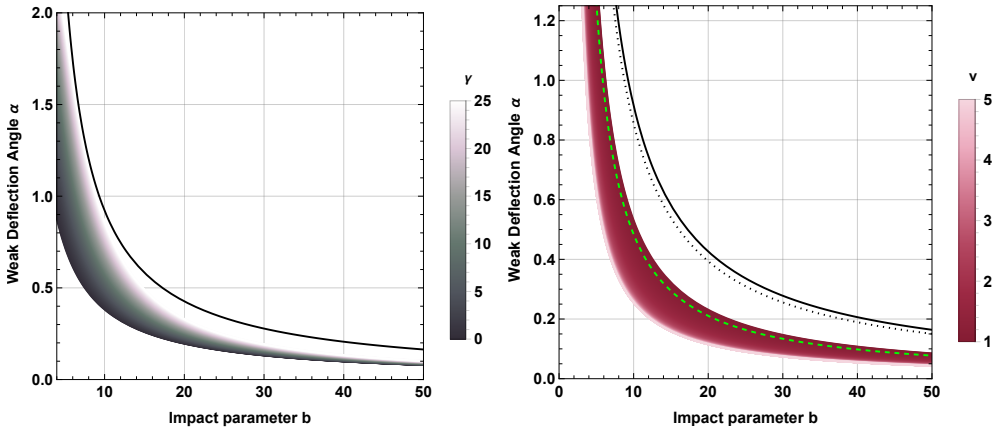

(a) Vacuum; varying γ (b) Massive particles; varying v

Figure 5.3: $\hat{\alpha}$ vs b for $\mu = 2$. The solid black line is the deflection angle for the Schwarzschild case with $M = 2$. On the right, the dotted black line shows a Schwarzschild black hole surrounded by massive particles; the dashed green line depicts the vacuum case of the Horndeski black hole.

2. Fig. 5.2b shows how increasing the mass term μ gradually increases $\hat{\alpha}$. Juxtaposing against Fig. 5.2a, the upshot of μ variation on $\hat{\alpha}$ is quite abrupt as it increases. While the μ term dominates, the repercussions of $\tilde{\gamma}$, though minute, cannot be ignored.

5.2 Massive Particles

The Gaussian curvature is:

$$\mathscr{K} = \frac{1}{2r^5}\left(\frac{14\tilde{\gamma}\mu}{v^6} - \frac{22\tilde{\gamma}\mu}{v^4} + \frac{8\tilde{\gamma}\mu}{v^2}\right) + \frac{1}{2r^4}\left(2\tilde{\gamma} - \frac{4\tilde{\gamma}}{v^4} + \frac{2\tilde{\gamma}}{v^2}\right) + \frac{1}{2r^3}\left(\mu - \frac{\mu}{v^4}\right), \tag{5.14}$$

to give:

$$\hat{\alpha} = \frac{\tilde{\gamma}\mu}{3b^3} - \frac{2\tilde{\gamma}\mu}{b^3v^4} + \frac{3\tilde{\gamma}\mu}{b^3v^2} + \frac{\pi\tilde{\gamma}}{4b^2} + \frac{\pi\tilde{\gamma}}{2b^2v^2} + \frac{\mu}{b} + \frac{\mu}{bv^2}. \tag{5.15}$$

Fig. 5.3b shows a large decrease in deflection for this, falling more for increasing v.

5.3 Plasma

The Horndeski black hole equation, when applied to the equivalent optical metric, designates the optical Gaussian curvature as:

$$\mathscr{K} = \left(-r^{-3} - 3/2\,\frac{{\omega_e}^2}{{\omega_\infty}^2 r^3}\right)\mu + \left(-3\,r^{-4} - 5\,\frac{{\omega_e}^2}{{\omega_\infty}^2 r^4} + \left(3\,r^{-5} + 13\,\frac{{\omega_e}^2}{{\omega_\infty}^2 r^5}\right)\mu\right)\tilde{\gamma}. \tag{5.16}$$

Hence, after simplification:

$$\hat{\alpha} \simeq \frac{2\mu}{b} + \frac{3\pi\tilde{\gamma}}{4b^2} + \frac{\pi\tilde{\gamma}\omega_e^2}{2b^2\omega_\infty^2} + \frac{\mu\,\omega_e^2}{b\omega_\infty^2} + \mathscr{O}(\mu^2, b^3). \tag{5.17}$$

The results show that photon rays are moving in a homogeneous plasma medium. The plasma effect can be eliminated by ignoring ω_e/ω_∞.

To investigate the graphical effect of deflection angle $\hat{\alpha}$ on Horndeski black holes, the physical impact of these graphs due to the effect of plasma terms ω_e/ω_∞, $\tilde{\gamma}$, and impact parameter b on deflection angle are reviewed. In a plasma medium, the deflection angle $\hat{\alpha}$ is investigated in relation to the impact parameter b. Fixing at $\mu = 2$, $\pi = 3.14$ and, for the sake of simplicity, $\omega_e/\omega_\infty = z$.

- Fig. 5.4 graphs $\hat{\alpha}$ vs b for varying z: as $z \to 1$, the influence on $\hat{\alpha}$ grows dramatically. $\hat{\alpha}$ in Fig. 5.4a is doubled when compared to Fig. 5.4b. It is clear that the deflection angle is quite sensitive to plasma, particularly at low b.
    1. Figure 5.4a interprets the significance of changing P, where the favorable action of $\hat{\alpha}$ is only examined for the range $0.1 \leq z \leq 0.9$. The weak deflection angle increases as the value of z (for plasma medium) increases.

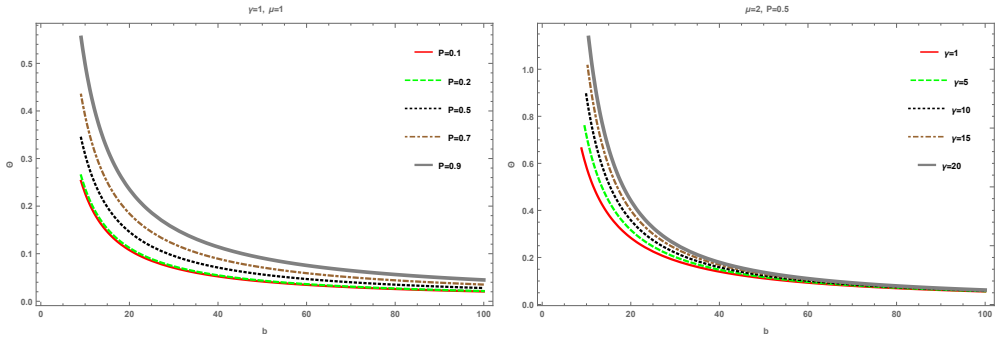

(a) Varying z (b) Varying $\tilde{\gamma}$

Figure 5.4: Closer look at the variation due to plasma.

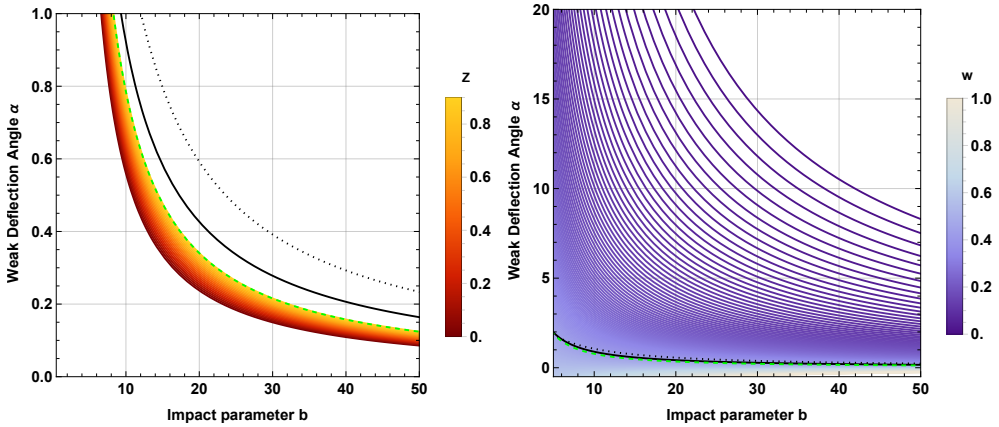

(a) Plasma case; varying z (b) Dark matter case; varying w

Figure 5.5: $\hat{\alpha}$ vs b in the presence of a medium. The solid black line is the Schwarzschild case with $M = 1$; the dotted black line shows the case of a Schwarzschild black hole surrounded by the same medium; the dashed green line depicts the vacuum case of a Horndeski black hole.

The zoomed-out view in Fig. 5.5a agrees with the above.

2. Figure 5.4b depicts an exponential increase in deflection angle with $\tilde{\gamma}$.

5.4 Dark Matter

Dark matter influences yield the deflection angle:

$$\hat{\alpha} = -\frac{3\pi B\tilde{\gamma}u}{2b^2} + \frac{9\pi B\tilde{\gamma}uvw^2}{2b^2} + \frac{3\pi\tilde{\gamma}}{4b^2} - \frac{3\pi\tilde{\gamma}vw^2}{2b^2} - \frac{4B\mu u}{b} + \frac{12B\mu uvw^2}{b} + \frac{2\mu}{b} - \frac{4\mu vw^2}{b}. \tag{5.18}$$

Yet again, the DM consequences are immense for low values of w with a few values falling under the Schwarzschild case as w approaches unity.

Chapter 6

REISSNER-NORDSTRÖM BLACK HOLE IN EINSTEIN-NONLINEAR-MAXWELL FIELDS WITH HIGHER-ORDER MAGNETIC CORRECTION

A conducting medium containing an electric charge can neutralize the magnetic charge, unlike normal matter. This is an interesting factor that influences the size of the shadow's radius as well according to [87]. The introduction of a magnetic charge leads to an augmentation in the curvature of spacetime, causing an increased attraction of photons towards the black hole. Consequently, this process results in a reduction in the radius of the shadow [88]. Magnetic charge, in combination with the spin of the black hole, gives rise to the formation of two separate horizons: the inner and outer horizons. These horizons are determined by the existence of stable and unstable photon orbits [89]. However, as per their experiments, the inner horizon becomes more prominent as the charge value approaches a critical value and the outer horizon remains charge-sensitive as the charge moves towards the centre. Previous research has demonstrated the impact of the magnetic charge on the shadow across different categories of black holes [9, 88].

The goal of this chapter is to discuss the Keeton-Petters formalism [90] parallel to the typical GW method [7] in the context of nonlinear electrodynamics (NLED). Furthermore, the black hole's shadow cast with a thin-accretion disk and a special case are investigated. [5] is the main reference for this chapter.

6.1 Corrected Reissner-Nordström Black Hole

From the Big Bang to the enigma of black holes, the existence of singularities has posed a challenge to the unification of general relativity with other cosmic models. Cosmologists have diligently endeavored to discover a solution for black holes devoid of singularities, with the pioneering work of Bardeen serving as a cornerstone in this pursuit [91]. By incorporating nonlinear electrodynamics into this solution, the researchers in [92] are aiming to eliminate singularity. They offered an analytical black hole solution in the weak field limit, comparable to Born-Infeld-type modifications to linear Maxwell's theory [93]. The equations governing a pure magnetic field are considered and following a series of computations and initiations involving the NLED Lagrangian, the energy-momentum tensor, and the Einstein tensor as the primary targets for a pure magnetic field, the black hole solution satisfying the Maxwell-nonlinear equations referred from [92] is found to be:

$$f(r) = 1 - \frac{2GM}{r} + \frac{Gp^2}{r^2} - \beta\frac{Gp^4}{60r^6} + \beta^2\frac{Gp^6}{810r^{10}} - \mathscr{O}\left(\beta^3\right), \tag{6.1}$$

where p is the magnetic charge defined as a magnetic monopole, *beta* is a dimensional constant with a dimension of [Length]^4, and M is the ADM[2] mass; it is directly related – with linear proportionality through the energy density – to the mass function $m(r)$ that holds the basis of the above solution such that $f(r) = 1 - 2Gm(r)/r$. This magnetic black hole solution will be the focus of this chapter and will henceforth be known as an ENM-corrected RN black hole.

The lapse functions of $f(r)$ for this black hole with $G = 1$ for different p, β, and M are given in Fig. 6.1. Though the overall behaviours of all three plots are similar, they

[2] ADM: Arnowitt-Deser-Misner, named after the Physicists who used the Hamiltonian formalism to find the total energy of an asymptotically-flat spacetime perceived by an observer at infinity in natural units ($c = 1$).

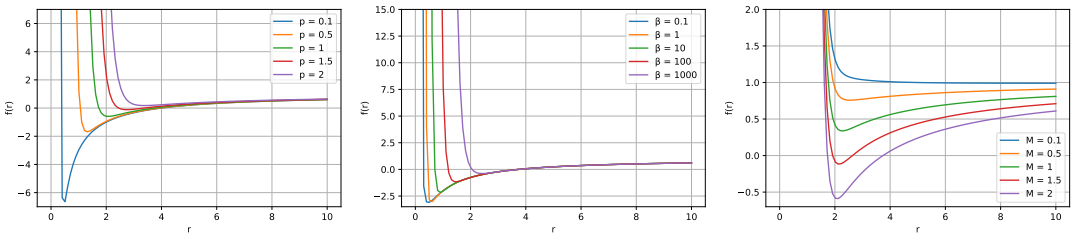

(a) Varying p; $M = 2$; $\beta = 500$ (b) Varying β; M=2; $p = 1$ (c) Varying M; $p = 1$; $\beta = 1$

Figure 6.1: The lapse function of the ENM corrected RN black hole.

behave differently for low values of r. For $p < 1$, a sharp dip is observed in Fig. 6.1a; a smoother dip is observed for $\beta < 100$ in Fig. 6.1b. The atypical behaviour of M is because of p and β. The influence of p on incoming light rays is depicted in Fig. 6.2.

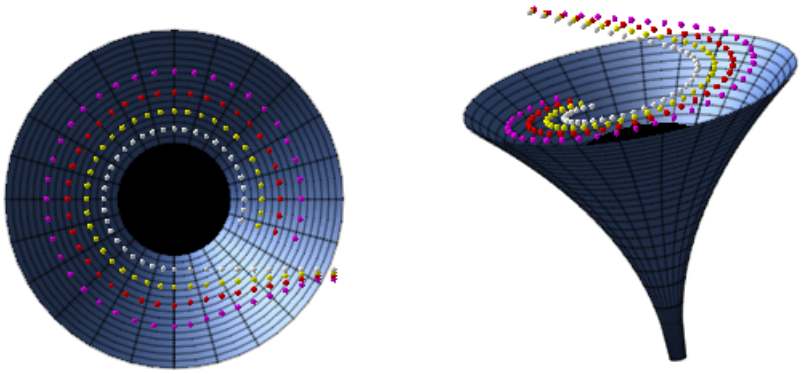

Figure 6.2: The representation of the function $f(r)$ in Cartesian coordinates. The first illustration presents a bird's-eye view, while the second one presents an angular perspective. The white circles symbolize the Schwarzschild scenario, whereas the yellow, red, and purple circles symbolize $p = 1.4$, $p = 1.45$, and $p = 1.5$, respectively.

Naturally:

$$\mathscr{K} \approx \frac{3G^2M^2}{r^4} + M\left(-\frac{6G^2p^2}{r^5} - \frac{2G}{r^3}\right) + \frac{p^4\left(40G^2r^2 - 7\beta G\right)}{20r^8} + \frac{3Gp^2}{r^4} + \mathscr{O}(p^6), \quad (6.2)$$

for which

$$\hat{\alpha} \approx \frac{4GM}{b} - \frac{3\pi Gp^2}{4b^2} + \frac{3\pi G^2M^2}{4b^2} + \frac{8G^3M^3}{3b^3} - \frac{8G^2Mp^2}{3b^3} + \frac{7\pi\beta Gp^4}{384b^6}. \quad (6.3)$$

This downsizes to the Schwarzschild case in the absence of the magnetic charge, $p = 0$.

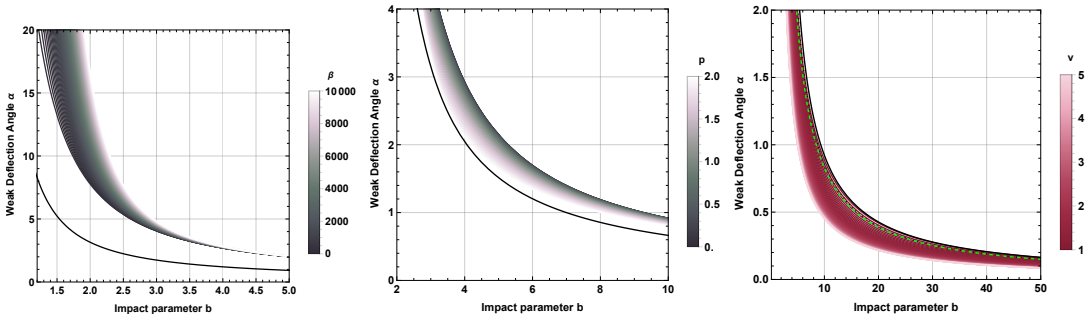

(a) Vacuum; varying β (b) Vacuum; varying p (c) Massive particle; varying v

Figure 6.3: $\hat{\alpha}$ vs b for $M = 1$. The solid black line is the deflection angle for a Schwarzschild case. On the right, the dotted black line shows a Schwarzschild black hole surrounded by massive particles; the dashed green line depicts the vacuum case of the ENM-corrected RN black hole.

Figs. 6.3a and 6.3b have been plotted to look at the consequences of β and p respectively. The scale of each parameter is interesting when compared: although small variations in β do not exhibit significant differences, it is observed that β tends to increase with increasing b. On the other hand, parameter p demonstrates a high sensitivity to any change, and it generally decreases as b increases. As a result, for a specific impact parameter, the deflection increases in proportion to the magnitude of the magnetic charge. These highlight the significance of the repercussions of β and p on the deflection angle, showcasing their inverse relationship. The consequence of magnetic charge on the curvature of an outgoing light ray is illustrated in Fig. 6.4.

6.1.1 Keeton-Petters Formalism

This general PPN (post-post-Newtonian) approach [8, 90] shows that Eq. (6.3) can be accurately obtained. Given the following metric:

$$\mathrm{d}s^2 = -A(r)\,\mathrm{d}t^2 + B(r)\,\mathrm{d}r^2 + r^2\,\mathrm{d}\Omega^2\,, \tag{6.4}$$

such that the coefficients are expressed in power series as:

$$A(r) = 1 + 2a_1\phi + 2a_2\phi^2 + 2a_3\phi^3 + \ldots\,, \tag{6.5}$$

$$B(r) = 1 - 2b_1\phi + 4b_2\phi^2 - 8b_3\phi^3 + \ldots\,, \tag{6.6}$$

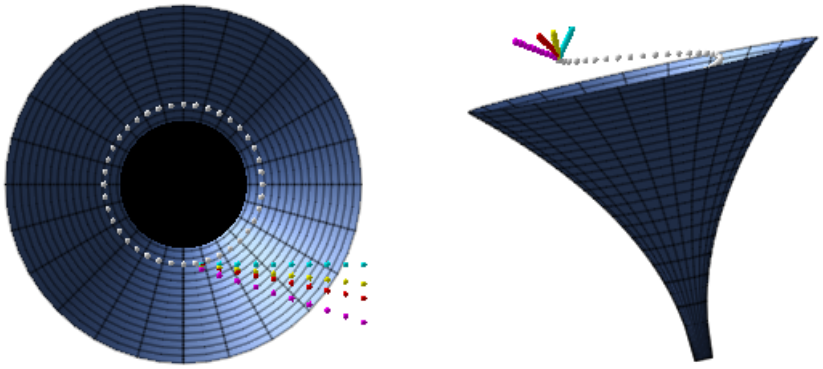

Figure 6.4: Ilustration of the function $f(r)$ deflecting a ray of light for varying p. The initial illustration presents a bird's-eye view, while the subsequent illustration presents an angular perspective. The white circles symbolize the Schwarzschild scenario, whereas the yellow, red, and purple circles symbolize $p = 1.4$, $p = 1.45$ and $p = 1.5$ respectively.

where the Newtonian potential is defined as $\phi \equiv -M/r$. Correlating this to the metric in the line element, $A(r) = 1/B(r) = f(r)$. Setting the theoretical quantity $P = pM$:

$$\begin{aligned} a_1 &= G \quad a_2 = GP^2/2 \quad (a_3 = 0), \\ b_1 &= G \quad b_2 = \left(4G^2 - GP^2\right)/4. \end{aligned} \tag{6.7}$$

The quantity $\hat{\varepsilon}$ as serial expansion expresses the corrected deflection angle in GR. By defining the source's gravity radius as $r_g \equiv M$, the bending of light in GR due to M can be expressed as $\hat{\varepsilon}_{GR} = 4\,r_g/b$. Therefore:

$$\hat{\varepsilon} = A_1 \left(\frac{r_g}{b}\right) + A_2 \left(\frac{r_g}{b}\right)^2 + \mathscr{O}\left(\frac{r_g}{b}\right)^3. \tag{6.8}$$

The coefficients A_1, A_2 are independent of M/b; in regard to $a_1, b_1, a_2,$ and b_2, they become $A_1 = 2\,(a_1 + b_1)$ and $A_2 = \pi\left(2a_1^2 - a_2 + a_1 b_1 - \frac{b_1^2}{4} + b_2\right)$ to give:

$$A_1 = 4G; A_2 = \pi\left[\frac{1}{4}\left(4G^2 - GP^2\right) + \frac{11G^2}{4} - \frac{GP^2}{2}\right], \tag{6.9}$$

as per Eq. (6.7). Ordering linearly, $\mathscr{O}(M^2/b^2)$ is ignored, rendering:

$$\hat{\varepsilon} = \frac{4GM}{b} - \frac{3\pi G p^2}{4b^2} \quad \Rightarrow \quad \hat{\varepsilon} = \hat{\alpha}_{GR}\left(1 - \frac{3\pi p^2}{16bM}\right), \tag{6.10}$$

in accord with Eq. (6.3) for $\mathscr{O}(M/b)$.

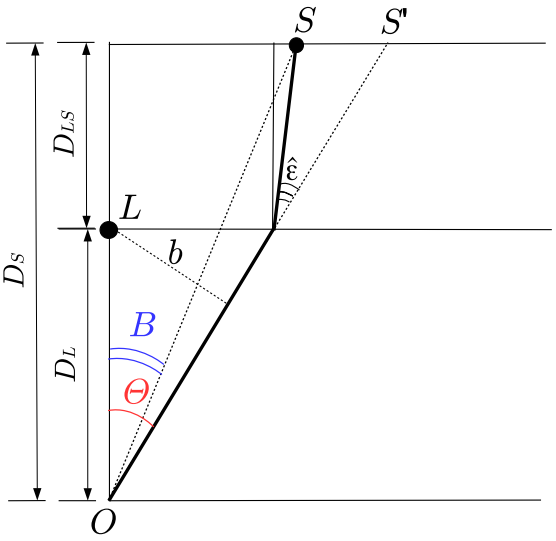

Figure 6.5: Lens Geometry [8].

The geometric arrangement of the lensing scenario is illustrated in Figure 6.5. The source is located at an angular position B, while the image appears at $\tilde{\Theta}$, and the deflection angle is denoted as $\hat{\varepsilon}$. The distances involved are denoted by D, and the subscripts S, L, and LS refer to observer-source, observer-lens, and lens-source, respectively. From the viewpoint of an observer at point O, the image of the source at point S appears as if it were at point S'. The coordinates of the lens are represented by L. In this analysis, the thin-lens approximation is employed, treating all light paths as straight lines. In terms of light propagation, b remains constant throughout the process. Figure 6.5 provides a clear visualization of the relationship $b = D_L \sin\tilde{\Theta}$. Because of this, the *lens equation* can be derived using basic geometric principles.

$$D_S \tan B = D_S \tan\tilde{\Theta} - D_{LS}\left[\tan\tilde{\Theta} - \tan\left(\tilde{\Theta} - \hat{\varepsilon}\right)\right]. \tag{6.11}$$

Utilizing this, the angular position $\tilde{\Theta}$ of the image can be determined as a function of B (the angular position of the source) and $\hat{\varepsilon}$. Several key assumptions underlie this calculation: the lens is assumed to be SSS, the source and observer are asymptotically flat, and light rays propagate outside the gravitational radius r_g, where r_0 represents the closest approach distance. Moreover, it is assumed that $r_0 \gg r_g$.

Under the assumption of small angles, Eq. (6.11) can be written as $D_S B = D_S \tilde{\Theta} - D_{LS} \hat{\varepsilon}$. Since $\hat{\varepsilon}_{GR} = 4M/b$ and $b = D_L \tilde{\Theta}$,

$$D_S B = D_S \tilde{\Theta} - \frac{D_{LS}}{D_L} \frac{4M}{\tilde{\Theta}}. \tag{6.12}$$

When $B = 0$, solving this equation reveals that the source, lens, and observer are perfectly aligned on a single line, resulting in the Einstein angle θ_E calculated as :

$$\theta_E = \sqrt{\frac{4MD_{LS}}{D_L D_S}}. \tag{6.13}$$

Subsequently, a characteristic length-scale called the Einstein radius is defined and is denoted as $R_E := D_L \theta_E$. In this context, all angular positions are normalized relative to the Einstein angle which serves as a reference. Now:

$$\zeta = \frac{B}{\theta_E},\ \theta = \frac{\tilde{\Theta}}{\theta_E},\ \text{(and setting)}\ \varepsilon = \frac{\tilde{\Theta}_M}{\theta_E}, \tag{6.14}$$

where $\tilde{\Theta}_M = \tan^{-1}(M/D_L)$ represents the angle subtended by the lens' gravitational radius. Employing ε, the observables can be subject to power series expansion. In the case of the image position, the lens equation derived from Eq. (6.11), and resembling $\hat{\varepsilon}$ as expressed in eq. (6.8), can be written as:

$$\theta = \theta_0 + \theta_1 \varepsilon + \mathscr{O}(\varepsilon^2), \tag{6.15}$$

where θ_0 is the position of the image in the weak-field limit resolved as

$$0 = -\beta + \theta_0 - \frac{1}{\theta_0}. \tag{6.16}$$

The image position, one of the observables, is subsequently obtained to be

$$\theta_0^{\pm} = \frac{1}{2}\left(\sqrt{4+\beta^2} \pm |\beta|\right), \tag{6.17}$$

where $\theta_0^{\pm}$ represents the parity images relative to the lens. The presence of a positive sign indicates that the image is situated on the same side as the source ($\beta > 0$), while a negative sign indicates that the image is positioned on the opposite side of the source ($\beta < 0$). In this scenario, the second-order term until $\mathscr{O}(\varepsilon)$ is found to be [90]:

$$\theta = \theta_0 + \frac{A_2\,\varepsilon}{A_1 + 4\theta_0^2} = \theta_0 + \frac{3\pi G\left(5GM^2 - p^2\right)\,\varepsilon}{16M^2\left(G + \theta_0^2\right)}, \tag{6.18}$$

For small angles, $\tilde{\Theta} \equiv \theta\,\theta_E$ is interpreted as the actual angular position, which, with the amelioration $\tilde{\Theta}_1 = \theta_1\,\theta_E\,\varepsilon$ becomes:

$$\tilde{\Theta}_1 \simeq \theta_1 \frac{M}{D_L} \simeq \frac{3\pi G\left(5GM^2 - p^2\right)}{16M^2}\frac{M}{D_L}. \tag{6.19}$$

Next is the observable that can provide the magnification of an image μ at $\tilde{\Theta}$ with the help of its sign formulated as:

$$\mu(\tilde{\Theta}) = \left[\frac{\sin B(\tilde{\Theta})}{\sin\tilde{\Theta}}\,\frac{\mathrm{d}B(\tilde{\Theta})}{\mathrm{d}\tilde{\Theta}}\right]^{-1}, \tag{6.20}$$

for the general case, the series expansion in ε gives

$$\mu = \mu_0 + \mu_1\varepsilon + \mathscr{O}(\varepsilon^2), \tag{6.21}$$

where,

$$\begin{aligned} \mu_0 &= \frac{16\theta_0^4}{16\theta_0^4 - A_1^2} \quad \Rightarrow \quad \mu_0 = \frac{\theta_0^4}{\theta_0^4 - G^2} \\ \mu_1 &= -\frac{16A_2\theta_0^3}{(A_1 + 4\theta_0^2)^3} \quad \Rightarrow \quad \mu_1 = -\frac{3\pi G\theta_0^3\left(5G - P^2\right)}{16\left(G + \theta_0^2\right)^3}. \end{aligned} \tag{6.22}$$

The positive parity image θ^+ is associated with $\mu > 0$, while the negative parity image θ^- is associated with $\mu < 0$. The magnification is influenced by the sign of P, where if $P^2 > 5G$, then $\mu_1 < 0$ and the positive-parity image appears faint, while the negative-parity image appears bright. This constraint can be utilized as an observational test for P. In this approximation, the total magnification is found to be negligible as it does not change to $\mathscr{O}(\varepsilon)$, with the second-order term having a proportionality with A_2^2.

The final observable is the time delay, which is defined as the difference in travel time (due to the lens) between the actual time that light takes and the time that it would take if there were no lens, and it is provided by:

$$\frac{\tau}{\tau_E} = \frac{1}{2}\left[a_1 + \beta^2 - \theta_0^2 - \frac{a_1+b_1}{2}\ln\left(\frac{D_L\,\theta_0^2\,\theta_E^2}{4D_{LS}}\right)\right] + \frac{\pi}{16\,\theta_0}\left(8a_1^2 - 4a_2 + 4a_1b_1 - b_1^2 + 4b_2\right)\varepsilon \;+\; \mathscr{O}(\varepsilon^2), \tag{6.23}$$

which becomes

$$\frac{\tau}{\tau_E} = \frac{1}{2}\left[4G + \beta^2 - \theta_0^2 - \frac{5G}{2}\ln\left(\frac{D_L\,\theta_0^2\,\theta_E^2}{4D_{LS}}\right)\right] + \frac{\pi}{16\,\theta_0}\left(15G^2 - 3\frac{Gp^2}{2M^2}\right)\varepsilon. \tag{6.24}$$

Physical units evince $\tau_E = 4GM/c^3$, while in natural units where G and c are set to unity, the time delay becomes $\tau_E = 4M$ for the considered system. The discrepancy in the time delay between the negative and positive parity images can be computed as:

$$\Delta\tau = \Delta\tau_0 + \Delta\tau_1\,\varepsilon + \mathscr{O}(\varepsilon^2), \tag{6.25}$$

where:

$$\begin{aligned}
\Rightarrow \Delta\tau_0 &= \tau_E\left[\frac{(\theta_0^-)^{-2} - (\theta_0^+)^{-2}}{2} - \frac{a_1+b_1}{2}\ln\left(\frac{\theta_0^-}{\theta_0^+}\right)\right] \\
&= \tau_E\left[\frac{(\theta_0^-)^{-2} - (\theta_0^+)^{-2}}{2} - G\ln\left(\frac{\theta_0^-}{\theta_0^+}\right)\right] \\
\Delta\tau_1 &= \tau_E\,\frac{\pi}{16}\left(8a_1^2 - 4a_2 + 4a_1b_1 - b_1^2 + 4b_2\right)\frac{(\theta_0^+ - \theta_0^-)}{\theta_0^+\theta_0^-} \\
&= \tau_E\,\frac{\pi}{16}\left(15G^2 - \frac{3Gp^2}{2M^2}\right)\left(\frac{\theta_0^+ - \theta_0^-}{\theta_0^+\theta_0^-}\right).
\end{aligned} \tag{6.26}$$

Applying corrections up to $\mathscr{O}(\varepsilon)$, it becomes:

$$\Delta\tau_1\varepsilon \simeq \frac{\tau_E}{16}\left(15G^2 - \frac{3Gp^2}{2M^2}\right)\pi\varepsilon. \tag{6.27}$$

6.2 Massive Particles

For the Jacobi metric defined for massive particles, the weak deflection angle of massive particles is documented as

$$\begin{aligned}
\hat{\alpha} = \frac{\pi\beta Gp^4}{384b^6} + \frac{\pi\beta Gp^4}{64b^6v^2} + \frac{16G^3M^3}{3b^3v^6} - \frac{40G^3M^3}{3b^3v^4} + \frac{10G^3M^3}{b^3v^2} + \frac{2G^3M^3}{3b^3} \\
+ \frac{4G^2Mp^2}{b^3v^4} - \frac{6G^2Mp^2}{b^3v^2} - \frac{2G^2Mp^2}{3b^3} - \frac{\pi G^2M^2}{b^2v^4} \\
+ \frac{3\pi G^2M^2}{2b^2v^2} + \frac{\pi G^2M^2}{4b^2} - \frac{\pi Gp^2}{2b^2v^2} - \frac{\pi Gp^2}{4b^2} + \frac{2GM}{bv^2} + \frac{2GM}{b}.
\end{aligned} \tag{6.28}$$

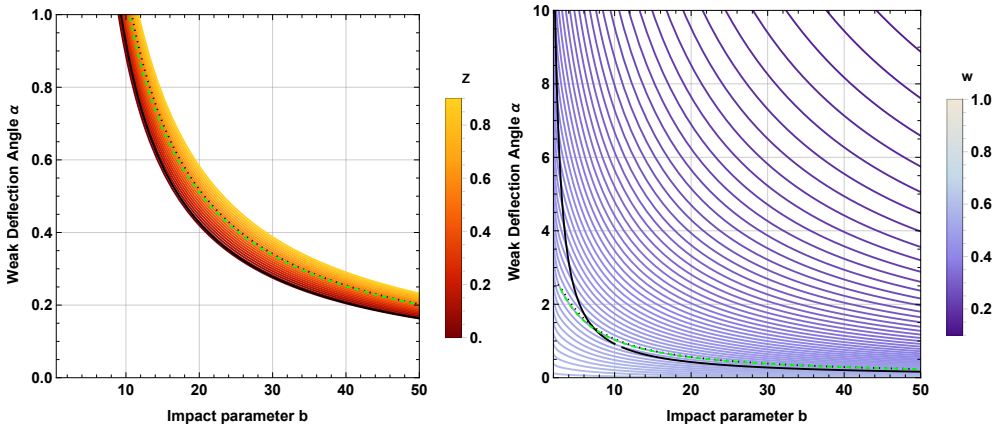

(a) Plasma case; varying z (b) Dark matter case; varying w

Figure 6.6: $\hat{\alpha}$ vs b in the presence of a medium for $M = 1$, $G = 1$, $p = 1$, and $\beta = 500$. The solid black line is the Schwarzschild case; the dotted black line shows a Schwarzschild black hole surrounded by the same medium; the dashed green line depicts the vacuum case of the ENM-corrected RN black hole.

In Fig. 6.3c, this deflection angle is plotted against b; v is observed to reduce the value of $\hat{\alpha}$, approaching the Schwarzschild case as $b/M \to \infty$.

6.3 Plasma

The deflection angle specified by the leading order terms is non-trivially:

$$\hat{\alpha} = \frac{\pi\beta G p^4 \omega_e^2}{64 b^6 \omega_\infty^2} + \frac{7\pi\beta G p^4}{384 b^6} - \frac{2G^3 M^3 \omega_e^2}{3b^3 \omega_\infty^2} + \frac{2G^2 M p^2 \omega_e^2}{b^3 \omega_\infty^2} - \frac{8G^2 M p^2}{3b^3} - \frac{\pi G^2 M^2 \omega_e^2}{2b^2 \omega_\infty^2} - \frac{\pi G p^2 \omega_e^2}{2b^2 \omega_\infty^2} + \frac{3\pi G^2 M^2}{4b^2} - \frac{3\pi G p^2}{4b^2} + \frac{2GM\omega_e^2}{b\omega_\infty^2} + \frac{4GM}{b}. \tag{6.29}$$

Fig. 6.6a is plotted to investigate the effects of plasma. Clearly, the presence of plasma leads to an increase in the deflection angle for a specific value of b. This outcome is not surprising since the bending is influenced by both gravitational effects and refraction, which introduces an additional and distinct component to the deflection.

6.4 Dark Matter

In the presence of dark matter, the deflection angle is prompted to be

$$\hat{\alpha} = -\frac{7\pi\beta BGp^4u}{192b^6} + \frac{7\pi\beta BGp^4uvw^2}{64b^6} + \frac{7\pi\beta Gp^4}{384b^6} - \frac{7\pi\beta Gp^4vw^2}{192b^6} + \frac{16BG^2Mp^2uvw^2}{b^3} - \frac{16BG^2Mp^2u}{3b^3} - \frac{16G^2Mp^2vw^2}{3b^3} + \frac{8G^2Mp^2}{3b^3} - \frac{9\pi BG^2M^2uvw^2}{2b^2} + \frac{3\pi BG^2M^2u}{2b^2} - \frac{9\pi BGp^2uvw^2}{2b^2} + \frac{3\pi BGp^2u}{2b^2} + \frac{3\pi G^2M^2vw^2}{2b^2} - \frac{3\pi G^2M^2}{4b^2} + \frac{3\pi Gp^2vw^2}{2b^2} - \frac{3\pi Gp^2}{4b^2} + \frac{24BGMuvw^2}{b} - \frac{8BGMu}{b} - \frac{8GMvw^2}{b} + \frac{4GM}{b}. \tag{6.30}$$

As a result, the dark matter medium can be seen to influence the deflection angle by causing small deflections compared to a Schwarzschild black hole. Fig. 6.6b graphs this variation. Its effect is more dispersed than in the other cases studied; dark matter is observed to have a significant impact on the deflection angle. Low values of the dark matter parameter w appear to produce a high deflection, whereas high values of w appear to produce a low deflection.

6.5 Shadow

The Hamilton-Jacobi approach for a photon is written as [94]:

$$H = \frac{1}{2}g^{\mu\nu}p_\mu p_\nu = \frac{1}{2}\left(\frac{L^2}{r^2} - \frac{E^2}{f(r)} + \frac{\dot{r}^2}{f(r)}\right) = 0. \tag{6.31}$$

Here, p_μ is the photon momentum, $p_\phi = L$ represents its angular momentum, $-p_t = E$ corresponds to its energy, and $\dot{r}$ is defined as the derivative of the Hamiltonian H with respect to p_r. This equation describes the dynamics of the system with an effective potential denoted as V.

$$V + \dot{r}^2 = 0, \quad V = f(r)\left(\frac{L^2}{r^2} - \frac{E^2}{f(r)}\right). \tag{6.32}$$

The circular null geodesics, as illustrated by Fig. 6.7, holds the stability condition $V(r) = V'(r) = 0$ and $V''(r) > 0$. For circular photon orbits, the instability is linked to the maximum value of the V as

$$V(r)|_{r=r_p} = 0, \quad V'(r)\big|_{r=r_p} = 0, \tag{6.33}$$

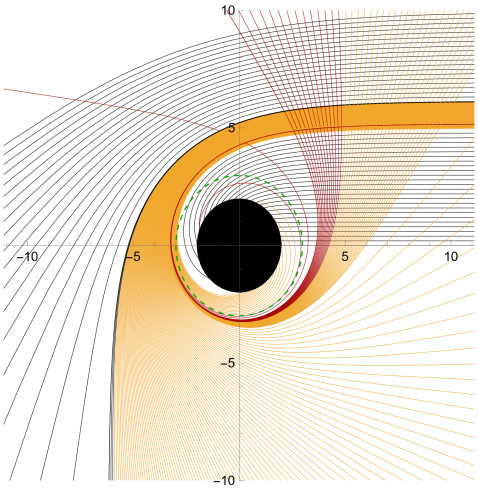

Figure 6.7: Raytracing of spacetime with null geodesics with respect to direct $\phi < 3\pi/2$ (black), lensing $3\pi/4 < \phi < 5\pi/4$ (yellow), and photon ring orbits $\phi > 5\pi/4$ (red); the central disk is the black hole.

where, the impact parameter $b \equiv L/E = r_p/\sqrt{f(r_p)}$ and $r_p = 3 + \frac{1}{2}\sqrt{36 - 8p^2}$ is the radius of the photon sphere: the latter can be computed from the largest root from:

$$\frac{f'(r_p)}{f(r_p)} = \frac{2}{r_p}. \tag{6.34}$$

This equation is solved numerically to ease the calculations of the photosphere radius r_p; the radius of the photon sphere increases with an increasing value of the confining charge parameter.

The black hole shadow radius with respect to a static observer at a position r_0 is [21]

$$R_s = r_p \sqrt{\frac{f(r_0)}{f(r_p)}}, \tag{6.35}$$

and for a distant observer ($f(r_0) = 1$), it is

$$R_s^2 = \frac{r_p^2}{f(r_p)}. \tag{6.36}$$

Accordingly,

$$R_s = \frac{\sqrt{2}\left(\sqrt{9 - 2p^2} + 3\right)}{\sqrt{\frac{p^2 + \sqrt{9-2p^2} - 3}{p^2}}}. \tag{6.37}$$

To gain more perspective in this context, Fig. 6.8 is plotted for various p values. The shadow radius and the magnetic charge are inversely proportional, indicating that the smaller the radius, the lesser the magnetic influence.

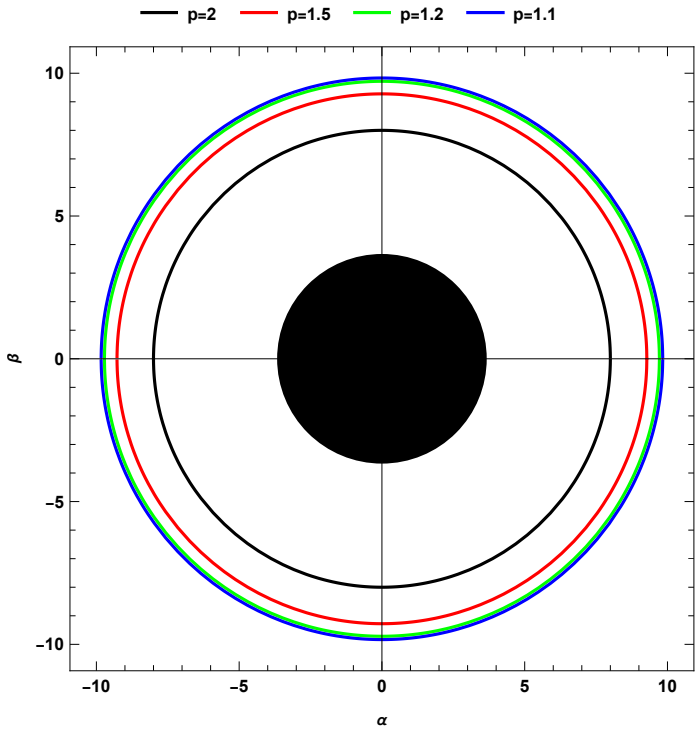

Figure 6.8: Shadow ($M = 2$ and $\beta = 0$) for varying p.

Fig. 6.9 presents the upper limits of p obtained from Event Horizon Telescope (EHT) observations, with a 68% confidence level (C.L.) upper limit of $p \leq 0.8$ and a 95% C.L. upper limit of $p \leq 0.92$ [9]. The solid black line in this numerical plot illustrates the variation of the black hole's shadow radius (R_{sh}/M) with respect to the parameter p for $\beta = 0.8$. It is interesting to note the exponential and inverse relationship exhibited by p, in addition to the observed range of variation in both parameters.

In a recent study, EHT confirmed that the spin of Sgr A* does not have any effect [95]. Consequently, the focus of research has been on non-rotating black holes. This

aligns with the reasoning presented in [9], where the authors investigate various gravity theories and fundamental physics, specifically considering the case where the spin parameter a is set to zero. They further demonstrate the validity of the aforementioned statement by visually illustrating that for small values of a and a rotating black hole, the shadow size is not significantly influenced, resulting in a distorted circle shape.

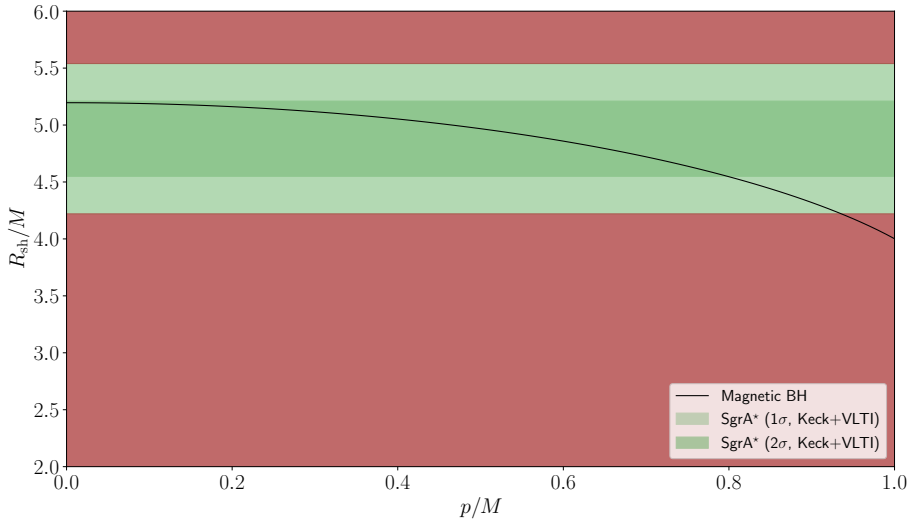

Figure 6.9: Constraints from EHT horizon-scale image of SgrA* at 1σ and 2σ [9] ($M = \beta = 1$).

6.5.1 Spherically in-falling Accretion

This section investigates spherically free-falling accretion using the technique of [96]. Unlike the static disc that was previously examined, the accretion disk is dynamic and spherical. The number of orbits formalism of [97] is utilized again for this dynamic model, but the crossings are distributed across the entire spherical accretion rather than at the equatorial plane. The integrated intensity observed at a specific frequency ν_{obs} expressed as an integral over the null geodesic γ to have the following form

$$I(\nu_{obs}, b_\gamma) = \int_\gamma g^3 j(\nu_e)\, \mathrm{d}l_{pr}, \tag{6.38}$$

where b_γ is the impact parameter's null geodesic, j is the emissivity per unit volume as a function of emitted frequency, and $\mathrm{d}l_{pr}$ is the infinitesimal (proper) length. and g

is the modified redshift factor

$$g = \frac{k_\mu u_o^\mu}{k_\mu u_e^\mu},\ k^\mu = \dot{x}_\mu, \tag{6.39}$$

with k^μ as the 4-velocity of the photon, u_o^μ as the 4-velocity of a static observer at infinity, and u_e^μ as the 4-velocity of the in-falling accretion such that

$$k_t = \frac{1}{b},\ k_r = \pm\frac{1}{bf(r)}\sqrt{1-f(r)\frac{b^2}{r^2}} \quad \text{and} \quad u_e^\mu = \left(\frac{1}{f(r)}, -\sqrt{1-f(r)}, 0, 0\right), \tag{6.40}$$

allowing

$$g = \left(u_e^t + \frac{k_r}{k_t}u_e^r\right)^{-1}. \tag{6.41}$$

Aside from proper time, the proper distance along γ can be represented by an affine parameter.

$$\mathrm{d}l_\gamma = k_\mu u_e^\mu\ \mathrm{d}\lambda = \frac{k^t}{g|k_r|}\ \mathrm{d}r. \tag{6.42}$$

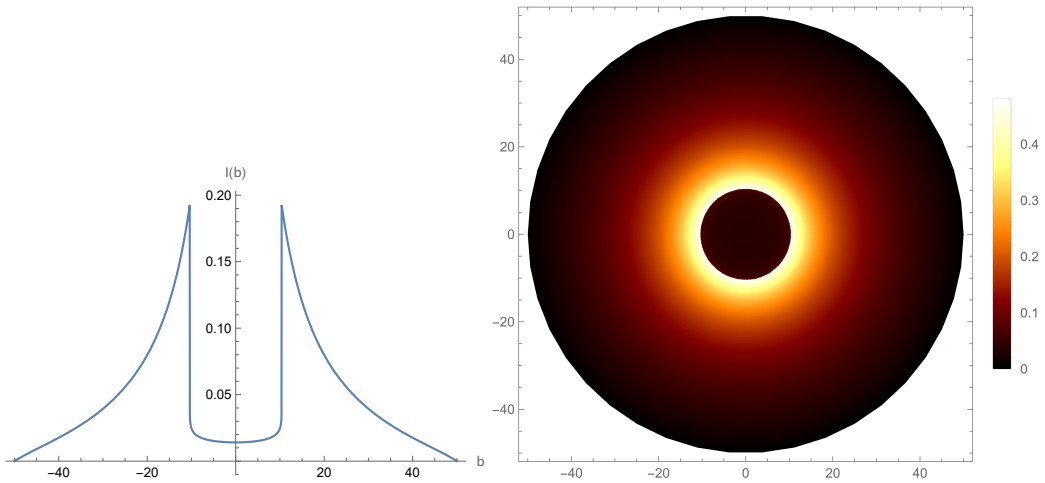

Figure 6.10: The visual manifestation of a spherically free-falling accretion emission in the vicinity of a charged black hole ($M = 2$, $p = 0.1$ and $\beta = 0$).

For the sake of simplicity, this model assumes a monochromatic emission with a rest-frame frequency ν_* and a radial profile $1/r^2$, such as

$$j(\nu_e) \propto \frac{\delta(\nu_e - \nu_*)}{r^2}, \tag{6.43}$$

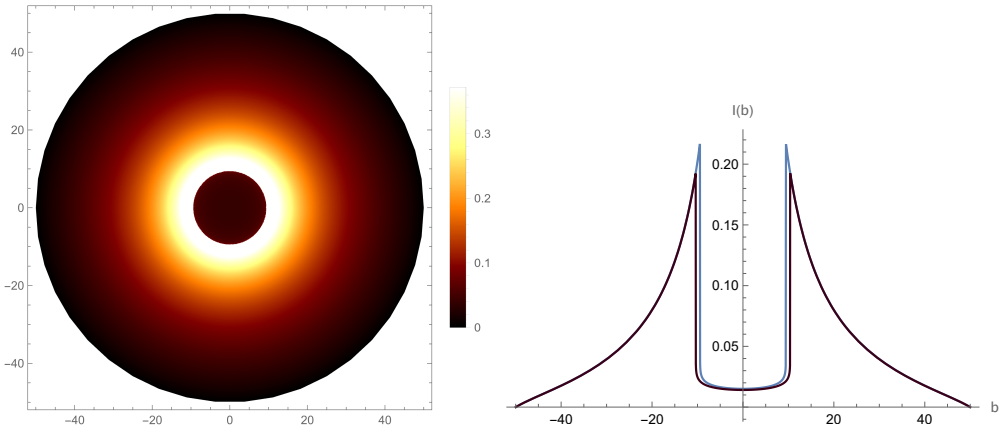

Figure 6.11: The visual manifestation of a spherically free-falling accretion emission in the vicinity of a charged black hole ($p = 0.99$, $\beta = 0$, and $M = 2$). The black and blue lines stand for $p = 0.1$ and $p = 0.99$ respectively.

where δ represents the delta function. Integrating eq. (6.38) across all frequencies yields the total observed flux, which is

$$F(b_\gamma) \propto \int_\gamma \frac{g^3}{r^2} \frac{k_e^t}{k_e^r} \, \mathrm{d}r. \tag{6.44}$$

Using EinsteinPy *Python* package [98] and Okyay- Övgün *Mathematica* package [31], (used also in [30, 32, 34]), the flux numerically integrated to examine the effects of the charge parameters. The EinsteinPy package is also used to plot geodesics, determine the critical impact parameter b_{cr} that separates the orbits of entering and exiting photons, and calculate the black hole's radius, its event horizon, and Ergosphere. See figures 6.10, and 6.11 for examples.

The shape of the black hole shadow is visually represented in Figs. 6.10 and 6.11 using stereographic projection in the celestial coordinates X and Y. It is evident from these plots that as the value of p increases, the radius of the shadow also increases. This observation highlights the significant impact of the magnetic charge on the size of the shadow. Consequently, the inclusion of a charge term leads to an apparent enlargement of the shadow while simultaneously reducing the intensity of incoming light.

Chapter 7

ASYMPTOTIC, MAGNETICALLY-CHARGED, NON-SINGULAR BLACK HOLE

When there is no existing singularity, a "regular" black hole, as pioneered by Bardeen, is an appealing prospect to pursue. Instead of singularity, these non-singular black holes are thought to have regular centers with a core of collapsed charged matter. [91]. The resulting Einstein tensor is not only appropriate for a physical domain, but it also meets the conditions for a static, spherically symmetric, and asymptotically flat metric. Locally, a non-singular spacetime is defined for a black hole that forms from a vacuum region and evaporates to a vacuum region, with its quiescence explained as a static region. [99].

The existence of a shadow [26] has allowed distant observers to see a black hole despite its invisibility. The size and shape of a shadow are found to be dependent on the geometry of spacetime rather than the characteristics of the accretion in relativistic models. [29]. The black hole's extreme gravitational pull causes light rays to be deflected toward the singularity, causing those that skim the photon sphere to begin looping around it. When a photon lands precisely on the photon sphere, it will forever wrap around the black hole. This phenomenon occurs for light rays passing in the vicinity of the unstable photon region and increases the intensity of the original source through the extended path length of the light rays, thus increasing its brightness around the shadow's edge; consequently, the brightness of the cloud just

outside the shadow appears to be enhanced as well. In this chapter, the black hole will be scrutinized in terms of the deflection angle as in [6].

7.1 AMCNS Black Hole

Extensive research has been conducted on the solutions that depict black holes within the framework of non-linear electrodynamics in the context of general relativity [100]. To describe the solution for a magnetically charged black hole, consider the non-linear electrodynamics where the Lagrangian density is written in the exponential form as:

$$\pounds = -P\exp(-\beta P), \tag{7.1}$$

where, $P \equiv \frac{1}{4}\left(F_{\mu\nu}F^{\mu\nu}\right) = \frac{1}{2}\left(B^2 - E^2\right)$, and $F^{\mu\nu} = \partial^{\mu}A^{\nu} - \partial^{\nu}A^{\mu}$. $F^{\mu\nu}$ is the electromagnetic field tensor, B is the magnetic field, E is the electric field, A^{μ} is the four-potential, and β is a parameter with the dimensions of [Length]^4 having an upper bound of $\left(\beta \leq 1\times 10^{-23}\mathrm{T}^{-2}\right)$ The Euler-Lagrange equation is formulated as:

$$\partial_{\mu}\left(\frac{\partial \pounds}{\partial\left(\partial_{\mu}A_{\nu}\right)}\right) - \frac{\partial \pounds}{\partial A_{\nu}} = 0, \tag{7.2}$$

where $\mu,\ \nu \in [0,3]$. Thus, the field equations come to be:

$$\partial_{\mu}\left[(\beta P - 1)\exp\left(-\beta P\right)F^{\mu\nu}\right] = 0. \tag{7.3}$$

The energy-momentum tensor takes the form of:

$$\tau^{\mu\upsilon} = H^{\mu\lambda}F^{\upsilon}_{\lambda} - g^{\mu\upsilon}\pounds, \tag{7.4}$$

where, $g^{\mu\upsilon} = 1/g_{\mu\upsilon}$ and:

$$H^{\mu\lambda} \equiv \frac{\partial \pounds}{\partial F_{\mu\lambda}} = -\left(1-\beta P\right)\exp\left(-\beta P\right)F^{\mu\lambda}. \tag{7.5}$$

Thus, the energy-momentum tensor derived from the Lagrangian density is:

$$\tau^{\mu\upsilon} = \exp\left(-\beta P\right)\left[(\beta P - 1)F^{\mu\lambda}F^{\upsilon}_{\lambda} + g^{\mu\upsilon}P\right], \tag{7.6}$$

whose trace is:

$$\tau = 4\beta P^2\exp\left(-\beta P\right). \tag{7.7}$$

The instance of $\beta \to 0$ not only signifies weak limits, but also reverts to classical electrodynamics as $\pounds \to -P$ and $\tau = 0$ in Eq. (7.7).

Typically, when β is not zero and the energy-momentum tensor has a non-zero trace, it entails that the scale invariance is violated. That's why, if any forms of nonlinear electrodynamics incorporate a dimensional parameter, they would also break the scale invariance, prompting the dilation current to be non-trivial: $\partial_\upsilon x^\mu \tau^\upsilon_\mu = \tau$

This can be overruled by the general principles of causality together with unitarity according to which the group velocity of the background perturbations is less than c. The sustaining of the causality principle necessitates that $\pounds_P = \partial\pounds/\partial P \leq 0 \Rightarrow \beta P \leq 1$. For a purely magnetic field, $B \leq \sqrt{\frac{2}{\beta}}$ ought to be fulfilled. Besides, the constraint $\pounds_P + 2P\pounds_{PP} \leq 0$ allows the unitarity principle to hold provided $\pounds_{PP} \geq 0$. While Eq. (7.1) construes $\beta P \leq 0.219$ agreeing with , it is clear that the limitations for both the causality and unitarity principles incur for $\beta P \leq 0.219$ giving:

$$B \leq \sqrt{\frac{5-\sqrt{17}}{2\beta}} \simeq \frac{0.66}{\sqrt{\beta}}. \tag{7.8}$$

Deriving the metric of a static AMCNS black hole in a spherically symmetric spacetime starts from the governing equations for a pure magnetic field as follows: The invariant P is deliberated in terms of an electric charge q to be:

$$P = \frac{q^2}{2r^4}. \tag{7.9}$$

Computing the function $f(r)$ specific to the AMCNS black hole is necessary to go on. To pursue this, putting:

$$f = 1 - \frac{2mr^2}{r^3 + 2ml^2}, \tag{7.10}$$

engenders the Hayward metric [99] of a non-singular black hole that is static, has no

charge, and emerges as the solution of a certain modified gravity theory. The quantity l is an approximate parameter in the length-scale under which the corollaries of the cosmological constant prevail.

If M is assumed to vary with r, then:

$$M(r) = \int_0^r \rho(r) r^2 \, \mathrm{d}r = m - \int_r^\infty \rho(r) r^2 \, \mathrm{d}r, \tag{7.11}$$

where $m = \int_0^\infty \rho(r) r^2 \, \mathrm{d}r$ describes the magnetic mass of the black hole that is responsible for screening the magnetic interactions so that the perturbative divergences of magnetostatics can be eliminated.

The energy density, in the absence of an electric field, ensues from Eq. (7.6) to be:

$$\rho = \frac{q^2}{2r^4} \exp\left(\frac{-\beta q^2}{2r^4}\right). \tag{7.12}$$

This transforms the mass function to:

$$M(r) = \frac{q^2}{2} \int_0^r \exp\left(\frac{-\beta q^2}{2r^4}\right) \frac{\mathrm{d}r}{r^2} = \frac{q^{3/2} \Gamma\left(\frac{1}{4}, \frac{\beta q^2}{2r^4}\right)}{2^{11/4} \beta^{1/4}}, \tag{7.13}$$

where, the incomplete gamma function is characterized by:

$$\Gamma(s,x) = \int_x^\infty t^{s-1} e^{-t} \, \mathrm{d}t. \tag{7.14}$$

Therefore, rewriting the magnetic mass as:

$$m = M(\infty) = \frac{q^{\frac{3}{2}} \Gamma\left(\frac{1}{4}\right)}{2^{\frac{11}{4}} \beta^{\frac{1}{4}}} \simeq \frac{0.54 q^{\frac{3}{2}}}{\beta^{\frac{1}{4}}}. \tag{7.15}$$

Consolidating all of the above, the metric function is discovered to be [101]:

$$f(r) = 1 - \frac{r^2 q^{\frac{3}{2}} \Gamma\left(\frac{1}{4}, \frac{\beta q^2}{2r^4}\right) 2^{\frac{-7}{4}} \beta^{\frac{-1}{4}}}{r^3 + l^2 q^{\frac{3}{2}} 2^{\frac{-7}{4}} \beta^{\frac{-1}{4}} \Gamma\left(\frac{1}{4}, \frac{\beta q^2}{2r^4}\right)}. \tag{7.16}$$

The metric function in the circumstance of $l = 0$ reduces to Reissner-Nordström solution [100]. In the vicinity of radial infinity, its asymptotic value is attained using

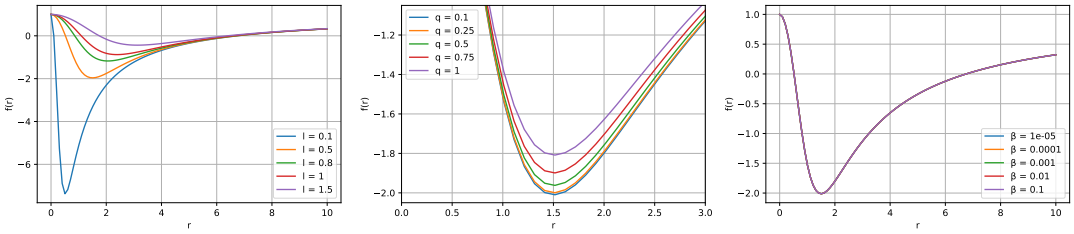

(a) Varying l; q=0.5; $\beta = 10^{-5}$ (b) Varying q; l=0.5; $\beta = 10^{-5}$ (c) Varying β; l=0.5; q=0.5

Figure 7.1: The lapse function of the AMCNS black hole.

the expansion of the series:

$$\Gamma(s,z) = \Gamma(s) - z^s \left[\frac{1}{s} - \frac{z}{s+1} + \frac{z^2}{2(s+2)} + O\left(z^3\right) \right], \quad z \to 0. \tag{7.17}$$

Ultimately, the metric function $f(r)$ at $r \to \infty$ is structured as [101]:

$$f(r) = 1 - \frac{r^2 \left[2m - \frac{q^2}{r} + \frac{\beta q^4}{20r^5} + O(r^{-9}) \right]}{r^3 + l^2 \left[2m - \frac{q^2}{r} + \frac{\beta q^4}{20r^5} + O(r^{-9}) \right]}. \tag{7.18}$$

This will be used for the subsequent computations of the AMCNS black hole. The lapse function of $f(r)$ for this black hole for different p, β, and M are given in Fig. 7.1. Low values l are seen to imply excessive variation. The effect of q is small but significant. However, β seems to have a trivial effect over a broad range of values.

The photon behaviors within the AMCHS black hole for a range of l values are illustrated in Figure 7.2. Subsequently, Figure 7.3 presents the paths followed by light rays as they orbit around the AMCNS black hole using the method defined in [97].

In light of this, the geodesics of the optical metric that controls the AMCNS black hole is explored in greater detail in Fig. 7.2. The fate of the light ray is determined by the tiniest variation in its trajectory as it approaches the black hole from infinity; this is a predictable effect of the electric charge, which will either strongly draw the ray in or divert it around. In addition, it is seen that an increase in l causes the light to retract toward the black hole's centre more rapidly. By extrapolating from this, it is seen that

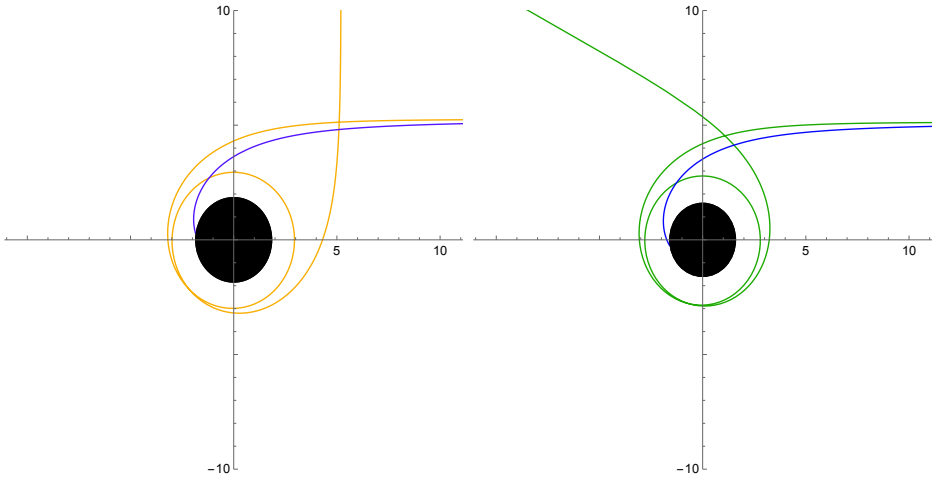

Figure 7.2: Geodesics of AMCNS black hole for $q = 0.5$, $\beta = 0.001$, and varying l; $l = 0.5$ (left), and $l = 0.7$ (right).

Fig. 7.3 captures the raytracing of the AMCNS metric. The multitude of light rays in this figure makes the abrupt coiling more noticeable.

The Gaussian curvature is computed from the non-zero Christoffel symbols due to its proportionality to the Ricci scalar and is found to be:

$$\begin{aligned}\mathscr{K} = m\Bigg(&\frac{q^4\left(225\beta+19\beta r^2-1830r^2-22950\right)}{10r^{11}}-\frac{6q^2\left(r^2+25\right)}{r^7}-\frac{2}{r^3}\Bigg)\\&+l^2\left[m^2\left(\frac{30q^2}{r^8}-\frac{3q^4\left(23\beta+65r^2-3640\right)}{10r^{12}}\right)-\frac{21mq^4}{r^9}\right]\\&+m^2\Bigg(-\frac{3q^4\left(1326\beta-130r^4+124\beta r^2-18410r^2-202800\right)}{10r^{14}}\\&+\frac{6q^2\left(50r^2+612\right)}{r^{10}}+\frac{3r^2+100}{r^6}\Bigg)+\frac{q^4\left(-21\beta+40r^2+1050\right)}{20r^8}+\frac{3q^2}{r^4}.\end{aligned} \tag{7.19}$$

Owing to the complexity of this calculation, the Gaussian curvature was reduced to $\mathscr{O}\left(m^2\right)$ and the integral was simplified by ignoring the higher-order terms $\mathscr{O}\left(q^5\right)$. With $\mathrm{d}S \approx (r+3m)\,\mathrm{d}r\,\mathrm{d}\phi$, the deflection angle due to weak lensing for an asymptotic, magnetically charged, non-singular black hole is estimated by employing the straight-line approximation to be:

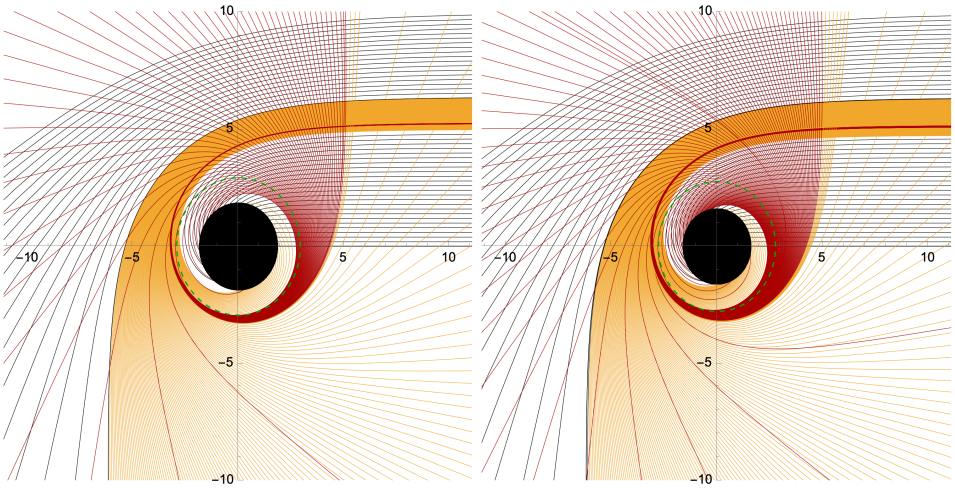

Figure 7.3: Raytracing of AMCNS black hole for $q = 0.5$, $\beta = 0.001$, and varying l; $l = 0.5$ (left), and $l = 0.7$ (right). The lines coloured in black, gold, and red represent the direct, lensed, and photon rings correspondingly. On the panel located to the right, a chosen assortment of related trajectories in Euclidean polar coordinates, denoted as (r, ϕ), is depicted. The black hole is symbolized by a black disk, and the circular orbit of light is a dashed yellow circle.

$$\begin{aligned}\hat{\alpha} = &-\frac{1.43139l^2q^5}{b^6\sqrt{\beta}} + \frac{7.15694q^5}{b^6\sqrt{\beta}} + \frac{7\pi\beta q^4}{128b^6} - \frac{175\pi q^4}{64b^6} - \frac{10.0777q^{9/2}}{b^5\beta^{3/4}} \\ &+ \frac{17.28q^{7/2}}{b^5\sqrt[4]{\beta}} - \frac{0.6912q^{11/2}}{b^5\sqrt[4]{\beta}} + \frac{1.5459q^5}{b^4\sqrt{\beta}} - \frac{3\pi q^4}{16b^4} - \frac{8.58833q^3}{b^4\sqrt{\beta}} \\ &- \frac{0.629856q^{9/2}}{b^3\beta^{3/4}} - \frac{0.72q^{7/2}}{b^3\sqrt[4]{\beta}} + \frac{0.687066q^3}{b^2\sqrt{\beta}} - \frac{3\pi q^2}{4b^2} + \frac{2.16q^{3/2}}{b\sqrt[4]{\beta}},\end{aligned} \tag{7.20}$$

in the weak-field limit. Note that the mass function defined by Eq. (7.15) is employed here in the place of m. From this result, the deflection angle is expected to change significantly because of the parameters that govern the black hole, reducing it to the case of a Schwarzschild black hole when $\beta = 0$, $q = 0$, and $l = 0$. This relation is depicted in Figs. 7.4a and 7.4b.

Taking a look at this equation graphically, the deflection angle is seen to be vividly affected by l and more intensely for q. The ranges of values for l and q are chosen according to the acquirable potentialities of a charged particle in the black hole locale. The deviating curve shows that the deflection angle is more than the Schwarzschild

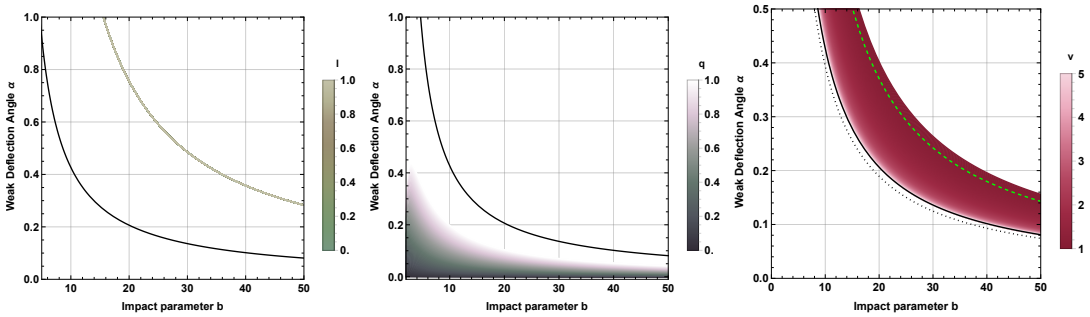

(a) Vacuum; varying l (b) Vacuum; varying q (c) Dark matter case; varying v

Figure 7.4: $\hat{\alpha}$ vs b in the presence of a medium for $\beta = 10^{-5}$. The solid black line is the Schwarzschild case; the dotted black line shows a Schwarzschild black hole surrounded by the same medium; the dashed green line depicts the AMCNS black hole.

case when there is an electric charge, and it keeps increasing as q increases. The deceiving large contribution from l is seemingly increasing the deflection angle.

As a result, it appears that the charge q is increasing the deflection angle. This implies that the distortions will be more pronounced, stronger, and possibly contain more details about the properties of the structure of the black hole and the light source.

7.2 Massive Particles

The deflection angle is calculated to be:

$$\hat{\alpha} = \frac{0.229022q^3}{b^2\sqrt{\beta}} - \frac{0.916088q^3}{b^2\sqrt{\beta}v^4} + \frac{1.37413q^3}{b^2\sqrt{\beta}v^2} - \frac{\pi q^2}{2b^2v^2} - \frac{\pi q^2}{4b^2} + \frac{1.08q^{3/2}}{b\sqrt[4]{\beta}} + \frac{1.08q^{3/2}}{b\sqrt[4]{\beta}v^2}. \tag{7.21}$$

In contrast to the other cases, the presence of massive particles is enhancing the deflection throughout the range of $0 \leq w \leq 1$, perhaps, due to their positive interaction with the black hole parameters (in the descending order) l, q, and β.

7.3 Plasma

An AMCNS black hole surrounded by plasma gives the deflection angle:

$$\hat{\alpha} = -\frac{0.458044q^3\omega_e^2}{b^2\sqrt{\beta}\omega_\infty^2} - \frac{\pi q^2\omega_e^2}{2b^2\omega_\infty^2} + \frac{0.687066q^3}{b^2\sqrt{\beta}} - \frac{3\pi q^2}{4b^2} + \frac{1.08q^{3/2}\omega_e^2}{b\sqrt[4]{\beta}\omega_\infty^2} + \frac{2.16q^{3/2}}{b\sqrt[4]{\beta}}. \tag{7.22}$$

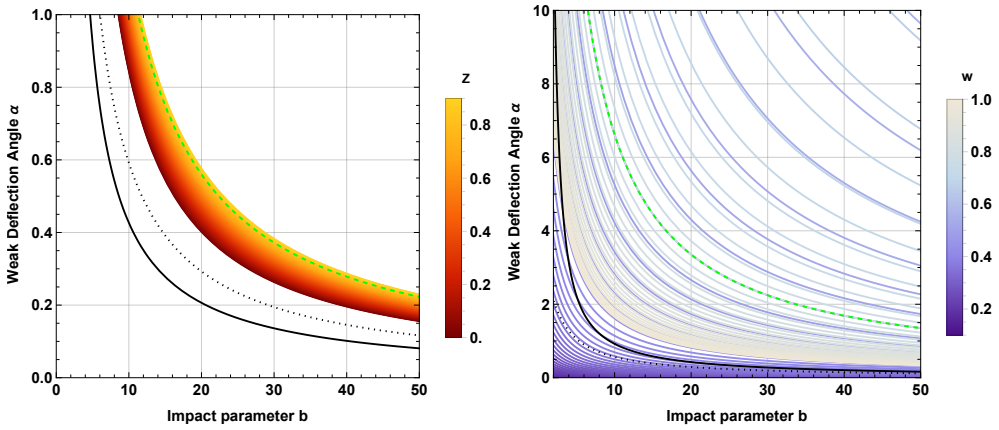

(a) Plasma case; varying z (b) Dark matter case; varying w

Figure 7.5: $\hat{\alpha}$ vs b in the presence of a medium for $q = l = 0.5$ and $\beta = 10^{-5}$. The solid black line is the Schwarzschild case with $M = 1$; the dotted black line shows the case of a Schwarzschild black hole surrounded by the same medium; the dashed green line depicts the vacuum case of the asymptotically flat black hole.

As always, plasma increases the deflection with increasing z; the offset of $z = 0$ from the Schwarzschild case is relative;y higher for this black hole, thanks to l, q and β.

7.4 Dark Matter

The weak deflection angle of an asymptotic, magnetically charged, non-singular black hole enveloped by dark matter can be expressed as:

$$\hat{\alpha} = \frac{1}{(Bu+vw^2+1)^2}\left[-\frac{1.43139l^2q^5}{b^6\sqrt{\beta}} - \frac{14.3139q^5}{b^6\sqrt{\beta}} + \frac{7\pi\beta q^4}{128b^6} - \frac{175\pi q^4}{64b^6} + \frac{17.28q^{7/2}}{b^5\sqrt[4]{\beta}} - \frac{3\pi q^4}{16b^4} - \frac{8.58833q^3}{b^4\sqrt{\beta}} + \frac{1.44q^{7/2}}{b^3\sqrt[4]{\beta}} - \frac{0.687066q^3}{b^2\sqrt{\beta}} - \frac{3\pi q^2}{4b^2} + \frac{2.16q^{3/2}}{b\sqrt[4]{\beta}}\right]. \tag{7.23}$$

In Fig. 7.5b, it is demonstrated that the deflection angle exhibits an upward trend as the parameter w increases within the weak field limits, implying more dark matter activity engenders more distortions in the lensing profile. While it is not possible to predict how dark matter behaves around a black hole as opposed to the well-understood outer-galactic distribution, its fundamentality of augmenting the distortions, and by extension, the deflection angle, is unchanging.

7.5 Accretion Disk And The Shadow Cast

This section examines at the shadow cast by a black hole with a thin accretion disk. The structure that results from a central gravitating object's gravitational pull on nearby material, such as gas or dust, is known as an accretion disk. [96, 97, 102]. This matter gains kinetic energy as it approaches the central object and creates a rapidly rotating disk around it. The disk may emit radiation in various forms, such as X-rays, visible light, or radio waves, depending on its temperature and density. Since they facilitate the transfer of mass and angular momentum easier, accretion disks play a crucial role in the growth and development of gravitating objects.

When the lensing effect and the accretion disk work together, a shadow of a black hole appears. In essence, the phenomenon of gravitational lensing is the key factor that distinguishes the black hole shadow in the Newtonian case in contrast to that of the general-relativistic case, thus, magnifying the shadow with the bending of light. The critical curve separating the capture orbits and the scattering orbits creates the shadow with a geometrically thick, optically thin region filled with emitters (that either spiral into the black hole or veer away from it) and is associated with a distant, homogeneous, isotropic emission ring. When discussing an emission region, the former property is crucial because the intensity dips at the same time as the shadow, making it visible through this distinct visual signature. The black hole's inherent parameters primarily determine the size of the shadow, and the orbital instability of the light rays from the photon sphere causes the shadow's shape to change. The shadow appears to a distant observer as a dim, two-dimensional disk that is illuminated by its uniformly bright surroundings.

For the line element given by Eq. (7.18), introducing the function $h(r)$ such that:

$$h^2(r) = \frac{r^2}{A(r)}, \tag{7.24}$$

which is equivalent to the effective potential for photon motion [94]. Not that according to line element in 7.18, $A(r) = \frac{1}{B(r)} = f(r)$. Eq. (7.25) can be rearranged and rewritten as:

$$\left(\frac{\mathrm{d}r}{\mathrm{d}\phi}\right)^2 = \frac{r^4}{B(r)}\left(\frac{1}{b^2A(r)} - \frac{1}{r^2}\right) = \frac{r^2}{B(r)}\left(\frac{r^2}{b^2A(r)} - 1\right), \tag{7.25}$$

where, the impact parameter $b \equiv L/E$ yet again. This equation is analogous to the traditional energy-conservation law described for one-dimensional motion in classical mechanics:

$$\left(\frac{\mathrm{d}r}{\mathrm{d}\phi}\right)^2 + V(r) = 0, \tag{7.26}$$

with ϕ taking the place of the temporal variable and the effective potential $V(r)$ displaying its dependence on r, and by extension, b. This is also known as the orbit equation.

To determine the circular trajectories, the equations $V = 0$ and $\frac{\mathrm{d}V}{\mathrm{d}r} = 0$ can be solved. For a light ray approaching the centre, if there exists a point at which it turns back around to exit the orbit after the ray reaches the minimum radius R, then the condition $\frac{\mathrm{d}r}{\mathrm{d}\phi}|_R = 0$ needs to be complied with, yielding the orbit equation to be:

$$\frac{1}{b^2} = \frac{A(R)}{R^2}. \tag{7.27}$$

This relation between the constant of motion and R instigates the following relationship:

$$b = h(R), \tag{7.28}$$

which in turn yields:

$$\left(\frac{\mathrm{d}r}{\mathrm{d}\phi}\right)^2 = \frac{r^2}{B(r)}\left(\frac{h^2(r)}{h^2(R)} - 1\right), \tag{7.29}$$

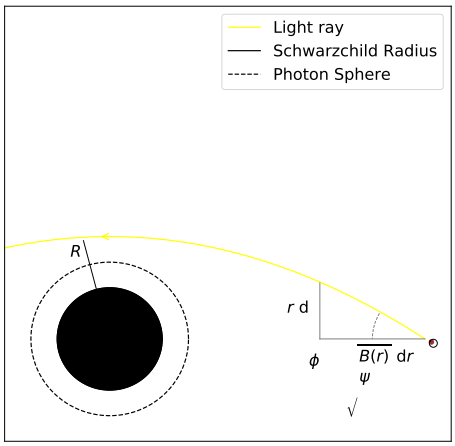

Figure 7.6: Description of the turning point with the minimum radius R and the shadow's angular radius ψ in the Schwarzschild spacetime when a light ray is sent to the past by an observer located at r_o in the present.

Say, a static observer located at a radial coordinate r_o shoots one light ray to the past. The dimensionless quantity ψ is identified in terms of the cotangent to be:

$$\cot\psi = \sqrt{\frac{g_{rr}}{g_{\phi\phi}}}\frac{\mathrm{d}r}{\mathrm{d}\phi}\bigg|_{r=r_O} = \frac{\sqrt{B(r)}}{r}\frac{\mathrm{d}r}{\mathrm{d}\phi}\bigg|_{r=r_O}, \tag{7.30}$$

as represented by Fig. 7.6 to be the measurable angle between the light ray and the radial coordinate which is directed towards the point of closest approach. It is termed as the angular radius of the shadow.

Squaring this equation and substituting Eqs. (7.28) and (7.29) in it gives:

$$\cot^2\psi = \frac{h^2 r_o)}{h^2(R)} - 1 \qquad \text{i.e.,} \qquad \sin^2\psi = \frac{h^2(R)}{h^2\left(r_o\right)}. \tag{7.31}$$

Here, the light ray approaching the circular (with radius r_{ph}), unstable photon orbits asymptotically is oriented to the past, and so is the shadow's boundary curve. In the limit where where $R \to r_{ph}$, the above expression can be rewritten as:

$$\sin^2\psi_{sh} = \frac{h^2\left(r_{ph}\right)}{h^2\left(r_o\right)} \qquad \text{and} \qquad b_{cr} = h\left(r_{ph}\right). \tag{7.32}$$

This implies:

$$\sin^2 \psi_{sh} = \frac{b_{cr}^2}{h^2(r_o)} = \frac{b_{\rm cr}^2}{r_o^2/A(r_o)}. \tag{7.33}$$

In the pursuit of calculating r_{ph} for the metric in Eq. (7.18) next, it is essential to realize that both $\mathrm{d}r/\mathrm{d}\phi$ and $\mathrm{d}^2r/\mathrm{d}\phi^2$ should simultaneously be zero. Differentiating Eq. (7.25), all terms vanish following the conditions except the third term acquired from the parentheses which are equated to zero resulting in:

$$0 = \frac{\mathrm{d}}{\mathrm{d}r} h^2(r). \tag{7.34}$$

The range of values that r can take is extensive inferring that there could be multiple photon orbits – stable and unstable, existing together, with the light rays oscillating and spiraling respectively – impinging on the construction of the black hole shadow. For $r = r_{ph}$, the shadow can be determined for any distance, small or large, in a SSS, asymptotically-flat spacetime for $h(r)$ from Eq. (7.32) by:

$$b_{cr} = \frac{r_{ph}}{\sqrt{A\left(r_{ph}\right)}} \qquad \text{and} \qquad R_{sh} = \psi_{sh} \approx \frac{b_{cr}}{r_o}\sqrt{A(r_o)}. \tag{7.35}$$

In the numerical plot depicted in Fig. 7.7, the radius of the black hole's shadow (R_{sh}) is calculated for different values of l for the asymptotically flat case $A(r_o = 1)$, and $(r_0 = 1)$. It is intriguing to observe the exponential and inverse relationship exhibited by l, irrespective of the range within which the parameters vary. In Fig. 7.7, the upper limits of l are presented based on EHT observations. According to the 68% confidence level (C.L.) [9], the upper limit for l is 0.6.

7.5.1 Spherically in-falling Accretion

In this section, the model of spherically free-falling accretion around AMCNS black hole from an infinite distance is investigated as in § 6.5.1. To analyze the shadow created by the thin accretion disk around the AMCNS black hole, the starting point is to numerically solve the aforementioned equation. The integration of the flux reveals

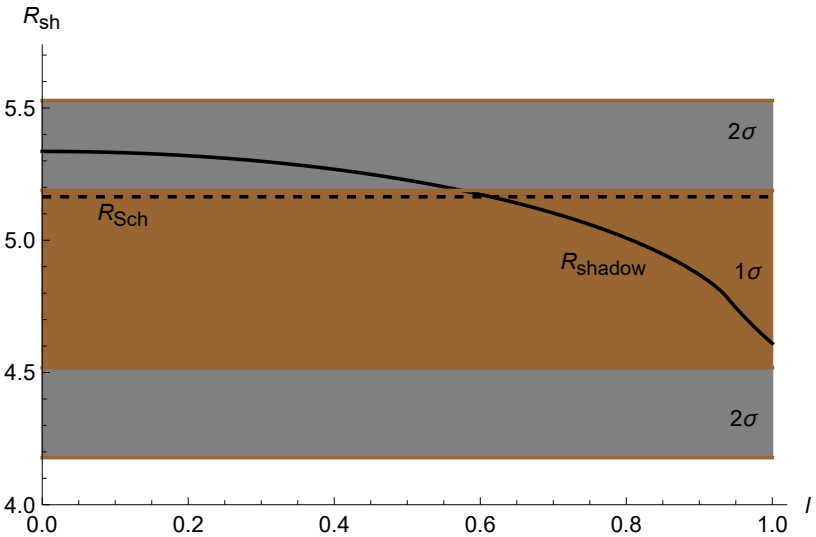

Figure 7.7: Constraints from the Event Horizon Telescope horizon-scale image of Sagıttarius A* at 1σ [9]($q = 0.5$, $\beta = 0.001$, and varying l).

the impact of the parameter l on the specific intensity observed by a distant observer for an in-falling accretion. The results are presented in Figs. 7.8, 7.9, and 7.10.

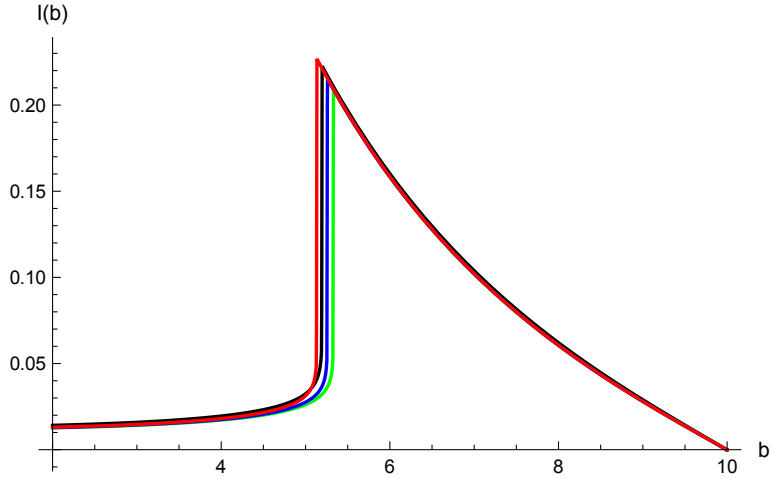

Figure 7.8: $q = 0.5$; $\beta = 0.001$; $l = 0.3$ (blue), $l = 0.5$ (green), and $l = 0.7$ (red).

The figures in Fig. 7.9, and 7.10 show the intensity plots and stereographic projections of the AMCNS black hole described following the method of [96,97,102]. The smooth transition between the layers in the journey away from the event horizon is depicted by the intensity plot. In Fig. 7.10 sharpness in each photon band illustrates the impact of

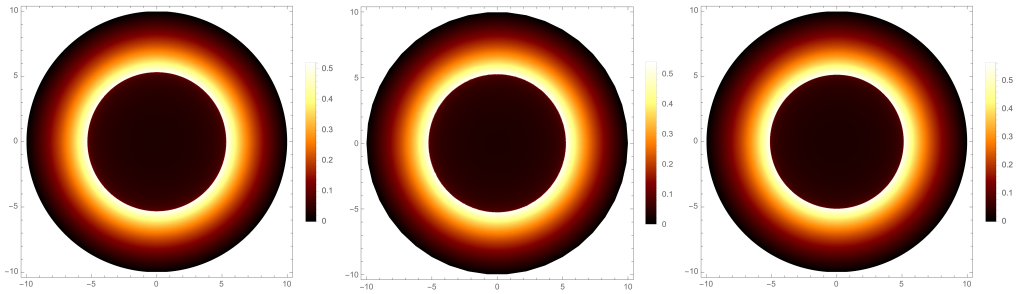

Figure 7.9: $q = 0.5$, $\beta = 0.001$, and $l = 0.3$ (left), $l = 0.5$ (middle), and $l = 0.7$ (right).

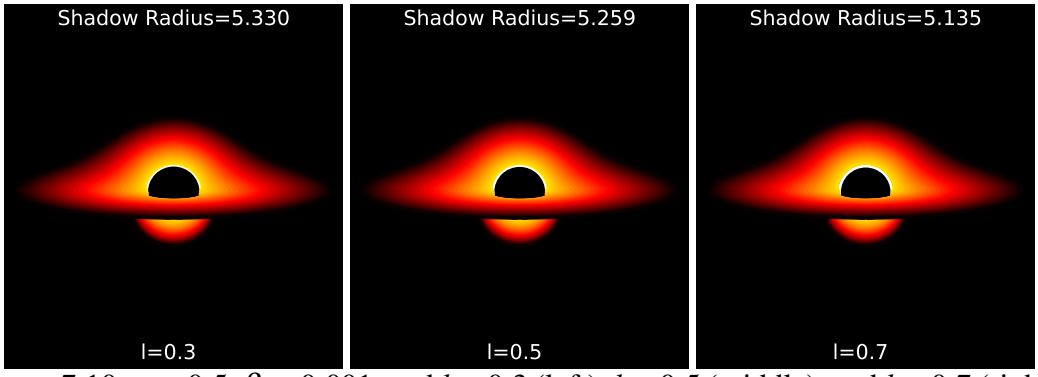

Figure 7.10: $q = 0.5$, $\beta = 0.001$, and $l = 0.3$ (left), $l = 0.5$ (middle), and $l = 0.7$ (right).

the parameters q, l, and β that appear to be brighter.

It's difficult to ignore the differences in how the shadow sizes appear between the three images in Fig. 7.9. As l increases, it is observed that the emissivity from the innermost photon orbit becomes brighter. As a result, it appears that the size of the dark shadow region is shrinking. Fig. 7.8 illustrates the small but non-trivial size of this difference numerically. The shadow outline in Fig. 7.10 clearly illustrates how the appearance of additional photon inner-orbits that are proportionally increasing with l causes the peak intensity to increase.

The crucial feature that makes a striking difference between them when compared to the shadow of a Schwarzschild black hole is the singularity. The Schwarzschild black hole has a singularity, or a point of infinite density and zero volume, at its centre.

The event horizon, a mathematical construct that presumes the black hole is a point singularity, is the one that is significantly impacted among all the characteristics of a black hole that are disturbed by this (such as curvature, geometry, density profile, etc.). For a non-singular black hole, this presumption does not hold; in that case, the event horizon becomes an apparent boundary beyond which light cannot travel to infinity, but can still escape to some finite distance. This leads the non-singular black hole to have a smaller event horizon than the Schwarzschild black hole, which in turn explains why the former has a smaller shadow.

In conclusion, any object that avoids a black hole and creates a time-dependent shadow will inevitably cause distortions of varying sizes depending on its characteristics. Additionally, a black hole's singularity at the center may cause the geometry of spacetime to curve more, resulting in a wider event horizon and a larger shadow. A non-singular black hole, on the other hand, would have smoother geometry and a smaller horizon, which would lead to a smaller shadow size. Additionally, due to dispersion, dark matter increases the degree of distortions.

Chapter 8

CONCLUSION

In this research, the deflection angle using the Gauss-Bonnet theorem has been studied. The solution given by Gibbons and Werner was adapted and applied to various scenarios pertaining to the Schwarzschild black hole so as to lay out the blueprint for this work. The lapse function of the black hole was analysed, and the deflection angle was formulated for vacuum and then for the case when the black is surrounded by massive particles. The effects of triggering media were subsequently examined, namely, plasma and dark matter. All these results were plotted in order to be examined graphically. Comparing and contrasting various sources helped recognize a pattern. It was discovered that each adjunct played a particular and distinctive role in altering the deflection angle in all of the cases investigated.

The quantum gravity outcomes in the close vicinity of a black hole were probed with the goal to retain the specific state of an object slipping into it, consequently resolving the information paradox. The presence of a medium introduces significant alterations to the deflection angle, attributable to quantum effects. This phenomenon has been extensively investigated in the context of supermassive black holes, such as Sagittarius A* and M87. [71, 73]. The EUP corrections were found to be high enough to estimate various parameters on a large scale. Finally, the three important observables were identified: position, magnification, and time delay.

Then, a thorough analysis of the deflection angle of light by an exponentially flat

black hole was performed in the context of Horndeski theory in weak field approximation. The Horndeski theory's optical geometry of asymptotically flat black holes was employed to analyze the deflection angle. Decreasing the impact parameter increased the deflection angle, decreasing the mass term μ decreased the deflection angle, and increasing the curvature constant was seen to decrease the deflection angle gradually. The Horndeski theory and its mathematical implications yield significant conclusions regarding various observables, including angular positions, separation, magnification, and fluxes. A case study focusing on astrophysical applications for Sagittarius A* and M87 provides further insights into these findings [84]. This was followed by analyzing the deflection angle of photons by Horndeski black holes in weak field limits. The term $\tilde{\gamma}$ was found to increase the weak deflection angle. When $\mu = 2M$ for the first-order of b, the Schwarzschild black hole is recovered. Furthermore, in the case of $\gamma = -Q^2$, the result is the deflection angle for the Reissner-Nordstrom black hole. The charge corrects the second-order term to a small extent, resulting in a smaller weak deflection angle than in the Schwarzschild case, which agrees with [103].

After that, an RN black hole under the influence of a magnetic charge for various conditions was investigated. The impact of higher-order magnetic correction in Einstein-nonlinear-Maxwell fields was scrutinized. The derived vacuum deflection angle was validated with the Keeton-Petters formalism, which we extended to determine three observables. Additionally, the shadow and spherically in-falling accretion were examined.

Finally, the astrophysics of an asymptotic, magnetically charged, non-singular black hole was scrutinized, starting with the Euler-Lagrange equation for nonlinear

electrodynamics and applying it to the Hayward metric via the energy-momentum tensor trace. The discovery of its relationship to the energy density aided in determining the mass function and, with additional calculations, the metric function of the AMCNS black hole. For the AMCNS black hole, even a small change in the refractive index resulted in a massive upshot in the bending angle. Moreover, the AMCNS case was researched using the black hole shadow. The critical curve and the angular radius of the shadow were determined by employing the Euler-Lagrange equation once more. They were thoroughly examined using stereo-graphic projections; the singularity at the centre of the Schwarzschild black hole curves and distorts its spacetime geometry more than a non-singular black hole, resulting in a larger horizon and shadow size. The AMCNS black hole has a smaller horizon and shadow size due to its smoother spacetime geometry.

Professional methodologies of maximum parametric inclusiveness help refine our understanding of gravitational lensing. The weak deflection angle is computed with the goal of delving deeper into the black hole's gravitational field, intrinsic properties such as mass, spin, and so on, the nature of light bending, and, ultimately, the validity of Einstein's theory. These bestow a better understanding of black hole dynamics and prepare Observational Astrophysicists for what to expect. Overall, the bending angle was calculated for various black holes with distinct properties in a vacuum at the weak-field limits. Then the deflection angle of massive particles using the Jacobi metric was evaluated, followed by the presence of the plasma and dark matter mediawere. Massive particles mostly exhibited an inverse proportionality suggesting that more massive particles mean lesser deflection. Plasma was discovered to be directly proportional to the electron frequency to photon frequency ratio, implying that more refraction resulted in more bending. The deflection, on the other hand,

decreased as dark matter activity increased. The capacity of all the $\hat{\alpha}$ equations to conform between vacuum and supplementary influences fosters flexibility in altering the result for an array of evaluations.

8.1 Future Goals

The effects of gravitational lensing on the deflection angle resulting from the bending of trajectories of massive objects have been extensively studied based on various criteria [74]. These investigations highlight the subtle nature of infinitesimal modifications. In the weak field regime, as discussed by [104], deviations between modified gravity and general relativity are typically too small to be detectable, except for the differential time delay, which exhibits a more noticeable increase. The ivestigation of C.-Y. Wang et al. [105] explores weak lensing observables for charged Horndeski black holes, specifically focusing on Sagittarius A* as the lens. The findings suggest that the deviations of these observables from those of the Schwarzschild black hole are either too minuscule to be detected or can be easily overshadowed by Sagittarius A* flares. Despite the angular separation, angular difference, and flux difference between the two lensed images falling within the thresholds of current technology, the results imply that the current technology is insufficient to validate these conclusions. Similarly, [106] investigates weak lensing by a regular non-minimal Einstein-Yang-Mills black hole and reports that its effects are equivalent to those caused by a Reissner-Nordström black hole. Nonetheless, all prior research agrees on one point: current technology is not adequate to validate the obtained corollaries.

The distortions produced by each black hole's weak deflection reveal lots of information about the source of the light rays as well as the black hole. This variation can be used to improve the accuracy of differential deflection derived from weak

lensing presumptions. This fact motivates me to develop new hypotheses that could polish and perfect our perception: my future work is geared toward this goal. I intend to collect as many contributing factors that affect our understanding of black hole theories as possible and improve them, no matter how complex they are, so that both theoretical and observational astrophysics can use them as a resource for enhancement. I hope to find ways to reduce our assumptions, such as zero spin, staticity, spherical symmetry, and many other constraints, and deal with the black hole as realistically as possible. Furthermore, I aspire to explore the captivating process of accretion jets in the context of relativistic hydrodynamics. This will not only help me to take advantage of my studies on gravitational lensing and modified gravity theories but also open new prospects in the field of gravitational waves [107]. Learning how to minimize initial presumptive constraints has dared me to solve the bigger challenges posed by Physics.

Alas, in the words of Albert Einstein, "Everything should be made as simple as possible, but not simpler!"

REFERENCES

[1] Y. Kumaran and A. Övgün, "Weak deflection angle of extended uncertainty principle black holes," *Chin. Phys. C*, vol. 44, no. 2, p. 025101, 2020.

[2] W. Javed, J. Abbas, Y. Kumaran, and A. Övgün, "Weak deflection angle by asymptotically flat black holes in Horndeski theory using Gauss-Bonnet theorem," *Int. J. Geom. Meth. Mod. Phys.*, vol. 18, no. 01, p. 2150003, 2021.

[3] Y. Kumaran and A. Övgün, "Deriving weak deflection angle by black holes or wormholes using Gauss-Bonnet theorem," *Turk. J. Phys.*, vol. 45, no. 5, pp. 247–267, 2021.

[4] A. Övgün, Y. Kumaran, W. Javed, and J. Abbas, "Effect of horndeski theory on weak deflection angle using the gauss-bonnet theorem," *Int. J. Geom. Meth. Mod. Phys.*, vol. 19, no. 12, p. 2250192, 2022.

[5] Y. Kumaran and A. Övgün, "Deflection Angle and Shadow of the Reissner–Nordström Black Hole with Higher-Order Magnetic Correction in Einstein-Nonlinear-Maxwell Fields," *Symmetry*, vol. 14, no. 10, p. 2054, 2022. [Online]. Available: https://www.mdpi.com

[6] Y. Kumaran and A. Övgün, "Shadow and deflection angle of asymptotic, magnetically-charged, non-singular black hole," arXiv:2306.04705 2023.

[7] G. W. Gibbons and M. C. Werner, "Applications of the gauss-bonnet theorem to gravitational lensing," *Class. Quant. Grav.*, vol. 25, p. 235009, 2008.

[8] M. L. Ruggiero, "Light bending in $f(T)$ gravity," *Int. J. Mod. Phys. D*, vol. 25, no. 06, p. 1650073, 2016.

[9] S. Vagnozzi, R. Roy, Y.-D. Tsai, and L. Visinelli, "Horizon-scale tests of gravity theories and fundamental physics from the Event Horizon Telescope image of Sagittarius A*," *Classical and Quantum Gravity*, 5 2022.

[10] M. Bartelmann and P. Schneider, "Weak gravitational lensing," *Phys. Rept.*, vol. 340, p. 291, 2001.

[11] R. H. Sanders and S. S. McGaugh, "Modified newtonian dynamics as an alternative to dark matter," *Ann. Rev. Astron. Astrophys.*, vol. 40, p. 263, 2002.

[12] B. Abbott, et al. [LIGO Scientific, and V. Collaborations], "Physical review letters," *Phys. Rev. Lett.*, vol. 119, no. 16, p. 161101, 2017.

[13] A. Einstein, "The Foundation of the General Theory of Relativity," *Annalen Phys.*, vol. 49, no. 7, pp. 769–822, 1916.

[14] C. Montgomery, W. Orchiston, and I. Whittingham, "Michell, Laplace and the origin of the black hole concept," *Journal of Astronomical History and Heritage*, vol. 12, no. 2, pp. 90–96, Jul. 2009.

[15] P. de Laplace, *Exposition du systeme du monde. Seconde edition revue et augmentee*. Crapelet, 1799. [Online]. Available: https://books.google.com.cy/books?id=4GJUAAAAcAAJ

[16] K. Schwarzschild, "On the gravitational field of a mass point according to Einstein's theory," *Sitzungsber. Preuss. Akad. Wiss. Berlin (Math. Phys.)*, vol. 1916, pp. 189–196, 1916.

[17] G. Nordström, "On the Energy of the Gravitation field in Einstein's Theory," *Koninklijke Nederlandse Akademie van Wetenschappen Proceedings Series B Physical Sciences*, vol. 20, pp. 1238–1245, Jan. 1918.

[18] B. P. Abbott *et al.*, "GWTC-1: A Gravitational-Wave Transient Catalog of Compact Binary Mergers Observed by LIGO and Virgo during the First and Second Observing Runs," *Phys. Rev. X*, vol. 9, no. 3, p. 031040, 2019.

[19] K. Akiyama and et al. [Event Horizon Telescope Collaboration], "The astrophysical journal," *Astrophys. J.*, vol. 875, no. 1, p. L1, 2019.

[20] K. Akiyama and others (Event Horizon Telescope), "First m87 event horizon telescope results. i. the shadow of the supermassive black hole," *Astrophys. J. Lett.*, vol. 875, p. L1, 2019.

[21] D. Psaltis *et al.*, "Gravitational Test Beyond the First Post-Newtonian Order with the Shadow of the M87 Black Hole," *Phys. Rev. Lett.*, vol. 125, no. 14, p. 141104, 2020.

[22] F. Atamurotov, A. Abdujabbarov, and B. Ahmedov, "Physical review d," *Phys. Rev. D*, vol. 88, no. 6, p. 064004, 2013.

[23] R. Shaikh, "Physical review d," *Phys. Rev. D*, vol. 100, no. 2, p. 024028, 2019.

[24] K. S. Virbhadra, "Distortions of images of Schwarzschild lensing," arXiv:2204.01879 2022.

[25] E. Copeland, M. Sami, and S. Tsujikawa, "International journal of modern physics d," *Int. J. Mod. Phys. D*, vol. 15, p. 1753, 2006.

[26] J. P. Luminet, "Image of a spherical black hole with thin accretion disk," *Astron. Astrophys.*, vol. 75, pp. 228–235, 1979.

[27] H. Falcke, F. Melia, and E. Agol, "Viewing the shadow of the black hole at the galactic center," *Astrophys. J. Lett.*, vol. 528, p. L13, 2000.

[28] T. Bronzwaer and H. Falcke, "The Nature of Black Hole Shadows," *Astrophys. J.*, vol. 920, no. 2, p. 155, 2021.

[29] R. Narayan, M. D. Johnson, and C. F. Gammie, "The Shadow of a Spherically Accreting Black Hole," *Astrophys. J. Lett.*, vol. 885, no. 2, p. L33, 2019.

[30] X.-M. Kuang and A. Övgün, "Strong gravitational lensing and shadow constraint from M87* of slowly rotating Kerr-like black hole," *Annals Phys.*, vol. 447, p. 169147, 2022.

[31] M. Okyay and A. Övgün, "Nonlinear electrodynamics effects on the black hole shadow, deflection angle, quasinormal modes and greybody factors," *JCAP*, vol. 01, no. 01, p. 009, 2022.

[32] L. Chakhchi, H. El Moumni, and K. Masmar, "Shadows and optical appearance of a power-Yang-Mills black hole surrounded by different accretion disk profiles," *Phys. Rev. D*, vol. 105, no. 6, p. 064031, 2022.

[33] P. Kocherlakota *et al.*, "Constraints on black-hole charges with the 2017 EHT observations of M87*," *Phys. Rev. D*, vol. 103, no. 10, p. 104047, May 2021.

[34] A. Uniyal, R. C. Pantig, and A. Övgün, "Probing a nonlinear electrodynamics black hole with thin accretion disk, shadow and deflection angle with M87* and Sgr A* from EHT," *Phys. Dark Univ.*, vol. 40, p. 101178, 5 2022.

[35] A. Övgün, I. Sakalli, and J. Saavedra, "Shadow cast and deflection angle of kerr-newman-kasuya spacetime," *JCAP*, vol. 1810, no. 10, p. 041, 2018.

[36] K. Jusufi, A. Övgün, A. Banerjee, and I. Sakalli, "Gravitational lensing by wormholes supported by electromagnetic, scalar, and quantum effects," *Eur. Phys. J. Plus*, vol. 134, no. 9, p. 428, 2019.

[37] R. C. Pantig, L. Mastrototaro, G. Lambiase, and A. Övgün, "Shadow, lensing, quasinormal modes, greybody bounds and neutrino propagation by dyonic ModMax black holes," *Eur. Phys. J. C*, vol. 82, no. 12, p. 1155, 2022.

[38] R. C. Pantig and A. Övgün, "Testing dynamical torsion effects on the charged black hole's shadow, deflection angle and greybody with M87* and Sgr. A* from EHT," *Annals Phys.*, vol. 448, p. 169197, 2023.

[39] R. C. Pantig, A. Övgün, and D. Demir, "Testing symmergent gravity through the shadow image and weak field photon deflection by a rotating black hole using the M87* and Sgr. A* results," *Eur. Phys. J. C*, vol. 83, no. 3, p. 250, 2023.

[40] I. Çimdiker, D. Demir, and A. Övgün, "Black hole shadow in symmergent gravity," *Phys. Dark Univ.*, vol. 34, p. 100900, 2021.

[41] J. Rayimbaev, R. C. Pantig, A. Övgün, A. Abdujabbarov, and D. Demir, "Quasiperiodic oscillations, weak field lensing and shadow cast around black holes in Symmergent gravity," *Annals of Physics*, no. 169335, 2023.

[42] NASA_ESA_CSA and STScI, "First Images from the James Webb Space Telescope," 2022.

[43] Z. Li and J. Jia, "Kerr-newman-jacobi geometry and the deflection of charged massive particles," *Phys. Rev. D*, vol. 104, no. 4, p. 044061, 2021.

[44] H. Gluck, "Differential geometry - herman gluck," https://www2.math.upenn.edu/~shiydong/Math501X-7-GaussBonnet.pdf.

[45] C. K. Qiao and M. Zhou, "The gravitational bending of acoustic schwarzschild black hole," arXiv:2109.05828 2021.

[46] A. Övgün, "Weak field deflection angle by regular black holes with cosmic strings using the gauss-bonnet theorem," *Phys. Rev. D*, vol. 99, no. 10, p. 104075, 2019.

[47] X. Er and S. Mao, "Monthly notices of the royal astronomical society," *Mon. Not. Roy. Astron. Soc.*, vol. 437, no. 3, p. 2180, 2014.

[48] G. Bisnovatyi-Kogan and O. Tsupko, "Universe," *Universe*, vol. 3, no. 3, p. 57, 2017.

[49] I. Rodríguez-Montoya, V. Ávila-Reese, A. Pérez-Lorenzana, and J. Venzor, "Constraints on the velocity dispersion of Dark Matter from Cosmology and new bounds on scattering from the Cosmic Dawn," *Astrophys. J.*, vol. 894, no. 1, p. 40, 2020.

[50] G. Crisnejo and E. Gallo, "Weak lensing in a plasma medium and gravitational deflection of massive particles using the gauss-bonnet theorem. a unified treatment," *Phys. Rev. D*, vol. 97, no. 12, p. 124016, 2018.

[51] C. R. Keeton and A. O. Petters, "Formalism for testing theories of gravity using lensing by compact objects. iii. braneworld gravity," *Phys. Rev. D*, vol. 73, p. 104032, 2006.

[52] K. S. Virbhadra, "Relativistic images of Schwarzschild black hole lensing," *Phys. Rev. D*, vol. 79, p. 083004, 2009.

[53] M. S. Ali and S. Kaushal, "Gravitational lensing for stationary axisymmetric black holes in eibi gravity," arXiv:2106.08464 2021.

[54] Z. Li, H. Liu, and J. Jia, "Deflection and gravitational lensing of null and timelike signals in general asymptotically (anti-)de sitter spacetimes," *Phys. Rev. D*, vol. 104, no. 8, p. 084027, 2021.

[55] R. E. T. Pantig Reggie C., Yu Paul K. and O. Ali, "Shadow and weak deflection angle of extended uncertainty principle black hole surrounded with dark matter," *Annals of Physics*, vol. 436, p. 168722, 2022.

[56] Q. M. Fu, L. Zhao, and Y. X. Liu, "Weak deflection angle by electrically and magnetically charged black holes from nonlinear electrodynamics," *Phys. Rev. D*, vol. 104, no. 2, p. 024033, 2021.

[57] W. Javed, J. Abbas, and A. Övgün, "Effect of the hair on deflection angle by asymptotically flat black holes in einstein-maxwell-dilaton theory," *Phys. Rev. D*, vol. 100, no. 4, p. 044052, 2019.

[58] R. C. Pantig and E. T. Rodulfo, "Weak deflection angle of a dirty black hole," *Chin. J. Phys.*, vol. 66, pp. 691–702, 2020.

[59] Z. Li and A. Övgün, "Finite-distance gravitational deflection of massive particles by a kerr-like black hole in the bumblebee gravity model," *Phys. Rev. D*, vol. 101, no. 2, p. 024040, 2020.

[60] Z.-Y. Li and T. Zhou, "Equivalence of gibbons-werner method to geodesics method in the study of gravitational lensing," *Phys. Rev. D*, vol. 101, no. 4, p. 044043, 2020.

[61] W. Javed, J. Abbas, and A. Övgün, "Deflection angle of photon from magnetized black hole and effect of nonlinear electrodynamics," *Eur. Phys. J. C*, vol. 79, no. 8, p. 694, 2019.

[62] A. Övgün, K. Jusufi, and I. Sakalli, "Gravitational lensing under the effect of weyl and bumblebee gravities: Applications of gauss-bonnet theorem," *Annals Phys.*, vol. 399, p. 193, 2018.

[63] I. Sakalli and A. Övgün, "Hawking radiation and deflection of light from rindler modified schwarzschild black hole," *EPL*, vol. 118, no. 6, p. 60006, 2017.

[64] K. Jusufi, "Gravitational lensing by reissner-nordström black holes with topological defects," *Astrophys. Space Sci.*, vol. 361, no. 1, p. 24, 2016.

[65] W. Javed, R. Babar, and A. Övgün, "Effect of the dilaton field and plasma medium on deflection angle by black holes in einstein-maxwell-dilaton-axion theory," *Phys. Rev. D*, vol. 100, no. 10, p. 104032, 2019.

[66] W. Javed, A. Hamza, and A. Övgün, "Effect of nonlinear electrodynamics on the weak field deflection angle by a black hole," *Phys. Rev. D*, vol. 101, no. 10, p. 103521, 2020.

[67] S. Hawking, "Nature," *Nature*, vol. 248, p. 30, 1974.

[68] R. Adler, P. Chen, and D. Santiago, "General relativity and gravitation," *Gen. Rel. Grav.*, vol. 33, p. 2101, 2001.

[69] J. Mureika, "Physics letters b," *Phys. Lett. B*, vol. 789, p. 88, 2019.

[70] B. Bolen and M. Cavaglia, "General relativity and gravitation," *Gen. Rel. Grav.*, vol. 37, p. 1255, 2005.

[71] X. Lu and Y. Xie, "Modern physics letters a," *Mod. Phys. Lett. A*, vol. 34, no. 20, p. 1950152, 2019.

[72] C. R. Keeton, "Computational methods for gravitational lensing," arXiv:astro-ph/0102340 2001.

[73] B. Turimov, B. Ahmedov, A. Abdujabbarov, and C. Bambi, "arxiv:1802.03293 [gr-qc]," 2018.

[74] X. Liu, J. Jia, and N. Yang, "Classical and quantum gravity," *Class. Quantum Grav.*, vol. 33, no. 17, p. 175014, 2016.

[75] T. Clifton, P. G. Ferreira, A. Padilla, and C. Skordis, "Modified gravity and cosmology," *Phys. Rept.*, vol. 513, p. 1, 2012.

[76] S. Capozziello and M. De Laurentis, "Extended theories of gravity," *Phys. Rept.*, vol. 509, p. 167, 2011.

[77] D. Blas, O. Pujolas, and S. Sibiryakov, "Consistent extension of horava gravity," *Phys. Rev. Lett.*, vol. 104, p. 181302, 2010.

[78] G. W. Horndeski, "Second-order scalar-tensor field equations in a four-dimensional space," *Int. J. Theor. Phys.*, vol. 10, p. 363, 1974.

[79] A. Anabalon, A. Cisterna, and J. Oliva, "Exact Hairy Black Holes and their Modification to the Universal Law of Gravitation," *Phys. Rev. D*, vol. 89, p. 084050, 2014.

[80] E. Babichev, C. Charmousis, and A. Lehébel, "Gravitational Bremsstrahlung in Black Hole-Scalar Field Scattering," *JCAP*, vol. 1704, no. 04, p. 027, 2017.

[81] J. Ezquiaga and M. Zumalacárregui, "Physical review letters," *Phys. Rev. Lett.*, vol. 119, no. 25, p. 251304, 2017.

[82] V. K. Oikonomou and F. P. Fronimos, "Reviving non-minimal horndeski-like theories after gw170817: kinetic coupling corrected einstein–gauss–bonnet inflation," *Class. Quant. Grav.*, vol. 38, no. 3, p. 035013, 2021.

[83] V. K. Oikonomou and F. Fronimos, "A nearly massless graviton in einstein-gauss-bonnet inflation with linear coupling implies constant-roll for the scalar field," *EPL*, vol. 131, no. 3, p. 30001, 2020.

[84] J. Badia and E. F. Eiroa, "Thick accretion disk in braneworld black holes," *Eur. Phys. J. C*, vol. 77, no. 11, p. 779, 2017.

[85] T. Kobayashi, "Horndeski theory and beyond: a review," *Rept. Prog. Phys.*, vol. 82, no. 8, p. 086901, 2019.

[86] R. Whisker, "Strong gravitational lensing by braneworld black holes," *Phys. Rev. D*, vol. 71, p. 064004, 2005.

[87] J. Maldacena, "Comments on magnetic black holes," *JHEP*, vol. 04, p. 079, 2021.

[88] S. Guo, G.-R. Li, and E.-W. Liang, "Influence of accretion flow and magnetic charge on the observed shadows and rings of the Hayward black hole," *Phys. Rev. D*, vol. 105, no. 2, p. 023024, 2022.

[89] C. Sun, Y. Liu, W.-L. Qian, and R. Yue, "Shadows of magnetically charged rotating black holes surrounded by quintessence *," *Chin. Phys. C*, vol. 46, no. 6, p. 065103, 2022.

[90] C. R. Keeton and A. O. Petters, "Formalism for testing theories of gravity using lensing by compact objects. i. static, spherically symmetric case," *Phys. Rev. D*, vol. 72, p. 104006, 2005.

[91] J. Bardeen, "Non-singular general-relativistic gravitational collapse," *in Proceedings of of International Conference GR5, Tbilisi, USSR*, p. 174, 1968.

[92] S. H. Mazharimousavi and M. Halilsoy, "Electric and magnetic black holes in a new nonlinear electrodynamics model," *Annals Phys.*, vol. 433, p. 168579, 2021.

[93] F. T. Falciano, M. L. Peñafiel, and S. E. Perez Bergliaffa, "Entropy bounds and nonlinear electrodynamics," *Phys. Rev. D*, vol. 100, no. 12, p. 125008, 2019.

[94] V. Perlick and O. Y. Tsupko, "Calculating black hole shadows: Review of analytical studies," *Phys. Rept.*, vol. 947, pp. 1–39, 2022.

[95] K. Akiyama *et al.*, "First Sagittarius A* Event Horizon Telescope Results. I. The Shadow of the Supermassive Black Hole in the Center of the Milky Way," *Astrophys. J. Lett.*, vol. 930, no. 2, p. L12, 2022.

[96] C. Bambi, "Can the supermassive objects at the centers of galaxies be traversable wormholes? The first test of strong gravity for mm/sub-mm very long baseline interferometry facilities," *Phys. Rev. D*, vol. 87, p. 107501, 2013.

[97] S. E. Gralla, D. E. Holz, and R. M. Wald, "Black Hole Shadows, Photon Rings, and Lensing Rings," *Phys. Rev. D*, vol. 100, no. 2, p. 024018, 2019.

[98] S. Bapat *et al.*, "EinsteinPy: A Community Python Package for General Relativity," arXiv:2005.11288 2020.

[99] S. A. Hayward, "Formation and evaporation of regular black holes," *Phys. Rev. Lett.*, vol. 96, p. 031103, 2006.

[100] S. I. Kruglov, "Black hole as a magnetic monopole within exponential nonlinear electrodynamics," *Annals Phys.*, vol. 378, pp. 59–70, 2017.

[101] A. Ali and K. Saifullah, "Asymptotic magnetically charged non-singular black hole and its thermodynamics," *Phys. Lett. B*, vol. 792, pp. 276–283, 2019.

[102] M. Jaroszynski and A. Kurpiewski, "Optics near kerr black holes: spectra of advection dominated accretion flows," *Astron. Astrophys.*, vol. 326, p. 419, 1997.

[103] M. Sereno, "Gravitational lensing in metric theories of gravity," *Phys. Rev. D*, vol. 67, no. 6, p. 064007, 2003.

[104] R. Izmailov, R. Karimov, E. Zhdanov, and K. Nandi, "Monthly notices of the royal astronomical society," *Mon. Not. Roy. Astron. Soc.*, vol. 483, no. 3, p. 3754, 2019.

[105] C.-Y. Wang, Y.-G. Shen, and Y. Xie, "Weak and strong deflection gravitational lensings by a charged horndeski black hole," *JCAP*, vol. 04, p. 022, 2019.

[106] F. Liu, Y. Mai, W. Wu, and Y. Xie, "Physics letters b," *Phys. Lett. B*, vol. 795, p. 475, 2019.

[107] S. Mendoza and Y. M. Rosas-Guevara, "Gravitational waves and lensing of the metric theory proposed by Sobouti," *Astron. Astrophys.*, vol. 472, pp. 367–371, 2007.